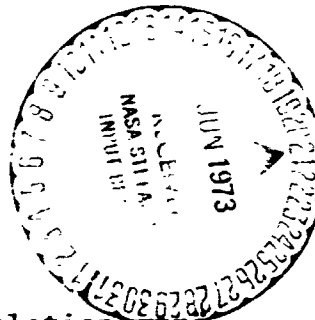


THE RECIRCULATION FLOW FIELD OF A VTOL LIFTING ENGINE

E. Schwantes



Translation of: "Das Rezirkulationsstromungsfeld eines VTOL-Hubtriebwerks", Deutsche Forschungs- und Versuchsanstalt für Luft- und Raumfahrt, (W. Germany). DLR-FB-72-50, 179 pages.

(NASA-TT-F-14912) THE RECIRCULATION FLOW
PATTERN OF A VTOL LIFTING ENGINE
(Scientific Translation Service) 201 p
HC \$12.25 CSCL 20D

N73-2-323

Unclas

63/12 05414

NATIONAL AERONAUTICS AND SPACE ADMINISTRATION
WASHINGTON, D. C. 20546
JUNE 1973

German Research and Test Institute for Aeronautics and Astronautics
Institute for Air-Breathing Engines
Division: Jet Deflection

Braunschweig, July 1972

Institute Director: Dr.-Ing. W. Alvermann
Author: Dipl.-Eng. E. Schwantes

This work appears simultaneously as a dissertation accepted by the Faculty for Machine Design and Electrotechnology of the Technical University of Braunschweig toward fulfillment of the academic degree of Doctor-Engineer.

SUMMARY:

A method is developed to predict theoretically the increase of temperature due to wind recirculation in the inlet of a VTOL lift engine exhausting normally to the ground. It is shown how to calculate with the potential theory the velocities in the recirculation flow and how to determine the temperatures with the laws of spread of buoyant plumes. Many model investigations were done to check these results. The three regions of a VTOL propulsion jet, the free jet, the wall jet, and the zone of separation of the wall jet from the ground due to wind effects and buoyancy forces are investigated in model jets with critical nozzle pressure ratios and temperatures up to 1000 °C.

This work was done at the Institute for Air-breathing Engines of the German Research and Test Institute for Aeronautics and Astronautics (DFVLR) at the Braunschweig Research Center.

I thank Prof. Dr.-Ing. O. Lutz for recommending and supporting this work. I Thank Prof. Dr.-Ing. F. Thomas for his interest in this work and his valuable counsel.

Dipl.-Ing. H. Dissen suggested this work to me in my diploma work in 1966 and has provided strong support. My co-workers deserve very special thanks. Without their many ideas which aided the design of the test system and the performance of the measuring program, it would not have possible to do such extensive tests in such a short time. H. Goldmann designed the test system. K. D. Karsten was responsible for the measuring technology and the electronic data collection, and also helped me set up the evaluation program. W. Wolters produced the measuring probes and supported me in performing the tests.

I thank Miss C. Böhm and Mr. K. Brewka for preparing the many diagrams and drawings. Finally, I thank Mrs. B. Matthiess for her careful production of the final draft of this work.

Eckart Schwantes

OUTLINE

	Page
1. Introduction - recirculation in jet-supported VTOL aircraft	1
2. Previous results and knowledge. Statement of the problem	5
3. Theory	10
3.1 Recirculation velocities	10
3.1.1 Application of the potential theory	10
3.1.2 Description of the potential theory model	12
3.1.3 Calculation of the recirculation velocities	17
3.2 Recirculation temperatures	21
3.2.1 Description of the model for temperature calculation	21
3.2.2 Plane ascending flow	22
3.2.3 Ascending flow in the recirculation flow field	30
3.2.4 Calculation of the recirculation temperatures	34
4. Experiments	39
4.1 Experimental design and measuring technique	39
4.2 Measurement of the recirculation velocities	43
4.3 Measurement of the recirculation temperatures	46
5. Comparison of the theoretical and experimental results	49
6. Summary	52
7. Bibliography	55
8. Figures	61

	Page
9. Appendix	82
9.1 Engine process	82
9.2 Potential theory	90
9.3 Ascending flow	103
9.4 Rotationally symmetric free jet	117
9.4.1 Turbulence of the free jet	118
9.4.2 Experimental design and measuring technique	121
9.4.3 Calculation of the velocity and temperature from the measurements	122
9.4.4 Pitot probe measurement errors due to turbulence	125
9.4.5 Systematic error in temperature measurement with thermocouples	128
9.4.6 Static pressure	137
9.4.7 Axial value	140
9.4.8 Jet width	141
9.4.9 Similarity of the free jet profile	142
9.4.10 Jet edge	143
9.4.11 Volume, mass and momentum flow	145
9.4.12 Inflow velocity	147
9.4.13 Effect of the nozzle shape	150
9.5 Rotationally symmetric wall jet	150
9.5.1 Experimental design and measuring technique	160
9.5.2 Ground pressure	162
9.5.3 Turbulence	163
9.5.4 Similarity of the profiles and wall jet breakup	164
9.5.5 Half-value heights	166
9.5.6 Volume, mass and momentum flow	167
9.5.7 Inflow velocity	170

9.5.8 Separation of the wall jet from the ground by the wind effect	172
9.6 Measuring accuracy and error estimation	190

ABBREVIATIONS

b	Width
c_p	Specific heat capacity
D	Nozzle diameter
e	Base of natural logarithms
F	Area, thrust
g	Acceleration of gravity
Gr	Grashof's number
H	Height of the jet orifice above the ground
h'	Wall jet thickness at the point of separation
l	length
M	Mach number
\dot{m}	Mass flow
N	Natural number
P	Pressure force
q	Dynamic pressure, heat flux density, depression distribution
R	Radius outward from the jet impact point; separation radius
r	Radius, distance
Re	Reynold's number
s	Path distance, standard deviation
T	Temperature
t	Time
u	Velocity component
V	Volume, substitution quantity
\dot{V}	Volume flow
v	Velocity component
W	Substitution quantity

w	Wind velocity
X	Force per unit volume
x	Coordinate
x'	Distance in the x direction
y	Coordinate
y'	Distance in the y direction
Z	Substitution quantity
z	Coordinate
α	Velocity ratio
Γ	Adiabatic temperature gradient of the atmosphere
γ	Dimensionless parameter for the temperature gradient
δ_1	Displacement thickness of the wind boundary layer
ζ	Dimensionless parameter for the ascending flow velocity
η	Dimensionless parameter for the ascending flow width
θ	Temperature above ambient: $T - T_\infty$, potential temperature
θ'	Excess temperature of the ascending flow
λ	Dimensionless parameter for the ascending flow temperature, coefficient of thermal conductivity
μ	Dynamic viscosity
ξ	Dimensionless parameter for the path of the ascending flow
π	Circle number
ρ	Density
τ	Thrust force
Φ	Potential function
φ	Angle of rotation

INDICES

o State at the nozzle orifice
a, ∞ Ambient state
b Width
E Compressor intake
ges Total
i Serial number
m Mean
max Maximum or axial value
W Wind effect

OVERSTROKES

- Time average

Dimensions are stated in millimeters.

1. Introduction - Recirculation in jet-supported VTOL aircraft / 9*

The ground effects induced by the free jet of the lifting engine have a considerable effect on the design and shape of V/STOL ⁽¹⁾ aircraft. This effect causes both increases in the lift as well as forces on the airframe which reduce lift, runway damage, and even damage to the airframe, through ground erosion, and considerable added noise stresses. In detail, we distinguish between the following jet-induced ground effects:

Aerodynamic ground effect

Thermal ground effect (recirculation)

Fountain recirculation

Wind recirculation

Ground erosion

Noise

The engine jets, directed toward the ground to produce lift during the takeoff and landing phases of a V/STOL aircraft, produce secondary forces and moments on the aircraft which increase or reduce the lift. This is the aerodynamic ground effect. Engine jets redirected at the ground meet each other in the so-called fountain effect, are redirected upward by it, strike the wings or the fuselage, and produce a local overpressure region there, increasing the lift. In contrast, the intake flow drawn into the thrust jet decreases the lift. Depending on the engine arrangement, the portions which increase or reduce the lift may predominate. Also, this secondary flow induced by the supporting jet can cause turbulent flow in flowing around the wing edges across the whole wing contour, and can lead to dynamic loads on the airframe due to vortex formation.

(1) Vertical/Short TakeOff and Landing

*Numbers in the margin indicate pagination in original foreign text.

In recirculation, the thermal ground effect, part of the hot / 10 engine jet is returned to the intake through redirection at the ground, the thermal lift forces, and the depression effect of the engine intake. The temperature increase at the intake can take on quite considerable values with mutual engine jet effects and the wind effect. This can cause a significant drop in engine power during hovering flight over the ground, the time of maximum requirement for thrust, and can cause the aircraft to crash.

The sensitivity of jet engines to an increase in the intake air temperature is shown in Appendix 9.1 with the Rolls-Royce RB 162-31 lift engine as an example (Figure 1), and is shown graphically in Figure 2. Even two degrees of temperature rise

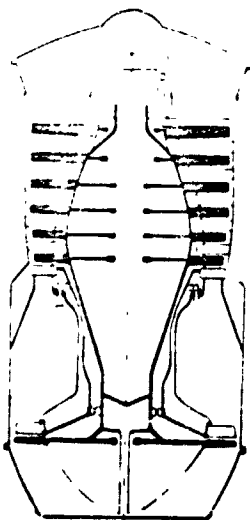


Figure 1. Rolls-Royce single-shaft lift engine RB 162.

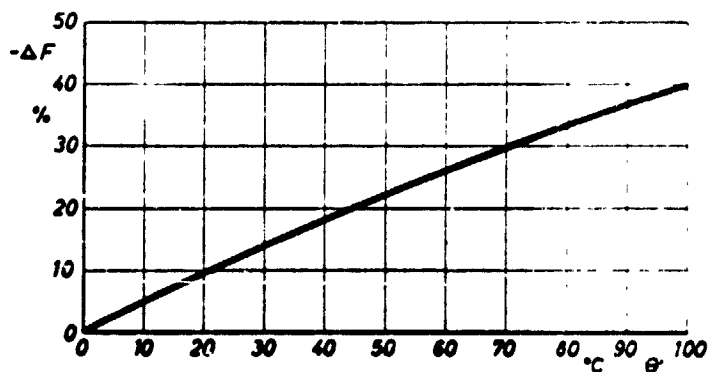


Figure 2. Thrust loss of the RB 162-31 as a function of the temperature rise at the compressor intake.

cause one percent loss of thrust. This justifies the great attempts of designers to protect engine intakes on VTOL aircraft from recirculation flow.

If several free jets strike the ground vertically, their wall jets which move toward each other are redirected upward as ascending flow fountains. Hot engine exhaust gases can get directly into the compressor intake this way, reducing the thrust production, cutting off the engine, or damaging the airframe due to high temperatures. Here, we speak of fountain recirculation or recirculation of the near zone. Local temperature peaks up to 70% of the nozzle have been measured at the level of the engine intake in such hot gas streams shooting upward. Along with the loss of thrust which occurs, the operating behavior of the engine is severely disturbed by such uneven temperature profiles at the intake cross section (inlet distortion). On the basis of extensive series of tests in the past years, we are now able, for new aircraft designs, to avoid from the beginning those engine arrangements in which hot gas fountains could occur. For instance, fountains can be avoided by slightly pivoting the engine jet away from the vertical or through injecting an auxiliary jet to destroy the fountain. /11

The wind recirculation (Figure 3) is considered far more problematical today. This process is also called "recirculation of the far zone". It occurs when a supporting jet redirected at the ground flows into a wind flow which separates the hot wall jet from the ground and carries it back to the engine intake. In bad cases, this hot air cloud washes over the entire aircraft. /12

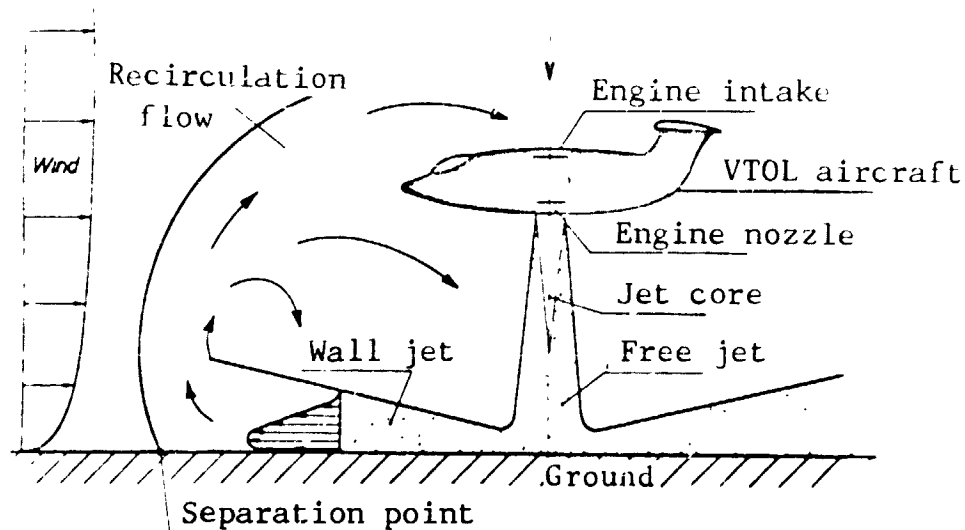


Figure 3. Wind recirculation in a VTOL aircraft.

In contrast to the hot gas fountains, the wind recirculation causes only relatively small temperature rises at the intake, rarely exceeding 30°C , but this recirculation is much more difficult to combat or eliminate. The trend in lifting engine technology toward larger-volume jets with low specific impulse is moving the problem of wind recirculation more and more to the front. This work is concerned exclusively with the wind recirculation.

The ground erosion leads to destruction of the ground by the hot high-velocity jet. Depending on the nature of the ground, it tears out pieces and may even damage the airframe or the engine, or hinder the pilot's vision.

The noise of VTOL aircraft with single-shaft lifting engines which occurs in hovering flight comes almost solely from the supporting jet. In addition to the jet noise of the conventional aircraft, with a VTOL engine jet there is also the acoustically stressing back-coupling effect described by Wagner [75].

2. Previous results and knowledge - statement of the problem. / 13

Today, we find a whole series of works in the literature, concerned with recirculation flows in VTOL aircraft. Most of the investigations on the thermal ground effect up to 1968 have been collected and briefly described in the literature survey [61]. It appears from this that so far only a few authors have made the attempt to describe the ground effect theoretically. So far, only one semiempirical theory on the hot gas wall jet has been published by the Englishman Cox-Abbott [11]. He attempts to determine the separation point of the hot wall jet caused by thermal buoyancy forces. In comparison, most of the reports are limited to the reporting of experimental results. In recent years in the USA, NASA has performed a series of extensive intake temperature measurements, by Speth-Ryan [69], Lavi-Hall-Stark [36] and McLemore-Smith [37], on VTOL aircraft models with the original engines. Almost without exception, these experiments were concerned with complicated aircraft configurations, and make statements on the intake state of the engine. But basic research on the parameters of the supporting jet and the flow drawn into it, which are important for the ground effect, remain unconsidered in these works.

Now, if one wishes to take the missing data on the VTOL supporting jet from the literature on free jet and wall jet flows, one must establish that nearly all basic studies have been done with jets having low nozzle pressure ratios, with or without low excess temperature. But with single-shaft lifting engines,

we have sonic velocity and exhaust gas temperatures between 600 and 1000 °C at the nozzle orifice. But, because of the different degree of turbulence, these engine jets are subject to different expansion laws than are incompressible cold gas jets. The classical free jet works of Tollmien [74], Reichardt [51], Förthmann [18], Corrsin-Uberoi [10], Laurence [35] and Wille [76] which are still used for most ground effect studies, however, are concerned with cold or only slightly heated jets in the fully expanded region far behind the nozzle. They do not go into the problematical definition of the jet boundary in hot gas jets (Section 9.4.10). But exact data on the jet boundaries are of decisive importance for determination of the mass drawn in. The basic wall jet studies of Glauert [21], Rakke [3], Bradshaw-Love [8], Hertel [25], Schrader [58] and Tani-Komatsu [72] also, without exception, treat incompressible jets without excess temperature. The "reversal effect" of the wall jet established here, which is the explanation for many phenomena which have not been understood in ground effect studies, has previously been measured by Schrader [58], and he has not considered it further. In the literature, statements on the separation behavior of wall jets under the effect of wind can only be found in Cox-Abbott [1']. The reversal effect is discussed in Section 9.5.4.

Seibold [65] in 1962 and Schulz [59] in 1970 performed the potential-theory calculation of the velocities in the secondary flow field from a single free jet in order to obtain the pressure distribution induced on the airframe, and, from that, to determine the secondary forces acting on the aircraft. In 1966 [60] the entire two-dimensional recirculation flow field of a single lifting engine was determined according to potential theory. But these calculations stand or fall with the boundary conditions. These are statements on the depression distribution of the supporting jet and on the separation length of the wall jet. Previously, these values have either been estimated or taken

from older free jet measurements which have only little predictive power for the VTOL jet.

Determination of the exact boundary conditions was a major prerequisite for the successful treatment of the recirculation problem. In years past, therefore, intensive free jet and wall jet studies have been performed. These are partially reported in [62, 63, 64]. These studies are described in detail in Appendices 9.4 and 9.5. Their most important results will be related briefly here: / 15

Free jet

The behavior of the high velocity jet differs from that of the low velocity jet. If one wishes to produce a supporting jet near to reality for a single-shaft lifting engine, we may change only the geometric dimensions. The jet Mach number and temperature must be maintained.

With convergent nozzles and critical nozzle pressure ratio p_{ges}/p_{∞} the core flow of the free jet is supersonic.

With increasing Mach number, the jet turbulence decreases and the jet breakup becomes less.

With increasing nozzle Mach number, the jet expansion angles become smaller for velocity, dynamic pressure and temperature. In contrast to the free jet with low nozzle velocity, the jet expansion angle of the Mach 1 jet is nearly independent of the temperature of the jet. At a length of 5 jet diameters, the hot gas jet increases its dimension considerably faster than the cold gas jet.

Wall jet

As the nozzle approaches the ground, the maximum dynamic pressure and velocity in the wall jet decrease (reversal effect). The mass flow of the wall jet increases slightly with increasing distance of the nozzle from the ground. It increases considerably with increase of the nozzle temperature. If it is normalized with respect to the free jet mass flow at the stagnation point, the increase in mass of the wall jet can be described by a single straight line.

/16

Separation of the wall jet

The separation length of the wall jet increases linearly with decreasing wind velocity.

The wall jet separation because of blowing wind is independent of the nozzle temperature, but, in contrast, the nozzle Mach number has a strong effect on the site of separation.

The temperatures of the recirculation flow in the secondary field of the supporting jet can be calculated from the expansion laws of rising warm air clouds. Such studies of thermal flows are known from meteorology and have been applied, among other things, for dispersal of fog over airfields (e. g., by Rankine [48], Rouse-Baines-Humphreys [54], Morton [43], Morton-Taylor-Turner [44], Priestley-Ball [47], Murgai-Emmons [45] and Sutton [70, 71]). These authors did not consider the wind effect. We cannot, however, combine these publications on ascending flows with the works on cold gas free jets blowing against objects perpendicular to their axes, by Keffer-Baines [34], Bradbury-Wood [6], Grove-Riesebieter [12], Gelb-Martin [20], Jordinson [33] and the authors of [41] and the research results on the expansion of smoke clouds from hot chimney flows by

Bosanquet-Carey-Mech-Halton [4], Wippermann [77] and Rauch [49] because all these studies treat rotationally symmetrical jets and, therefore, do not adequately describe the largely two-dimensional recirculation flow. In this work, then, we must follow a new route in order to describe conditions in the warm air clouds which rise above the site of separation and then blow away.

Model laws for the recirculation flow are important for the interpretation of model measurements. In this respect, Cox-Abbott [11] in 1964 and Behnert [5] in 1970 have proposed model parameters with which the results from model investigations with jets of low nozzle Mach number and excess temperature could be recalculated to such higher Mach number and temperature. But such recalculations between the model and the original are reasonable only if the flow conditions for the two are similar. But this similarity becomes questionable because of the changed expansion laws for the high velocity jets in comparison to the free jet with lower nozzle outlet velocity demonstrated in this work. Hall [23], who made comparative measurements of engine intake temperatures on a large model with real engines and a small model of the same configuration in 1970, came to the conclusion that there is similarity in recirculation flows only if the initial conditions of the engine jet, such as temperature, Mach number and degree of turbulence are identical for the full scale design and the model. Seifferth [66] confirmed this model. He investigated the model similarity of hot gas wall jets, with the critical nozzle pressure ratio and the nozzle temperature identical, but with the nozzle diameter varied between 10 and 50 mm. He established similar temperature and dynamic pressure profiles. Also, Hueber [32] had shown as early as 1964 that complete similarity of the recirculation processes between model and full scale are attained only if the original jet temperature is maintained in the model experiment. To be sure, he writes nothing in his work of the important Mach

/ 17

similarity.

In summary, we can say that today, in spite of the many experiments which have been done with VTOL aircraft models, the flow mechanism of the supporting jet and its secondary flow is not yet completely explained. Thus, it is not yet possible to make a theoretical prediction of the engine intake temperature to be expected because of recirculation as a function of the exhaust gas parameters of the engine, the height of the nozzle above the ground and the wind velocity. In this work, the expansion laws of the VTOL supporting jet are investigated with realistic nozzle temperatures and Mach numbers.

To do this, we have performed systematic model experiments on free jets, and on wall jets and their separation behavior as influenced by the wind. Based on these results, we have developed a method by means of which the recirculation flow for a single lifting engine and its intake temperatures can for the first time be calculated. These theoretically determined values are tested by model experiments, and have been confirmed. The temperature increase to be expected at the compressor intake due to wind recirculation for a certain engine configuration has been presented so that the project engineer can read it off a diagram (Figure 47).

/18

3. Theory

3.1 Recirculation velocities

3.1.1 Application of the potential theory

Here we shall present a method with which the velocity vectors of the entire three-dimensional recirculation flow field can be calculated in the near and far vicinity of a lifting engine blowing vertically onto the ground, according to potential

theory. By definition, potential flows are frictionless flows of constant temperature. The absence of friction is fulfilled well in the recirculation flow field, but we cannot speak of an isothermal flow.

As the following estimate will show, however, the temperature differences in the secondary flow field are so slight that the thermal lift forces due to local excess temperatures are small in relation to the kinetic flow forces generated by the wind flow and the suction effect of the jet. This can be clarified by the ratio

$$\frac{\text{kinetic force}}{\text{buoyancy force}} = \frac{q \cdot l^2}{l^3 \cdot g \cdot 1/T_a \cdot \theta \cdot \rho} \sim \frac{Re^2}{Gr} \quad (3.1)$$

Choice of the reference length, l , determines the numerical value of the ratio. The displacement thickness δ_1 of the wind boundary layer is considered to be the most reasonable length for formulating the Reynolds and Grashof numbers for the recirculation flow. According to Schlichting [56] this makes up some 1/3 of the total boundary layer thickness for a plate with longitudinal incident flow. Corresponding to Figure 112, then, the wind boundary layer thickness is about 6 m, so that δ_1 is some 2 m.

/ 19

The velocities in the recirculation flow field studied vary between 5 and 20 m/s (Section 4.2). This corresponds to an dynamic pressure range of 1.5 mm water $< q <$ 25 mm water.

According to Section 4.3, the recirculation temperatures θ' vary between 0 and 25°C. If we select for this estimate the extreme value $\theta' = 25^\circ\text{C}$, and an ambient temperature T_a of 288°K, then the characteristic ratio shown above is between the limits:

$$8 < \frac{\text{kinetic force}}{\text{buoyancy force}} < 130$$

In the recirculation flow field, the kinetic force exceeds the thermal force by one to two orders of magnitude, so that is the dominant quantity for the course of the flow, and allows the treatment of the recirculation process according to potential theory.

3.1.2 Description of the potential theory model

If one superimposes a series of sources and sinks in the proper way, it is possible to induce in the vicinity of the singularity a velocity field similar to that caused by a lifting engine blowing on the ground. The secondary flow field induced by the lift engine and the supporting jet are described with the potential theory mode. The flow conditions in the primary jet itself and in its adjacent turbulent mixing zone cannot be reproduced with this method.

The depression effect of the engine intake is produced by two adjacent point sources and point sinks with different strengths. The suction effect of the free jet and the wall jet can be simulated by line or area sinks. Light section photos of the free and wall jet intake flow show that the inflow direction of the secondary air at the jet boundary is not perpendicular to the jet surface. The inflow direction departs from the normal at the jet margin. Thus it is reasonable to place the line sink causing the suction effect of the free jet at the jet axis and not at the outer jet surface. A similar situation applies for the area sink of the wall jet. The separation of the wall jet from the ground, caused by wind and thermal buoyancy forces, can be reproduced well by the flow

/20

induced by a source on a cylindrical shell along with an adjacent annular sink. Because area singularities always flow to both sides, the in-flow from the cylindrical source which would disturb the recirculation flow field must be absorbed by the ring sink. It is shown in Appendix 9.5.8 that the separation line directed against the wind is deformed from a circular ring to an ellipse. Therefore, in the potential theory model also, the area sink simulating the wall jet and the source-sink pair representing the separation, the cylindrical source and the ring sink, must take on an elliptical form when the wind blows. The wind flow itself corresponds to a translational flow with a velocity gradient. The effect of the ground is generated by reflection of the potential flow.

The complete potential theory model with the various singularities for computation of the recirculation flow velocities is shown in Figure 4 and in the following table.

/ 21

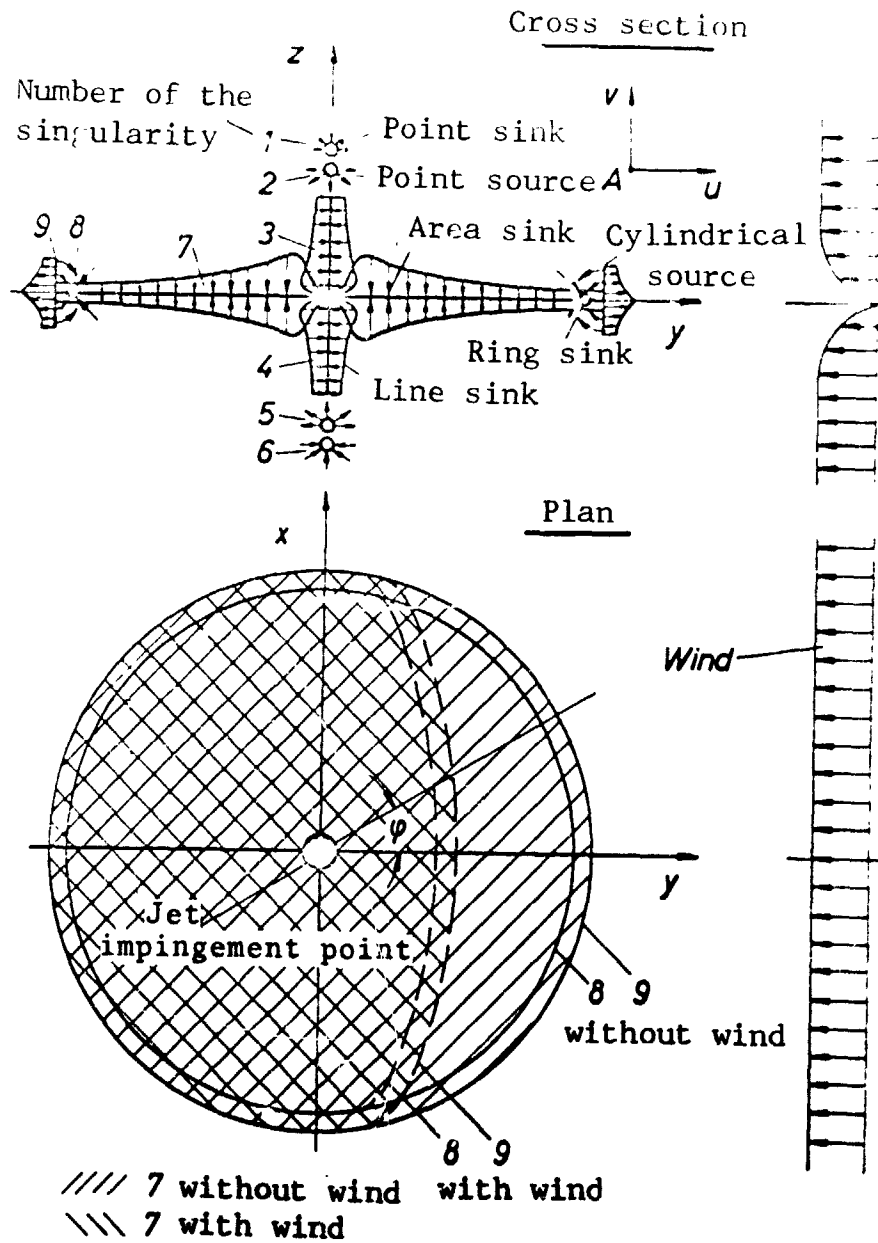


Figure 4. Potential theory model.

No. of the singularity in the potential model	Type of the Singularity	Physical Significance		/ 22
1,6 2,5 3,4	Point sink Point source Line sink	Engine intake Free jet		
7 8 9	Area sink Ring sink Cylindrical source	Wall jet Separation location	Without wind	
7 8 9	Elliptical area sink Elliptical ring sink Elliptical cylindrical source	Wall jet Separation location	With wind blowing	

The velocity and its direction at an arbitrary point in the y-z plane appears from the vectorial sum of the components U_{ges} and V_{ges} , which are made up of the induced velocity components of all the singularities of the potential theory model:

$$U_{ges} = U_1 + U_2 + U_3 + \dots + U_{10} + U_w$$

$$V_{ges} = V_1 + V_2 + V_3 + \dots + V_{10} .$$

The velocity components induced by the individual singularities of the potential theory model in the y-z plane of the spatial coordinate system are derived in Appendix 9.2. As they are calculated from potential equations, the potential functions for the various source types are presented here. For completeness, the potential functions for plane flows are also given:

	two-dimensional	three-dimensional
(3.2) point source	--	$\phi = -\frac{1}{4\pi} \cdot \dot{V} \cdot \frac{1}{r}$
(3.3) line source	$\phi = \frac{1}{2\pi} \cdot \frac{\dot{V}}{l} \cdot \ln r$	$\phi = -\frac{1}{4\pi} \cdot \frac{\dot{V}}{l} \int_S \frac{1}{r} ds$
(3.4) area source	$\phi = \frac{1}{2\pi} \cdot \frac{\dot{V}}{F} \int_S \ln r ds$	$\phi = -\frac{1}{4\pi} \cdot \frac{\dot{V}}{F} \iiint_F \frac{1}{r} dF$
(3.5) volume source	$\phi = \frac{1}{2\pi} \cdot \frac{\dot{V}}{V} \iiint_F \ln r dF$	$\phi = -\frac{1}{4\pi} \cdot \frac{\dot{V}}{V} \iiint_V \frac{1}{r} dV$

Here \dot{V} is the magnitude of the source. l , F and V are the length, area, and volume sizes of the source and r is the distance between the induced source point and the induced field point. The induced velocities at the field point are obtained by differentiation of the potential function

$$u = \frac{d\phi}{dy} , \quad v = \frac{d\phi}{dz} . \quad (3.6)$$

As long as we are dealing with simple integrals in the potential function of the potential theory model, this can be solved; but double integrals, because of their complex structure, can be integrated only once. The remaining residual integral must then be solved numerically. Superimposition, with the proper signs, of the induced velocity components of the individual singularities is done very carefully because of the complicated structure of the potential theory model and the difficulty in understanding the form of the integral equations.

The source strengths and the geometric dimensions of the model are necessary boundary conditions for the potential theory calculation.

Half the sink strength of a singularity is equal to the velocity component induced perpendicular to its surface. Thus, the sink strength of the jet is identical with twice the velocity at which air is drawn into it. The distributions of the free jet and wall jet inflow velocities are given in Figures 9 and 10. The extents of the singularities number 7, 8, and 9 are determined by the separation length of the wall jet, shown in Figure 11 as a function of the wind velocity and the nozzle Mach number. /24

3.1.3 Calculation of the recirculation velocities

The velocity vectors of the secondary flow field of a single lift engine blasting vertically onto the ground have been calculated according to the potential theory method with the boundary conditions measured in Appendix 9.4 and 9.5. For this, the integrals appearing in Equations 9.45, 9.47, 9.51, 9.52, 9.58 and 9.92 were solved numerically with an electronic computer using the Simpson method with a step width of 0.2. The velocity vectors thus calculated were plotted, with computer assistance, on a Graphomat. For reasons of computing technology, the variable source strength $q(y)$ of the free and wall jets were not inserted as polynomial functions into the potential equations, but were treated as constant values for each section.

The exhaust gas jet parameters in the computer model were selected on the basis of the nozzle values calculated in Appendix 9.1 for the RB 162-31 engine. The jet temperature must be changed, however, to the value obtained in the model experiment for which the sink distributions were determined.

The secondary flow field was also calculated for the modern two-shaft Rolls Royce RB 202 lift engine, although the boundary conditions for this two-shaft jet were estimated from the velocities averaged for the primary and secondary jet, (Figure 5). / 25

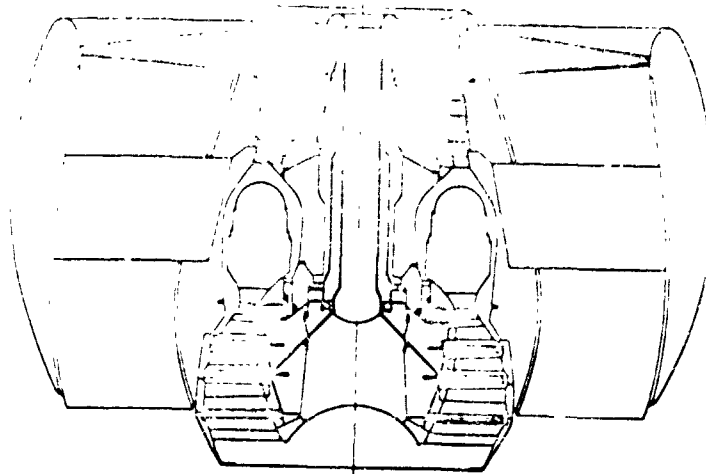


Figure 5. Rolls-Royce RB 202 two-shaft lift engine.

The following table shows the various configurations for which the velocity field was computed.

Figure 12 represents the basic case for the secondary flow of a single supporting jet. Here, in still air, surrounding air is sucked into the engine intake, the free jet, and the wall jet. In the RB 162 the engine intake is some four nozzle diameters above the nozzle plane. Flow into the inlet is attained by a point sink in the intake plane and a point source some two nozzle diameters below it. The source under the sink has the purpose of simulating the engine contour, with the resulting dipole flow. The volume flowing from the source to the sink does not participate in the volume balance of the model. It is only intended to produce a physically reasonable engine intake flow. The sink distribution of the line sink of the free jet and the area sink of the wall jet is taken from the measurements / 27 across the inflow velocities (Figure 9.10).

	Wind	Intake	Exhaust gas jet						Wall jet			Engine	
Figure w No.	H/D	\dot{V}_E	D_o	\dot{V}_o	\dot{m}_o	u_o	T_{ostat}	T_{oges}	M_o	$R_{w=0}$	$\dot{V}_{w=0}$	\dot{V}_w	
	$\frac{m}{s}$	$\frac{m^3}{s}$	m	$\frac{m^3}{s}$	$\frac{kg}{s}$	$\frac{m}{s}$	$^{\circ}C$	$^{\circ}C$	-	m	$\frac{m^3}{s}$	$\frac{m^3}{s}$	
12	0	37	0,475	92,5	46	522	409	500	1	41	-	3000	-
13	5	37	0,475	92,5	46	522	409	500	1	41	22	3000	1300
14	5	0	0,475	92,5	46	522	409	500	1	41	22	3000	1300
15	20	37	0,475	92,5	46	522	409	500	1	41	5,2	3000	316
16	5	25	0,475	65	33	368	409	500	0,7	29	10	1500	422
17	5	37	0,475	92,5	46	522	409	500	1	41	22	3600	1500
18	5	231	1,4	307	289	200	90	110	0,55	71	14	9100	1590

RB 162

RB 202

RB 162

$R_{w=0}$ is the thermal separation radius of the wall jet, calculated according to Cox and Abbott [11].

R_w is the distance between the jet impact point and the point of separation in the plane of symmetry, caused by the wind.

$\dot{V}_{w=0}$ is the total volume flow of the wall jet at $R_{w=0}$

\dot{V}_w is the volume flow of the wall jet at R_w

Numbers represent decimal points.

At a distance of 41 m from the jet impact point, the wall jet separated from the ground along a circular arc because of thermal buoyancy forces. At the site of separation, the wall jet has a thickness of about 4 m, so that the separation is represented by a cylindrical source 4 m high. Its source distribution corresponds to that of a wall jet velocity profile with the maximum value at the ground and the zero position at 4 m elevation. The volume flow moving from the cylindrical source to the outside must be equal to that injected by the intake, free jet and wall jet. As the cylindrical source sends a volume flow both inward and outward, but the inward flow is not physically reasonable in the existing model, and must not affect the secondary flow, it is completely absorbed by a ring sink which is 0.5 m inside the cylindrical source.

In Figures 13 - 18 the secondary flow field is shown superimposed on a wind flow with velocity profile having reference values of 5, 10 and 20 m/s at 3 m height, according to Equation 9.144. While the engine intake flow, the free jet, and the surface covered by the wall jet going downwind remain unchanged, the separation line running toward the wind is deformed by the premature wall jet separation into half an ellipse, with the major semiaxis across the wind direction. Now the two basic surfaces of the wall jet, the ring sink 8 and the cylindrical source 9 take on an elliptical shape in the two quadrants turned toward the wind. Thus the angular distribution of the singularities 8 and 9 becomes a function of the angle φ . At small angles the path of the wall jet is short and the volume flowing out at the site of separation is correspondingly smaller than at large angles φ . Furthermore, the height of the cylindrical source 9 also changes as φ varies. The cylinder height must always agree with the actual wall jet thickness for the different separation lengths.

It proved expedient to arrange the cylindrical source about 20% in front of the location of the separation line which was established in Appendix 9.5.8 through light section photographs of the maximum radial path of the wall jet, because the flow out of the cylindrical source still runs for a certain distance horizontally against the wind before it reaches the location defined as the separation radius. /-*

The minor influence of the sink strength of the engine intake on the recirculation flow field was demonstrated in Figure 14. Here, the entire engine and its intake sink is neglected in the computation. This flow field differs from Figure 13 only in the nearest vicinity of the engine. Therefore, in recirculation model experiments, one can reduce the realistic sink strength of the engine intake, which can usually be attained only with great experimental difficulty, without falling into serious error.

In Figure 16, where a nozzle Mach number of 0.7 was used, the sink strengths of the free and wall jet, for which there are no measurements, have been estimated. Now the separation point jumps back dangerously close to the engine. The rising hot air now has only a very short path to traverse back to the engine intake. Along this path it can hardly find time for significant cooling. Therefore engines with low-velocity exhaust gas streams are more endangered by recirculation than those with high velocity.

Increasing the height of the engine above the ground (Figure 17) can affect the recirculation flow field only in the immediate neighborhood of the free jet. Because its sink strength is quite small in comparison to the wall jet, the free jet, now longer, has no long-range effect on the secondary air flowing around it. Furthermore the sink strength of the wall

jet and its effect on the recirculation flow increases more with greater nozzle distances.

Figure 18 shows the recirculation flow field of the RB 202 engine. Its high-volume supporting jet with its low specific impulse has a short separation distance and is, therefore, one of the configurations severely endangered by recirculation. In order to attain a low overall height relationship, the mathematical model of the RB 202 differs from that of the RB 162 in having the engine intake one nozzle diameter above the level of the nozzle and the point source for generating the intake dipole flow only one diameter below the intake sink.

/29

3.2 Recirculation Temperatures

3.2.1 Description of the model for temperature calculation

Now we shall consider the calculation of the temperature distribution in the recirculation flow field. In the recirculation the hot gas wall jet separated from the ground is the only heat source for the secondary flow. The hot free jet and the unseparated wall jet do not contribute to heating the surroundings. The air about them which is heated by convection and turbulent mixing is continuously sucked into them and carried away with the jet. Warming of the air particles by radiation from the exhaust gas jet is excluded because of the low absorption coefficient of air.

In calm air, the rotationally symmetric wall jet separates from the ground along a circular arc due to the predominance of the thermal buoyancy forces. The continued movement of the warm air in the atmosphere is determined solely by the lift forces and the injection effect of the supporting jet. When

the wind is blowing, though, the separation is forced by kinetic forces, the line of separation deforms into half an ellipse, and the further expansion of the separated warm air cloud continues under the prevailing effect of the wind flow. The mathematical treatment of the process is considerably simplified by the fact that the elliptically deformed separation line (Figure 4) runs approximately parallel to the x axis in the vicinity of the /30 central section (y axis). In comparison to the rotationally symmetric case, now, the blowing back of the warm air onto the symmetry line of the recirculation flow process can be considered quite well as a plane process. The separation line is separated by an infinitely long slot of variable width, from which hot gas exits with excess temperature and the initial momentum. The expansion of this plane hot gas jet into the atmosphere is treated first in Section 3.2.2, completely isolated from the recirculation problem considered here. The velocity, temperature, and width of the rising warm air flow are calculated without the external wind effect and the sink action of the wall jet. Only in Section 3.2.3 are the results of this calculation applied to the recirculation flow.

The calculation of the plane ascending flow with initial momentum can also be evaluated simultaneously as the mathematical description of the expansion laws of the hot gas fountains between two wall jets flowing into each other, which is not treated in this work.

3.2.2 Plane ascending flow

In the literature, theoretical investigations on ascending flows are published primarily on point-shaped heat sources (rotationally symmetric case) for which, in a neutral atmosphere, the movement of the air stream occurs solely due to the buoyancy force. Schmidt [57] has worked theoretically and experimentally

with the expansion process of warm air over point and line sources in a neutral atmosphere. We have learned of other studies from England, such as those of Rankine [48] and Rouse et al. [54]. Morton [43], Priestley and Ball [47], Murgai and Emmons [45] and Sutton [70] have set up more general theories on free convection over point sources of heat.

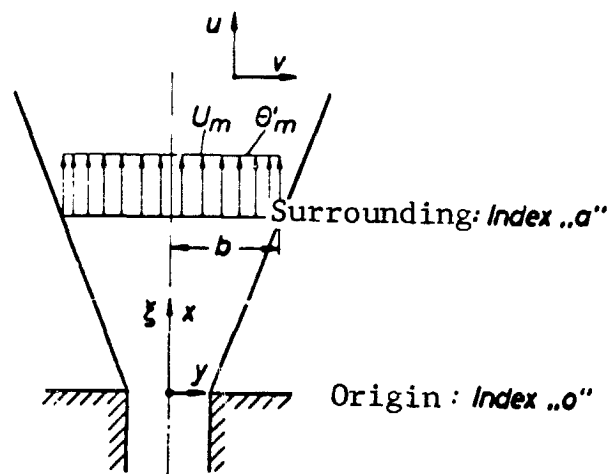


Figure 6. Coordinate system of a plane warm air source.

We begin with the equations given by Schlichting [56] for / 31 the flows of mass, momentum and heat. x is the coordinate in the direction of principal flow, (Figure 6), and y is the transverse coordinate. u and v are the corresponding velocity components.

Continuity equation:

$$\frac{\delta \rho \cdot u}{\delta x} + \frac{\delta \rho \cdot v}{\delta y} = 0 \quad (3.7)$$

Motion equation:

$$\rho \left(\frac{\delta u}{\delta t} + u \frac{\delta u}{\delta x} + v \frac{\delta u}{\delta y} \right) = X - \frac{\delta P}{\delta x} + \mu \left(\frac{\delta^2 u}{\delta x^2} + \frac{\delta^2 u}{\delta y^2} \right) \quad (3.8)$$

Energy equation:

$$\rho \cdot c_p \cdot \left(\frac{\delta T}{\delta t} + u \frac{\delta T}{\delta x} + v \frac{\delta T}{\delta y} \right) = \lambda \left(\frac{\delta^2 T}{\delta x^2} + \frac{\delta^2 T}{\delta y^2} \right) \quad (3.9)$$

For the present case of recirculation flow, this equation system must be simplified by means of certain assumptions. Thus, the calculation is based on a steady flow, which is certainly a great simplification of this highly turbulent flow process. But the results show that the calculation with steady flow determines the average flow parameter with sufficient accuracy.

The pressure and friction terms are neglected in the motion / 32 equation, and the heat conduction and radiation in the energy equation. The potential temperature θ and turbulent fluctuation quantities are also introduced.

As shown in Appendix 9.3, consideration of all these assumptions leads to the new equation system which applies for plane turbulent convective flow in the earth's gravity field without wind:

Continuity equation:

$$\frac{\delta \bar{u}}{\delta x} + \frac{\delta \bar{v}}{\delta y} = 0 \quad (3.10)$$

Motion equation:

$$\rho \left(\bar{u} \frac{\delta \bar{u}}{\delta x} + \bar{v} \frac{\delta \bar{u}}{\delta y} \right) = \rho \cdot g \cdot \frac{\bar{\theta} - \theta_a}{\theta_a} - \rho \cdot \frac{\delta \tau}{\delta y} \quad (3.11)$$

Energy equation:

$$\rho(\bar{u} \frac{\delta \theta'}{\delta x} + \bar{v} \frac{\delta \theta'}{\delta y}) = - \frac{1}{cp} \frac{\delta q}{\delta y} - \rho \cdot \bar{u} \cdot \frac{d\theta_a}{dx} . \quad (3.12)$$

For certain assumptions about the velocity and temperature distribution of the warm air stream, these equations can be simplified and integrated. With simple free convection, in which the gas moves because of an excess temperature, i. e., a buoyant force, according to Sutton [71] the velocity profile of the circular warm air stream can be approximated by a Gaussian normal distribution

$$\bar{U}(x,r) = \bar{U}(x) \cdot e^{-r^2/b^2} \quad (3.13)$$

where \bar{U}_x is the velocity along the axis, b is a characteristic width of the upflow and r is the current radius. The integral then yields the simple value $b^2 \cdot U$. As Schmidt [57] has shown, the temperature and velocity profiles of a line source without initial momentum is identical to that of the round source. The Gaussian distribution function would, accordingly, also be the proper profile shape for the line source. In the recirculation flow considered here, the separation point at which the two gas streams, the wind and the wall jet, meet each other is replaced by a line source with initial momentum and excess temperature. /33

There have been no previous measurements of the velocity profile in such a plane "fountain", and it is difficult to make predictions about them.

In the further considerations, therefore, we assume a profile of the type such that the velocity within the upflow is a constant equal to the mean velocity $u_m(x)$. Outside, $u_m(x) = 0$. This assigns a fixed width $b(x)$ to the upflow (Figure 6).

The same consideration applies to the temperature profile. Although the exchange mechanisms differ for momentum and heat, for the present case of the plane buoyant flow the ratio of the width of the velocity profile to that of the temperature profile is set equal to 1. Thus, we are calculating with a rectangular profile, for which:

$$\left. \begin{array}{l} -b \leq y \leq +b \\ u(x,y) = u_m(x) \\ \theta'(x,y) = \theta'_m(x) \end{array} \right\} \text{ for } x = \text{constant} \quad (3.14)$$

The velocity with which the surrounding air flows into the ascending flow at the edge of the jet is \bar{v}_b . According to Morton-Taylor-Turner [44] the inflow velocity is proportional to the mean flow velocity in the x direction, with the proportionality factor remaining constant.

$$\bar{v}_b = \alpha \cdot u_m. \quad (3.15)$$

We can find α values for circular warm air sources in the literature. For the Gaussian profile, for example:

- $\alpha = 0.093$ measured by Morton-Taylor-Turner [44].
- $\alpha = 0.082$ according to Morton [43].
- $\alpha = 0.1$ according to Murgai-Emmons [45].

For a rectangular profile:

- $\alpha = 0.116$ according to Morton [43].

/34

Now the integrated equation system (the integration is described in Appendix 9.3) is:

$$\frac{d}{dx} u_m \cdot b = \alpha \cdot u_m \quad (3.16)$$

$$\frac{d}{dx} u_m^2 \cdot b = g \cdot b \cdot \frac{\theta'_m}{\theta_a} \quad (3.17)$$

$$\frac{d}{dx} g \cdot b \cdot u_m \frac{\theta'_m}{\theta_a} = -u_m \cdot b \cdot g \cdot \frac{1}{\theta_a} \frac{d\theta_a}{dx} \quad (3.18)$$

The recirculation flow considered here represents an initial value problem. For $x = 0$, we have:

$$\begin{aligned} b &= b_0 \\ u_m &= u_{m0} \\ \theta_m &= \theta_{m0} \end{aligned} \quad (3.19)$$

In order to obtain solutions independent of the initial values, it is convenient to introduce dimensionless quantities here:

$$\xi = \frac{\alpha \cdot x}{b_0} \quad (3.20)$$

$$\eta = \frac{b}{b_0} \quad (3.21)$$

$$\zeta = \frac{u_m}{(b_0 \cdot g)^{1/2}} \cdot \left[\frac{\alpha}{(\frac{\theta'_m}{\theta_a})_0} \right]^{1/2} \quad (3.22)$$

$$\lambda = \left(\frac{\theta'_m}{\theta_a} \right) / \left(\frac{\theta'_m}{\theta_a} \right)_0 \quad (3.23)$$

$$\gamma = \frac{1}{\theta_a} \cdot \frac{d\theta_a}{dx} \cdot \frac{b_0}{\alpha \cdot (\frac{\theta'_m}{\theta_a})_0} \quad (3.24)$$

Insertion of these quantities into Equations 3.16, 3.17, 3.18 leads to:

27

$$\frac{d}{d\xi} \zeta \cdot \eta = \zeta \quad (3.25)$$

$$\frac{d}{d\xi} \zeta^2 \cdot \eta = \eta \cdot \lambda \quad (3.26)$$

$$\frac{d}{d\xi} \zeta \cdot \eta \cdot \lambda = -\gamma \cdot \zeta \cdot \eta \quad (3.27)$$

Now the initial conditions are:

For $x = 0$:

$$\begin{aligned} \xi &= 0 \\ \eta_0 &= 1 \\ \lambda_0 &= 1 \\ \zeta &= \zeta_0 \end{aligned} \quad (3.28)$$

The unknowns are:

- η Parameter for the width of the ascending flow
- ζ Parameter for the velocity of the ascending flow
- λ Parameter for the temperature of the ascending flow
- γ Parameter for the temperature gradient; generally prescribed.

With the substitution

$$V = \eta \cdot \zeta \quad (3.29)$$

$$W = \eta \cdot \zeta^2 \quad (3.30)$$

$$Z = \lambda \cdot \eta \cdot \zeta \quad (3.31)$$

or

$$\lambda = \frac{Z}{V} \quad (3.32)$$

$$\zeta = \frac{W}{V} \quad (3.33)$$

$$\eta = \frac{V^2}{W} \quad (3.34)$$

we obtain the final differential equation system for the infinite / 36
line source with initial momentum and buoyancy force:

$$V \cdot \frac{dV}{d\xi} = W \quad (3.35)$$

$$W \cdot \frac{dW}{d\xi} = Z \cdot V \quad (3.36)$$

$$\frac{dZ}{d\xi} = -\gamma \cdot V \quad (3.37)$$

Initial conditions:

$$\begin{aligned} \xi &= 0 \\ V_0 &= \zeta_0 \\ W_0 &= \zeta_0^2 \\ Z_0 &= \zeta_0 \end{aligned} \quad (3.38)$$

As Hölscher [29] has shown, exact solutions to these equations
can be found for

$$\gamma = 0 \quad b_0 = 0 \quad u_m^2 \cdot b_0 = 0 \quad \theta'_m \neq 0$$

and

$$\gamma = 0 \quad \zeta_0 = 1 \quad \eta_0 = 1 \quad \lambda_0 = 1$$

The first case represents a linear source in the neutral atmosphere, for which the width and momentum are equal to zero at the origin. There is only one heat flow at the origin, which generates a buoyant force which sets the air into motion. In the second case, the line source has a very definite average initial velocity u_{m0} at arbitrary b_0 and θ'_{m0} . General solutions of the differential equation system can be obtained through numerical integration by the Runge-Kutta method. The calculation was done on an electronic computer for various values of γ . For the value of practical interest, $\gamma = 0$, the results are shown in Figures 19, 20 and 21 for variable initial parameter ζ_0 . / 37

For the initial value $\zeta_0 > 1$ the velocity ζ first decreases sharply and then approaches a constant value asymptotically. As ζ_0 increases, the constant final velocity and the width of the transition region increase until the final velocity is reached. For $\zeta_0 < 1$ the velocity increases until it reaches the constant final value. The width of the upflow grows linearly with the distance from the source and, at a given point, is greater for high values of ζ_0 than for low ones. The excess temperature in the upflow falls according to a hyperbolic function. The lower temperature drop at larger initial velocities causes stronger buoyant forces in the rising cloud, so that the constant final velocity is also greater at high ζ_0 values. At large ζ_0 values the upflow reaches a certain distance from the source sooner than with low initial velocities. It has less time for turbulent mixing with the outside air, so that for the same initial temperatures the faster warm air stream always has the higher temperature.

3.2.3 Ascending flow in the recirculation flow field

Now we shall investigate the ascending flow in the recirculation flow field. At the site of separation of the wall jet the warm air flows vertically upward, is caught by the wind,

turned into the direction of the wind, and then blown away. Then the cloud of warm air flies over the wall jet moving toward it, is sucked in by its sink action, and for the most part, consumed. This prevents penetration of ambient air into the underside of the hot gas cloud. To make possible a theoretical description of this complex flow process, we shall greatly simplify the recirculation process for further consideration so that the injection effect of the wall jet on the underside of the warm air flow is neglected. The recirculation flow is considered to be an ascending flow with initial momentum, turned in the direction of the wind. / 38

This phenomenon can be observed at any smoking chimney on a windy day. The smoke cloud is turned in the direction of flow shortly after leaving the source. Investigations of this turbulent expansion process have been made, particularly in relation to dust and waste gas concentration at the ground in the direction of the wind. Let us mention here, particularly, the works of Keffer and Baines [34] and of Bosanquet, Carey, Mech and Halton [4]. They attempted to determine the path of the smoke cloud theoretically and experimentally. The formulas stated there show how complicated the whole problem is. These publications are concerned with smokestacks which can be considered point sources. They make no statements about the temperature fields in the clouds, which are particularly interesting in relation to recirculation flows.

On the other hand, Rankine [48] has experimentally determined temperature fields behind linear heat sources across which the wind is flowing. Let us give some of his most important results here:

At constant wind velocity, the temperature boundary layer grows with the distance from the heat source, the maximum temperature decreases, and the temperature maximum moves to greater heights. This means that the warm air cloud becomes wider in the direction of wind flow and rises.

If the wind velocity is changed, then at a point $y = \text{constant}$, the temperature boundary layer becomes smaller the greater the velocity is. Correspondingly, the maximum temperature is higher. But this means that the time during which the turbulent mixing with the outside air occurs is very important. This agrees with the results for the ascending flow calculated previously. At a high initial velocity v_0 the temperature was higher than at low v_0 at an altitude $\xi = \text{constant}$.

The recirculation flow under consideration differs in important points from the flow which Rankine studies. Because of the presence of the initial momentum, we cannot deal with pure thermal convection in the recirculation flow.

/ 39

In spite of this complex flow process, we shall state here a simple method by which the state within the recirculation cloud can be calculated. Assume that the mechanism of turbulent mixing of the warm air cloud with the surrounding air under the influence of wind is the same as without the wind. This is certainly the case for the low wind velocities which we are considering. After the same times, the state of the warm air cloud rising in calm air is identical with that of the cloud in the wind. Then, with y the coordinate in the wind direction, x the coordinate in the direction normal to that, u_m the velocity in the x direction and w the mean wind velocity (Figure 7):

$$dy = w \cdot dt. \quad (3.39)$$

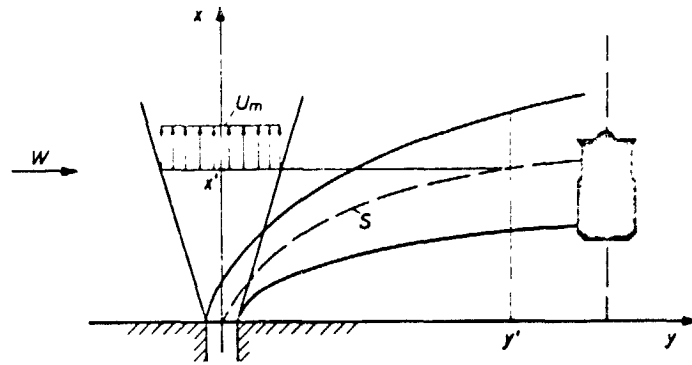


Figure 7. Coordinate system of a plane warm air source with a wind blowing across it.

If w is a constant value, then with the coordinates of Figure 7,

$$y = w \cdot t.$$

The time for the vertically rising cloud to move from the source to coordinate x' can be calculated from

$$u_m(x) = \frac{dx}{dt} \quad (3.40)$$

$$dt = \frac{dx}{u_m(x)}$$

$$t = \int_0^{x'} \frac{dx}{u_m(x)} \quad (3.41)$$

In the same time, the cloud in the wind moving with velocity w reaches the coordinate y'

$$y' = w \cdot \int_0^{x'} \frac{dx}{u_m(x)} \quad (3.42)$$

In this way, every point y in the wind direction is assigned a state of the vertically rising cloud without wind. For the practical calculation, the recirculation velocity $w(y)$ and the time t required for an air particle to move from the separation point R along path a with the recirculation velocity $w(y)$ to the engine on the z axis are determined by means of the recirculation flow pictures, Figures 13 to 18.

$$t = \frac{w(y)}{s} . \quad (3.43)$$

In this time, a rising thermal cloud moves with the velocity $u_m(x)$ along the vertical path distance x'

$$x' = \frac{u_m(x)}{t} \quad (3.44)$$

and at this position it has the same excess temperature as the recirculation flow at the height of the engine. In this way, the recirculation problem is reduced to the expansion process of the plane ascending cloud rising vertically, calculated in Section 3.2.2.

3.2.4 Calculation of the recirculation temperatures

/41

Now the temperatures of the recirculation flow fields can be calculated with the aid of the formulas developed in the last two sections. As the temperatures near the engine are the most interesting, the following example shows the calculation of the average excess temperature on the z axis.

We choose engine configurations with a nozzle Mach number $M_o = 1$ and constant $H/D = 3$. The ambient temperature $\theta_a = 288^\circ\text{K}$. From the model experiments we take:
The separation radius R , treated here as the beginning of separation, which is about 20% ahead of the values plotted in

Figure 11.

The maximum temperature θ_{\max} of the wall jet at the point of separation, according to Figure 96.

The maximum velocity U_{\max} of the wall jet at the point of separation, according to Figures 98 and 99.

The thickness h' of the wall jet at the site of separation, from the ground up to $U = 0$, according to Figures 87, 88 and 104.

The mean recirculation velocity W between the point of separation and the engine, taken from the flow pictures in Figures 13 to 18.

The averages of the temperature and velocity are taken by planimetry of the temperature and velocity profiles of the wall jet as far as the velocity zero point, and establishing a rectangular profile of the same area.

The first table shows the parameters which can be determined from the studies which have been done. The calculation and its intermediate results are shown in the second table.

Selected configu- ration θ_0	R \bar{D}	Original R	Model R	θ_0	$\frac{\theta_{max}}{\theta_0}$	θ_{max}	$\theta_m \approx 0,8 \cdot \theta_{max}$	$\frac{\theta'_m}{\theta_a}$	u_0	$\frac{u_{max}}{u_0}$	u_{max}	$u_m \approx 0,42 \cdot u_{max}$	w	Original h'	Model h'
θ_C		m	m	θ_C		θ_C	θ_C		$\frac{m}{s}$		$\frac{m}{s}$		$\frac{m}{s}$	m	m
8 600	37	17,6	1,85	600	0,035	21	17	0,059585	585	0,023	13,5	6	9	1,7	0,18
14 400	23	11	1,15	400	0,052	21	17	0,059520	20	0,038	20	9	14	1,1	0,115
14 600	23	11	1,15	600	0,052	31	25	0,087585	21	0,036	21	9	14	1,1	0,115
14 800	23	11	1,15	800	0,052	42	34	0,118650	21	0,032	21	9	14	1,1	0,115
14 1000	23	11	1,15	1000	0,052	52	42	0,146700	20,3	0,029	20,3	9	14	1,1	0,115

Original engine										Model engine									
b_0	t	x'	ζ_0	ξ	λ	θ'_m	b_0	t	x'	ζ_0	ξ	λ	θ'_m	b_0	t	x'	ζ_0	ξ	θ'_m
m	s	m				θ_C	m	s	m				θ_C	m	s	m			θ_C
8 600	0,85	2	12	2,7	1,4	8,3	0,09	0,2	1,2	8,3	1,34	0,52	8,8	0,09	0,2	1,2	8,3	1,34	8,8
14 400	0,55	0,8	7,2	5,1	1,3	8,8	0,06	0,08	0,72	16	1,26	0,53	9	0,06	0,08	0,72	16	1,26	9
14 600	0,55	0,8	7,2	4,2	1,3	13	0,06	0,08	0,72	13	1,26	0,53	14,2	0,06	0,08	0,72	13	1,26	14,2
14 800	0,55	0,8	7,2	3,6	1,3	17	0,06	0,08	0,72	11	1,26	0,53	15	0,06	0,08	0,72	11	1,26	15
14 1000	0,55	0,8	7,2	3,2	1,3	21	0,06	0,08	0,72	10	1,26	0,53	16	0,06	0,08	0,72	10	1,26	16

*Commas represent decimal points.

To calculate the equation

143

$$\zeta_0 = \frac{u_{m0}}{\sqrt{b_0 \cdot g}} \sqrt{\frac{\alpha}{(\frac{\theta'_m}{\theta_a})_0}} \quad (3.22)$$

the quantities u_{m0} , b_0 and α must be determined. θ_a , the potential temperature of the surroundings, is set equal to the actual surrounding temperature. θ'_m is the average excess temperature of the warm air in relation to the surroundings. u_{m0} is the average initial velocity of the rising warm air. In the present example, it is the vertical component of the wall jet velocity after separation. Here it is assumed that it is identical to the average wall jet velocity u_m before separation. b_0 is half the initial width of the rising warm air stream. Here, the wall jet thickness h' before separation is chosen as the initial width of the warm air. The following rough calculation confirms these assumptions:

In the first configuration of the example the separation radius $R = 17.6$ m, the wall jet thickness $h' = 1.7$ m, the mean initial velocity $u_{m0} = 6$ m/s. The rising volume flow

$$\dot{V} \approx 2\pi R \cdot h' \cdot u_{m0} = 1130 \text{ m}^3/\text{s}.$$

According to Section 3.1.3, the volume flow for this configuration must be equal to $1,300 \text{ m}^3/\text{s}$ at the point of separation. As the two volumes differ only insignificantly, we can set:

$$2 \cdot b_0 = h' . \quad (3.45)$$

The parameter α for the plane low velocity free jet is determined by means of the velocity profile published by Liem [38] for plane cold gas jets and the inflow velocities given there. For α we obtain values between 0.103 and 0.107. As a temperature rise 44

reduces the ratio of the inflow velocity to the mean jet velocity somewhat (Figure 9), a slightly lower value is selected for the recirculation flow:

$$\alpha = 0.10.$$

The value stated by Morton-Taylor-Turner [44], $\alpha = 0.116$, does not appear suitable for the example being investigated. The expression

$$\xi = \frac{\alpha \cdot x'}{b_o} \quad (3.20)$$

contains the height of rise of the warm air cloud, x' (Figure 7). For the calculation, we first determine the time t required for an air particle to move from the point of separation, R , with the mean recirculation velocity w , to the engine on the z axis. In this time, the warm air flow moves the vertical distance x' while maintaining the ascending velocity u_m .

Now, with the quantities ζ_o and ξ known, the value of λ is read from Figure 21. From the relation

$$\lambda = \frac{\theta'_m / \theta_a}{(\theta'_m / \theta_a)_o} \quad (3.23)$$

we can now determine the desired mean excess temperature θ'_m of the recirculation flow in the vicinity of the engine.

In order to show that the calculation gives almost the same temperatures in the model and the full-scale design, the results for both engine dimensions are compared in the table.

Now we shall check whether the assumption made in Section 3.2.2 about the order of magnitude of the parameter γ for the temperature gradients of the surroundings is also justified

for the example under study. According to Equation 3.24,

$$\gamma = \frac{1}{\theta_a} \cdot \frac{d\theta}{dx} \cdot \frac{b_o}{\alpha \cdot (\theta'_m / \theta_a)_o} \quad (3.24)$$

$\frac{d\theta}{dx}$ is a measure of the stability of the air stratification. We / 45 shall select the mean value for the ICAO standard atmosphere (neutral atmosphere)

$$\frac{d\theta}{dx} = -0,65 \text{ [}^\circ\text{C/100 m]} .$$

With the other values listed in the two tables we obtain

$$-0,00093 < \gamma < -0,00226 .$$

Therefore the assumption we made, that $\gamma = 0$, is justified.

4. Experiments

4.1 Experimental design and measuring technology

The VTOL supporting jet studies were performed on the ground-effect test system of the DFVLR Institute for Air-Breathing Engines at Braunschweig (Figure 8). The test system, which is described in detail in [13], is in a large room, 10 x 20 m, which can be moved on rails. A single model lift engine blasts vertically downward onto a platform. In order that the results would not be falsified by the ambient temperatures with long blast periods, all measurements were always done in the open air with the room rolled away. Thus, even with a wind machine blowing against the recirculation flow field, no disturbances could occur from the adjacent room walls.

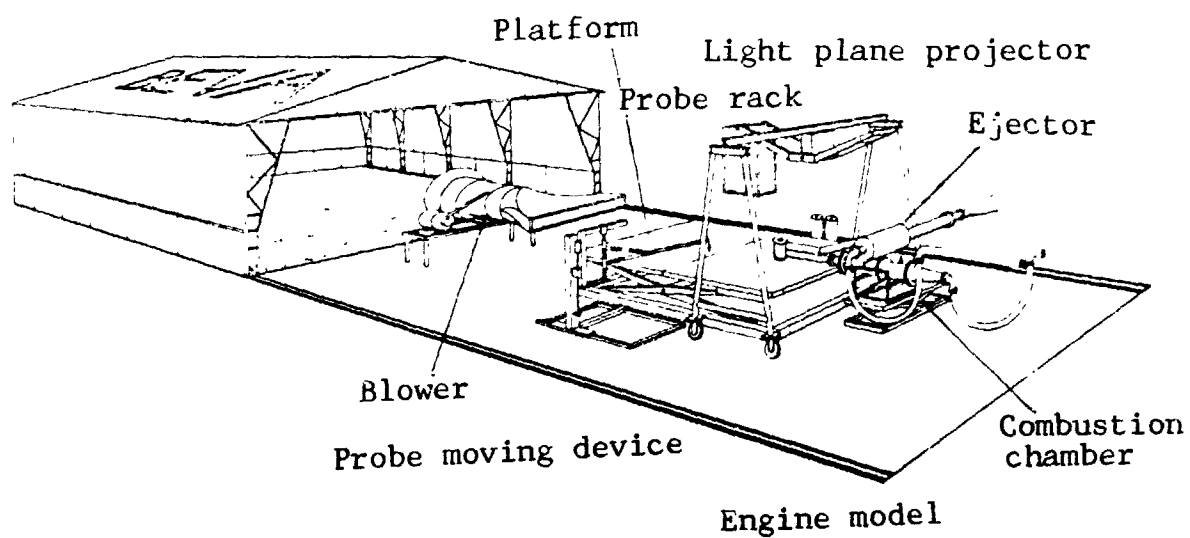


Figure 8. Ground effect test system.

At the engine intake, a compressed air-driven ejector sucks in air and blows it away from the test stand into the open air. The sink effect of quite different lift engine intakes can be simulated with the ejector suction system, consisting of a primary nozzle, secondary air chamber with a controllable suction line, mixing tube, Venturi nozzle and diffuser. The ejector works with a critical pressure ratio on the primary side, and is supplied from a rotary piston compressor ($\dot{m} = 0.8 \text{ kg/s}$, $\Delta p = 1 \text{ bar}$). The bypass ratio of the ejector can be controlled with a continuously adjustable iris diaphragm in the suction tube.

The air for the exhaust gas jet was supplied by a rotary piston compressor which supplied up to 1 kg/s at a maximum back-pressure of 3 bar . The air was led to a combustion chamber through a segment 10 m long (113 mm inside diameter). There it was heated by burning of JP 1. The air throughput was determined by means of a calibrated diaphragm in the tube ahead of the combustion chamber. As one section of the compressed air line between the compressors and the model consisted of flexible steel hose, the lift engine, with its entire ejector and combustion chamber system could be moved upward smoothly by hydraulic power. / 47

The wind effect on the ground effect was simulated by a high-volume blower ($\dot{V} = 20 \text{ m}^3/\text{s}$). The blown air moved through a jet guide system with several flow directors, arriving at the engine model platform without twist. As the blower, driven by a synchronous electrical motor, had no control of the rotation rate, the wind velocity could be changed only by blocking the intake cross section of the blower with throttle rings of different sizes.

All the recirculation tests were done with two different engine models. The two models differed only in their height. While Model 1 (Figure 24) had a total height of 7 nozzle diameters,

Model 2 (Figure 25) attained a height of 4 nozzle diameters through adept design of the suction line. The extremely short dimensions of the RB 162-31 engine, with a total length of 3 nozzle diameters, could not be realized with a model of this type, with separate air supply lines.

The temperature at the engine intake was measured with nine 0.5 mm thick Ni/Cr-Ni thermocouples distributed across the intake cross section.

The VTOL supporting jet was visualized with the light section method (Figure 32). For this, a non-burnable powdery contrast agent (silicon dioxide) was blown with compressed air into the hot gas line. It colored the supporting jet white.

A 6,000 watt light plane projector (Figure 26), during the darkness of night, radiated an arbitrarily selectable plane only a few millimeters thick over the entire flow field, so that an observer standing perpendicular to it could see the flow conditions in this plane. The deflection of the wind flow by an opposing wall jet and the flow directions in the secondary field were also visualized with the light section method. A contrast medium (silicon dioxide) with particles which were large, but which had a negligibly small sedimentation rate, so that they could follow the movements of the flow without inertia, is blown into the secondary flow field, making the flow visible in the light section. The flow was photographed with exposure times of $1/15$ second, using a sensitive camera ($1/0.95$). /48

In the secondary flow field, velocities were measured with temperature-compensated hot film transducers, working by the constant temperature method. In the transducer, there is a glass wire stretched between two points. The wire is 3 mm long and 0.15 mm thick, coated with a quartz film and then coated

with vapor-deposited quartz. This type of transducer was suited for velocity measurements of Mach 0 to 1, and can be exposed to excess temperatures up to 400°C. The temperature compensation is done with a resistance thermometer in the transducer socket, so that the wire temperature is always maintained at 230° above the ambient temperature. Temperature and velocity fluctuations with time were measured with UV-light recorders and storage tube cathode ray oscilloscopes.

The measurements were plotted fully automatically by means of a digital data processing system which interrogated the measurements at a rate of 5 measuring points per second, and recorded them on punched tape. The evaluation was done in the computer center of the DFVLR, Braunschweig, with a Siemens 40004/45 computer.

4.2 Measurement of the recirculation velocities

/49

Velocity measurements in the recirculation flow field of lift engines require a great expense for measuring technology, because it deals with highly turbulent hot air streams in which the velocity and temperature fluctuations can even exceed the value in the principal flow direction. The impact pressures of the recirculation flow are on the order of only a few mm water, so that pitot probes are unsuitable for velocity measurement. Furthermore, pitot probes are directional, and would have to be pointed in the main flow direction for measurement; but this is usually not known at all. Because of its high degree of turbulence, the recirculation flow at times blows obliquely even on those pitot probes aligned in the main flow direction, leading to erroneous measurements. Because of the temperature variations which occur, hot wire probes are not suited for velocity measurements in the recirculation flow field. Furthermore, the lifetime of such probes would be very limited because of the unclean

engine exhaust gas and the particles torn up from the ground by the wall jet, transported in the flow field, and thrown against the hot wire. In these studies, therefore, temperature-compensated hot film transducers were used. They are mechanically stronger than hot wires.

The velocities in the recirculation flow field were measured at certain points in the y-z plane with hot film transducers (Figure 28). Because of the high turbulence, 40 successive measurements of the instantaneous velocity were made at each measuring point. The arithmetic mean

$$\bar{x} = \frac{1}{N} \sum_{i=1}^N x_i \quad (4.1)$$

and the standard deviation

$$s = \sqrt{\frac{1}{N-1} \sum_{i=1}^N (x_i - \bar{x})^2} \quad (4.2)$$

/ 50

were calculated. Figures 28, 29, and 30 show \bar{x} and s . In these experiments, the mass flow sucked in at the engine intake was always kept equal to the nozzle mass flow.

A striking feature of the recirculation measurements is the high turbulence of the flow, which appeared with velocities in two different frequencies, once as a fluctuation above 10 Hz and then again as a low-frequency fluctuation below 1 Hz. The velocity fluctuations recorded by a hot film probe in the recirculation flow field are plotted as analog values versus time in Figure 31. Measurements become problematical where the turbulent fluctuation velocities in the main flow direction exceed the mean velocity, so that the local velocity changes its sign. Due to their construction, hot wire probes measure the velocity without sign, and do not differ between forward and rearward air movement.

The experiments established that a change in sign of the local velocity due to the high turbulence occurred only in the case without the wind blowing. Here it was impossible to determine the mean velocity through hot wire measurements alone. Only measurement of the impact pressure yielded the true mean, which was almost half as large as the value from averaging all the hot wire measurements without considering the change in sign.

The flow directions at the measuring points were determined with wool fibers and light section photographs (Figure 36). The light section photographs explained the physical process of recirculation particularly well. The engine waste gas jet is marked in Figure 32, while the wind remains unmarked. In Figure 33 / 51 contrast powder is blown into the lowest layer of the wind flow while the exhaust gas jet remains invisible. The course of the boundary line between the walljet air and the wind, which can be read from the photographs, is different with the two marking methods. For instance, when the wall jet is marked, the line of separation describes a higher arc than with the wind marked. The cause of this is the turbulent mixing of the marked and unmarked air. The visible boundary line is the outermost course of the turbulence balls from the marked flow which penetrate into the dark flow. The visible boundary line with the wall jet marked and the wind unmarked has the greatest predictive power for recirculation studies, because it describes the maximum height to which the air heated by the engine jet can arrive. If the engine intake is below this line, we must expect a temperature rise due to recirculation. If the intake is above it, only cold surrounding air is drawn in. The measurement of this temperature boundary line is described in Section 4.3.

In the measurements, because of the test system, there was a deviation of the recirculation flow of the model from the original flow. This was due to the fact that the profile of the

wind velocity from the blower dropped off with increasing height and increasing distance from the middle plane. In the model tests, the recirculation flow lines described wider arcs, which did not confirm the calculation (Section 3.1.3). Flows directed upward were deflected less strongly at greater height because the wind was falling off less there, so that they could rise higher.

A second effect, causing even more error in the recirculation measurements, occurred particularly at low wind velocities. The wind profile, dropping off transversely to the middle plane, blew with a lower velocity against points at the side of the wall jet than against those in the middle. Thus, in these marginal areas, the flow length of the wall jet increased up to its separation. The separation line took on rather a straight course instead of an elliptical one (Figure 37). This form of the separation line made possible transport of wall jet air toward the central plane, which then increased the flow velocities in the plane of symmetry. This cross flow caused the high recirculation flow velocities at great distances above the ground. These were almost twice as high as the wind velocities prevailing at this height. This, too, contradicts the calculation (Section 3.1.3) because the recirculation velocity can be only slightly greater than the local wind velocity. / 52

These errors in the recirculation measurements would not occur if such tests were performed in an appropriate wind tunnel with a rectangular velocity profile.

4.3 Measurement of the recirculation temperatures

In the recirculation flow field and at the engine intake, the temperature was measured with 0.5 mm thick NiCr-Ni thermocouples. The measurements were repeatedly interrogated by a data

processing system and averaged, and also plotted versus time by a recorder, so as to learn the turbulent temperature fluctuations. The averaging and calculation of the standard deviation followed the equations given in Section 4.2. The results of the temperature measurements in the recirculation flow field can be seen in Figures 28, 29 and 30. Figure 38 presents a recording of measurements obtained with a temperature probe moved in the recirculation flow field by means of a probe moving device. These temperatures were plotted versus time and path.

In Figures 39 and 40, on the other hand, the temperature is plotted only versus the path. The boundary line between the recirculation flow heated by the engine jet and the wind blowing at ambient temperature can be seen most clearly with this presentation. This recirculation boundary line was defined as the location where the temperature profile has dropped off to 10 to 20% of its maximum value. This separation line is identical with the visible boundary between the marked wall jet and the dark wind air on the light section photographs (Figures 34 and 35). It can, then, be determined without temperature measurements, solely by marking the engine jet and illuminating it with a light plane projector. / 53

Measurements of the temperature profile of the recirculation cloud on the z axis in height above the engine were done at a wind velocity of 14 m/s, although for technical reasons it had to be done 200 mm in front of the central axis of the engine. It established that the temperature profile for both engine models increased to its maximum value some 6 nozzle diameters above the ground and then gradually decreased upward to the value of the ambient temperature. The temperatures averaged over a period of 30 seconds, and the maximum values which occurred, are plotted versus temperature in Figure 41. From this presentation we can see clearly that engines with compressor intakes low above the

ground suck in warmer regions of the recirculation cloud and are, therefore more endangered by recirculation than those with high intakes. In Figure 42, the recirculation temperatures measured for various nozzle temperatures are plotted for the maximum of the temperature profile, in the plane $z = 6D$.

For both engines, the engine intake temperatures were measured with thermocouples in the intake plane. Figure 43 shows a temperature curve recorded over thirty seconds in this way. In contrast to the intake air temperatures of lift engine arrangements with which fountains occur, the temperature distribution in the intake plane is quite even with wind recirculation. There is only a slight increase in temperature toward the windward side.

As the flow line pictures (Figure 12) suggest, configurations /54 without the wind blowing show no increase of the average engine intake temperature. If we superimpose a wind velocity on the flow field and compare the corresponding configurations at the wind velocities studied, then we establish that the temperature rise at the engine intake due to recirculation increases as the wind velocity decreases. While practically no excess temperature was measured with a wind of 20 m/s, the mean temperature rise for the configurations susceptible to recirculation was about 7°C for a 14 m/s wind and 10°C with an 8 m/s wind. The position of the temperature boundary line provides the explanation: At low wind velocities, the temperature limit of the recirculation flow is higher above the ground. Correspondingly, the maximum in the temperature profile also shifts upward, reaching or even exceeding the height of the engine intake.

The mean intake temperatures of Model 2, with its low height ratio, differ from those of Model 1 in that they are higher by about 3°C in the Model 1 configurations, which are susceptible to recirculation. This is because the intake for

Model 2 was lower under the temperature boundary line and so sucked in warmer regions of the recirculation flow. For some configurations of the Model 2, severe temperature increases occurred in the intake, while Model 1 showed no recirculation for the corresponding configurations. These would be the recirculation limiting cases, in which the intake of the high engine model was above the temperature boundary line, while the flat-designed engine model was already washed over by the heated recirculation cloud.

5. Comparison of the theoretical and experimental results

/ 55

In Figure 44, the calculated velocities of the secondary flow field from Figure 12 are compared with the measured velocity vectors from Figure 28. They agree well with each other in magnitude and direction. At this configuration, recirculation flow which would increase the engine intake temperature cannot occur. The hot exhaust gas jet has no effect on the temperature of the intake air. The lifting engine draws in only cold surrounding air.

All the other configurations investigated with wind effect cannot be compared with each other so simply, as here the experiment is detectably falsified by the mass transport to the symmetry plane described in Section 4.2. The wide arc of the recirculation flow lines after separation, shown by the measurements (Figures 29, 30) do not describe the calculated flow lines (Figures 13 to 18). This gives rise to the idea of seeking a deficiency in the test design as the cause for the course of the flow diverging from the theory. Nevertheless, the flow pictures show clearly that the wind velocity impresses itself predominantly on the recirculation field, and all flow velocities are of the order of magnitude of the local wind velocity. After separation, the wall jet air is caught up by the wind, turned back sharply, and drawn in

again by the wall jet.

In summary, we shall emphasize here that only a steady laminar isothermal flow field is calculated with the potential theory model. This is not identical with the actually highly turbulent and heated recirculation flow. Conclusions about turbulent mixing processes, such as the determination of the boundary line between warm wall jet air and cold wind flow, obviously cannot be drawn. But the experiments confirm that mean turbulent velocities and their directions in the recirculation flow field agree with those calculated theoretically. The mathematical method is able throughout to determine the principal flow which is important for understanding of the recirculation process and fundamental to the complex flow field. In addition the calculation can also indicate clearly the parameters which have the greatest effect on the flow picture.

/56

In Figure 42, the temperatures of the recirculation cloud at the height of the engine central axis are compared with the results of the calculation in Section 3.2.4. The agreement of the computations with the time-average measurements is very good. While we dealt with averages of the entire temperature profile with the calculated θ'_m values, the measurements are temperatures at the profile maximum, so that they are slightly greater.

As there is a drop in temperature at the engine intake from the upwind to the downwind sides, the temperatures θ'_m calculated for the configuration under consideration could be considered as representative temperatures for the whole intake plane for computing the engine thrust loss.

The temperatures measured in the intake of the Model 1 engine are compared with the calculated values in Figure 45. Here, too, there appears a good agreement between the theoretical

and the experimental results. This might provide the proof that the theory set up here provides quite accurate data on the recirculation temperature occurring at the engine intake.

Figures 46 and 47 provide diagrams for the practical person. From these figures, he can read the results of the recirculation theory directly in the parameters of interest to him. By means of Figure 46 one can judge whether the engine configuration being studied is endangered by recirculation. The upper limits of the recirculation clouds visible on the light section photos at the height of the engine center axis are plotted versus the wind velocity in this diagram. Engine intakes arranged high above the ground are always less sensitive to recirculation than those with low intakes. Only at low wind velocities could the temperature boundary line rise above high engine intakes, bringing even such configurations into danger from recirculation. No effect of the nozzle temperature on the course of the boundary line could be detected. If for a certain configuration the point of intersection from the normalized ground distance, z/D , of the intake, and from the wind velocity, is below the curve plotted with the appropriate engine parameters (Nozzle Mach number and H/D) then we have an engine arrangement which is susceptible to recirculation. / 57

Now the temperature rise which occurs can be taken from Figure 47. Depending on whether we have a H/D configuration in which the jet core strikes the ground or not, one moves up in one of the right-hand columns above the nozzle Mach number M_0 to the prevailing wind velocity w . From this ordinate value, one now draws a straight line to the origin in the left half of the diagram. Now the mean intake temperature rise can be read above the nozzle temperature.

The question of how the transient peak temperatures, which certainly must affect the dynamic behavior of the lift engine, can be calculated must remain open, however. From the measurements, they are not directly proportional to the means. The calculation of such temperature fluctuations will probably be successful only with better understanding of the turbulence.

6. Summary

The physical process of wind recirculation was treated in detail. This type of recirculation flow will appear more seriously in future VTOL aircraft. It is favored by the present trend in engine development to jets with more and more volume and lower specific impulses. / 58

For a single engine blasting vertically onto the ground, the mean velocities of the three-dimensional recirculation flow generated by wind were calculated by potential theory. Average recirculation temperatures were determined by using the expansion laws of warm air clouds. These were tested and confirmed by model measurements. The velocities and temperatures at the engine intake plane can be predicted with sufficient accuracy by the process described if the wind velocity, engine geometry, and nozzle conditions of the exhaust gas jet are stated. Treatment of the wind recirculation as a potential flow is allowable because it can be demonstrated that the kinetic forces occurring in the secondary field are always more than an order of magnitude greater than the thermal forces.

The investigations of the recirculation flow field led to the following results:

For a single VTOL supporting jet, no recirculation can occur without the wind blowing.

The course of the temperature boundary line, visualized with the light section method, is a suitable criterion for judging whether warm air can arrive at the engine intake through recirculation flow.

The recirculation velocities induced from a rotationally symmetrical exhaust gas jet differ only slightly from the local wind velocities, which prevail over the entire flow field. On the other hand, the recirculation velocities of a plane engine jet (series of engines) can amount to a multiple of the wind velocity [60].

/ 59

Wind recirculation to the engine intake is favored by:

Low wind velocities

Engine intakes arranged low above the ground

High exhaust gas temperature

Low exhaust gas velocity.

Aids against wind recirculation:

While the aircraft manufacturer can avoid fountain recirculation through design measures in the airframe and through suitable engine arrangement, he is largely powerless against wind recirculation.

There will be no jet engines not sensitive to recirculation which will accept an increase in temperature of the intake air without thrust loss as long as vertical takeoff aircraft use air-breathing engines. In any case, it is possible to develop engines which will "endure" the uneven intake condition (inlet distortion) without severe power loss. For recirculation reasons, the jet engine would have to exhibit a low exhaust gas temperature at the same time as a high specific impulse. But such a solution is excluded by the thermodynamic cycle. Engines with high

specific impulse but simultaneously high exhaust gas temperature encounter environmental protection measures because of their greater noise development.

Probably there remains only the possibility of avoiding dangerous wind recirculation by appropriate takeoff procedures. The R/VTOL procedure (rolling vertical takeoff and landing) described in [52] would be conceivable. In this procedure the takeoff and landing could occur with a tail wind and a horizontal velocity of the aircraft which would have to be equal to the mean wind velocity. This horizontal velocity, which the aircraft would generate itself, should keep the warm air clouds moving over the ground away. The aircraft would need to assume this velocity only in the very lowest takeoff and landing phases near the ground (perhaps up to 15 m altitude) and that could hardly injure the advantages of VTOL equipment.

/ 60

Dipl.-Ing. Eckart Schwantes
Institute for Air-Breathing Engines
German Research and Test Institute for Aeronautics
and Astronautics, Braunschweig.

7. References

1. Alvermann, W. and P. Stottmann. Temperaturmessung mit Thermoelementen in Verbrennungsgasen (Temperature Measurement with Thermocouples in Combustion Gases) DLR-FB 64-18, 1964.
2. Baehr, H. Thermodynamik (Thermodynamics), Springer-Verlag, 1962.
3. Bakke, P. An Experimental Investigation of a Wall Jet. J. Fluid. Mech. Vol. 2, 1957, pp. 467 - 472.
4. Bosanquet, C., W. Carey, M. Mech and E. Halton. Dust Deposition from Chimney Stacks. The Institution of Mechanical Engineers Proceedings. Vol. 162, No. 3, 1950, pp. 355 - 367.
5. Behnert, R. Untersuchungen zur Ähnlichkeitsmechanik von heißen und kalten Strahlen und Strahlgruppen, insbesondere zur Modelltechnik von VSTOL-Fluggeräten (Investigations on the Similarity Mechanics of Hot and Cold Jets and Jet Groups, Particularly for the Technology of Modeling VSTOL Aircraft.). VFW-Report Ea-268, March 1971.
6. Bradbury, L. and M. Wood. The Static Pressure Distribution Around a Circular Jet Exhausting Normally from a Plane Wall into an Airstream. British Aeronautical Research Council Current Paper 822, 1965.
7. Bradshaw, P., D. Ferries and R. Johnson. Turbulence in the Noise-Producing Region of a Circular Jet. AGARD-Report 450, April 1963.
8. Bradshaw, P. and E. Love. The Normal Impingement of a Circular Air Jet of a Flat Surface. British Aeronautical Research Council, Reports and Memoranda, R.+M. No. 3205, Sept. 1959.
9. Bronstein, I. and K. Semendjajew. Taschenbuch der Mathematik (Pocket Book of Mathematics). 1967, Harri Deutsch.
10. Corrsin, S. and M. Uberoi. Further Experiments on the Flow and Heat Transfer in a Heated Turbulent Jet. NACA Report 998, 1950.

11. Cox, M. and W. Abbott. Studies of the Flow Fields Created by Single Vertical Jets Directed Downwards Upon a Horizontal Surface. National Gas Turbine Establishment, Pyestock, England, NGTE M, Vol. 390, Oct. 1964.
12. Crowe, C. and H. Riesebieter. An Analytic and Experimental Study of Jet Deflection in a Cross-Flow. Vortrag beim AGARD Fluid Dynamics Panel Meeting Göttingen, Sept. 1967, AGARD Conference Proceedings No. 22.
13. Dissen, H. and E. Schwantes. Versuchsanlage für Bodeneffektuntersuchungen bei Kurz- und Senkrechtstartern (Test System for Investigating Ground Effects with Short and Vertical Takeoff Aircraft). DLR-Report 68-29, Oct. 1968.
14. Ebrahimi, I. Turbulenz in isothermen Freistrahlen und Freistrahlfammen (Turbulence in Isothermal Free Jets and Free Jet Flames). Dissertation, Karlsruhe Technical University, Dec. 1967.
15. Eckert, E. Einführung in den Wärme- und Stoffaustausch (Introduction to Heat and Material Exchange). Springer-Verlag, 1966.
16. Eickhoff, H. Statischer Druck und Turbulenz in drehsymmetrischen Freistrahlen (Static Pressure and Turbulence in Rotationally Symmetrical Free Jets). Dissertation, Karlsruhe Technical University, July 1968.
17. Fiedler, H. Theoretische und experimentelle Analyse des statischen Drucks im ebenen turbulenten Freistrahle bei kleiner Machzahl (Theoretical and Experimental Analysis of the Static Pressure in a Plane Turbulent Free Jet at Low Mach Number). DLR-FB 67-04, January 1967.
18. Förthmann, E. On Turbulent Jet Expansion. Ing.-Archiv, Vol. V, No. 1, 1934, pp. 42 - 54.
19. Gauntner, J., J. Livingood and P. Hrycak. Survey of Literature on Flow Characteristics of a Single Turbulent Jet Impinging on a Flat Plate, NASA TN D - 5652, Feb. 1970.
20. Gelb, G. and W. Martin. An Experimental Investigation of the Flow Field About a Subsonic Jet Exhausting Into a Quiescent and a Low Velocity Air Stream. Canadian Aeronautical and Space Journal. October 1966, pp. 333 - 342.
21. Glauert, M. The Wall Jet. J. Fluid. Mech. Vol. 1, 1956, pp. 625 - 643.

22. Goldstein, S. A Note on the Measurement of Total Head and Static Pressure in a Turbulent Stream. Proceedings of the Royal Society of London. Vol. CLV, 1936, pp. 570 - 575.
23. Hall, G. Scaling of VTOL Recirculation Effects. NASA CR-1625, August 1970.
24. Hall, G. and K. Rogers. Recirculation Effects Produced by a Pair of Heated Jets Impinging on a Ground Plane. NASA CR-1307, May 1969.
25. Hertel, H. Wall Flows and Ascending Flows from the Redirection of Free Jet Groups. Progress Report. VDI-Zeitschrift, Series. Vol. 12, No. 11, July 1966.
26. Higgins, C. and T. Wainwright. Dynamic Pressure and Thrust Characteristics of Cold Jets Discharging from Several Exhaust Nozzles Designed for VTOL Downwash Suppression. NASA TN-2263, 1964.
27. Higgins, C., D. Kelly and T. Wainwright. Exhaust Jet Wake and Thrust Characteristics of Several Nozzles Designed for VTOL Downwash Suppression. NASA CR-373, 1966.
28. Hinze, J. and B. V.D. Hegge Zijnen. Transfer of Heat and Matter in the Turbulent Mixing Zone of an Axially Symmetrical Jet. Appl. Sci. Res. Series A, Vol. 1, 1949, pp. 435 - 461.
29. Hölscher, F. Theoretische Untersuchungen über den Einfluss der Gastemperatur auf Rezirkulationsströmungen, Dipl.-Arbeit im Inst.f. Strahltriebwerke der TU Braunschweig (Theoretical Studies on the Effect of the Gas Temperature on Recirculation Flow. Diploma Work in the Institute for Jet Engines of the Braunschweig Technical University). Nov. 1968.
30. Hölscher, F. and E. Jünke. Systematische Untersuchungen von Freistrahlen, Bodenstrahlen und Heissgas-Fontänen bei VTOL-Konfigurationen mit Strahltriebwerken, Lift-Fans und Luftschrauben (Systematic Studies of Free Jets, Ground Jets, and Hot Gas Fountains in VTOL Configurations with Jet Engines, Lift Fans, and Propellers). Dornier ZTL Final Report. Vol. 4, Dec. 1969, VT 483 B5.
31. Hrycak, P., D. Lee, J. Gauntner and N. Livingood. Experimental Flow Characteristics of a Single Turbulent Jet Impinging on a Flat Plate. NASA TN-D 5690, March 1970.

32. Hueber, J. Ähnlichkeitsbedingungen für Warmluftrezirkulationsvorgänge bei VTOL-Flugzeugen (Similarity Conditions for Warm Air Recirculation Processes at VTOL Aircraft). Dornier-Werke Report No. 64/3.
33. Jordinson, R. Flow in a Jet Directed Normal to the Wind. British Aeronautical and Research Council, R.+M. No. 3047, 1958.
34. Keffer, J. and W. Baines. The Round Turbulent Jet in a Cross-Wind. Journal Fluid Mech. Vol. 15, 1963, pp. 481 - 496.
35. Laurence, J. Intensity, Scale and Spectra of Turbulence in Mixing Region of Free Subsonic Jet. NACA Report 1292, 1956.
36. Lavi, R., G. Hall and W. Stark. Full-Scale Ground Proximity Investigation of a VTOL Fighter Model Aircraft NASA-CR-1098, June 1968.
37. McLemore, H. and C. Smith. Hot-Gas Ingestion Investigation of Large-Scale Jet VTOL-Fighter-Type Models, NASA-TN-D-4609, June 1968.
38. Liem, K. Flow Processes at a Free Lifting Jet. Luftfahrt-technik Vol. 8, 1962, pp. 198 - 207.
39. Lutz, O. and F. Wolf. I-S Tafel für Luft und Verbrennungsgase (I-S Table for Air and Combustion Gases). Springer-Verlag 1959.
40. Miller, D. and E. Comings. Static Pressure Distribution in the Free Turbulent Jet. Journal of Fluid Mechanics. Vol. 3, 1957, pp. 1 - 16.
41. Morgason, R. and J. Keffer u.a. Analysis of a Jet in a Subsonic Cross-Wind. NASA SP-218, September 1969.
42. Morton, B. Buoyant Plumes in a Moist Atmosphere. Journal of Fluid Mechanics, Vol. 2, Part 1, 1957, pp. 127 - 144.
43. Morton, B. Forced Plumes. Journal of Fluid Mechanics. Vol. 5, Part 1, 1959, pp. 151 - 163.
44. Morton, B., G. Taylor and J. Turner. Turbulent Gravitational Convection from Maintained and Instantaneous Sources. Proc. Roy. Soc. London. Vol. 234, A, 1956, pp. 1 - 23.

45. Murgai, M. and H. Emmons. Natural Convection Above Fires. Journal of Fluid Mechanics. Vol. 8, Part 1, 1960, pp. 611 - 624.
46. Prandtl, L. On the Developed Turbulence. Z.A.M.M., Vol. 5, 1925, pp. 136 - 139.
47. Priestley, C. and F. Ball. Continuous Convection from an Isolated Source of Heat. Quarterly Journal of the Royal Meteorological Society. Vol. 81, 1955, pp. 144 - 157.
48. Rankine, A. Experimental Studies in Thermal Convection. Proc. Phys. Soc. B. Vol. 63, Part 4, 1950, pp. 225 - 243, No. 364 B.
49. Rauch, H. On Making Smoke Stacks too High. Beitr. z. Phys. d. Atm. Vol. 37, No. 2, 1964, pp. 132 - 158.
50. Reichardt, H. Momentum and Heat Exchange in Free Turbulence. Z.A.M.M. Vol. 24, 1944.
51. Reichardt, H. Gesetzmässigkeiten der freien Turbulenz (Regularities of Free Turbulence). VDI-Research paper 414, Second Edition Berlin 1951.
52. Richarz, O., H. Heidrich and V. Zeidler. Voruntersuchungen und Durchführung von rollenden Senkrechtstarts und -landungen mit der VJ 101 C-X2 mit gezündeten Nachbrennern (Preliminary Studies and Performance of Rolling Vertical Takeoffs and Landings with the VJ 101 C-X2 with Afterburners on). BMVg-FBWT 71-13, December 1970.
53. Roscher, H.J. Untersuchung an statischen Drucksoden für hohe Unterschallgeschwindigkeiten (Investigation of Static Pressure Probes for High Subsonic Velocities). DLR-Report 69-14, June 1969.
54. Rouse, H., W. Baines and H. Humphreys. Free Convection over Parallel Sources of Heat. Proc. Phys. Soc. Vol. 66, B, 1953, pp. 393 - 399.
55. Schlichting, H. On the Wind Shadow Problem. Ing.-Archiv, Vol. 1, 1930, pp. 533 - 571.
56. Schlichting, H. Grenzschicht-Theorie (Boundary Layer Theory). Braun-Verlag, Karlsruhe 1965.
57. Schmidt, W. Turbulent Expansion of a Stream of Heated Air, Parts I and II. Z.A.M.M. Vol. 21, 1941, pp. 265 - 278, 351 - 363.

58. Schrader, H. Trocknung feuchter Oberflächen mittels Warmluftstrahlen (Drying of Moist Surfaces by Warm Air Jets). VDI-Research paper 484, 1961.
59. Schulz, G. Berechnung der Druckverteilung auf einem Flugzeugrumpf mit austretenden Hubstrahlen mittels Singularitäten (Calculation of the Pressure Distribution on an Aircraft Fuselage with Lifting Jets Working by Means of Singularities). DLR-Report 70-28, April 1971.
60. Schwantes, E. Theoretische Untersuchung des Betriebsverhaltens eines Hubtriebwerks unter Berücksichtigung der Rezirkulation, Diplomarbeit im Institut für Strahltriebwerke der TU Braunschweig (Theoretical Study of the Operating Behavior of a Lift Engine, Considering Recirculation. Diploma Work in the Institute for Jet Engines of the Braunschweig Technical University). November 1966.
61. Schwantes, E. Übersicht über den Bodeneffekt bei strahlgestützten V/STOL-Flugzeugen Literaturbericht (Review of the Ground Effect on Jet-supported V/STOL Aircraft Literature Report). DLR-Report 68-28, December 1968.
62. Schwantes, E. Untersuchungen an Abgasstrahlen von TL-Triebwerksmodellen (Investigations of Exhaust Gas Jets of TL Engine Models). DLR-Report 70-28, April 1971.
63. Schwantes, E. Der Heissgaswandstrahl bei kritischem Düsen-druckverhältnis, Vortrag vor dem DGLR-Fachausschuss für "Luftatmende Antriebe" (The Hot Gas Wall Jet at Critical Nozzle Pressure Ratio. Lecture Before the DGLR Expert Committee for "Air-Breathing Engines"). Bremen, Feb. 3, 1971.
64. Schwantes, E. The Propulsion Jet of a VTOL Aircraft. AGARD -CP 91-71, Sept. 1971.
65. Seibold, W. Über die von Hubstrahlen an Senkrechtstartern erzeugten Sekundärkräfte (On the Secondary Forces Generated on Vertical Takeoff Aircraft by Lifting Jets). WGLR Yearbook 1962, pp. 257 - 275.
66. Seifferth, K. Experimentelle Untersuchungen zur Ausbreitung eines Wandstrahls bei einer Einzeldüse (Experimental Investigations on the Expansion of a Wall Jet with a Single Nozzle). Messerschmitt Bölkow-Blohm UFE-Report No. 443-69 November 1969.
67. Shapiro, A. The Dynamics and Thermodynamics of Compressible Fluid Flow. The Ronald Press Company, New York, Vol. 1, 1953.

68. Skifstad, J. Aerodynamics of Jets Pertinent to V/STOL Aircraft. Journal of Aircraft. Vol. 7, No. 3, May-June 1970.
69. Speth, R. and P. Ryan. A Generalized Experimental Study of Inlet Temperature Rise and Near Field Temperature Contours of Jet V/STOL Aircraft in Ground Proximity AIAA Paper No. 66-740, September 1966.
70. Sutton, O.G. Convection in the Atmosphere Near the Ground. Quart. Journal Roy. Met. Soc. Vol. 74, 1948.
71. Sutton, O.G. Micrometeorology. New York 1953, McGraw-Hill Book Company, Inc.
72. Tani, I. and Y. Komatsu. Impingement of a Round Jet on a Flat Surface. Appl. Mech. Proc. of the 11th. International Congress of Appl. Mech. München 1964, Springer-Verlag 1966.
73. Taylor, G. The Transport of Vorticity and Heat Through Fluids in Turbulent Motion. Proc. Roy. Soc. London, Series A, 135, 1932, pp. 685 - 705.
74. Tollmien, W. Calculation of Turbulent Expansion Processes. Z. angew. Math. Mech. Vol. 6, 1926, pp. 468 - 478.
75. Wagner, F. On the Sound and Flow Field of an Axially Symmetric Free Jet Striking a Wall. Z. Flugwiss. Vol. 19, 1971, pp. 30 - 44.
76. Wille, R. Contributions to the Phenomenology of Free Jets. Z. Flugwiss. Vol. 11, No. 6, 1963.
77. Wippermann, F. Possibilities for Theoretical Understanding of the Expansion Process. Zeitschr. Staub, Vol. 21, 1961, pp. 104 - 109.
78. Wuest, W. Strömungsmesstechnik (Flow Measurement Technology). Vieweg-Verlag 1969.

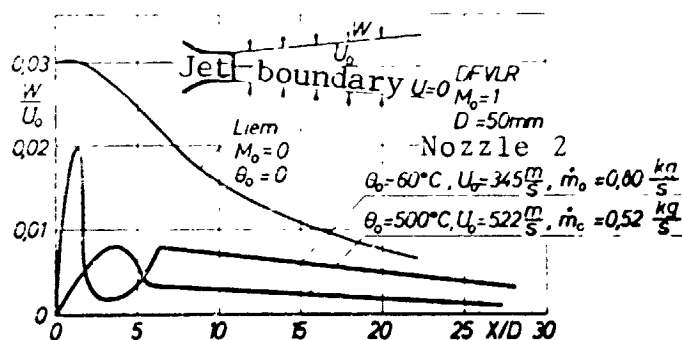


Figure 9. Inflow velocity of the free jet. Temperature and Mach number influence.

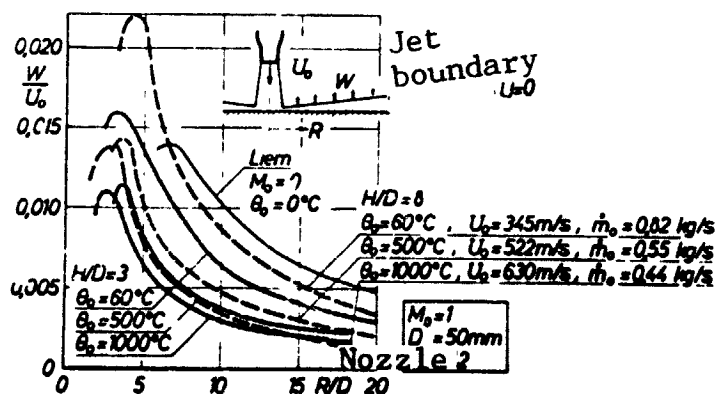


Figure 10. Inflow velocities of the wall jet. Temperature and H/D influence.

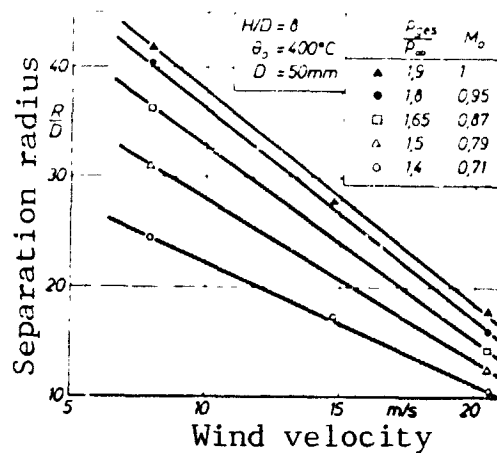


Figure 11. Separation radius of the wall jet, Mach number effect.

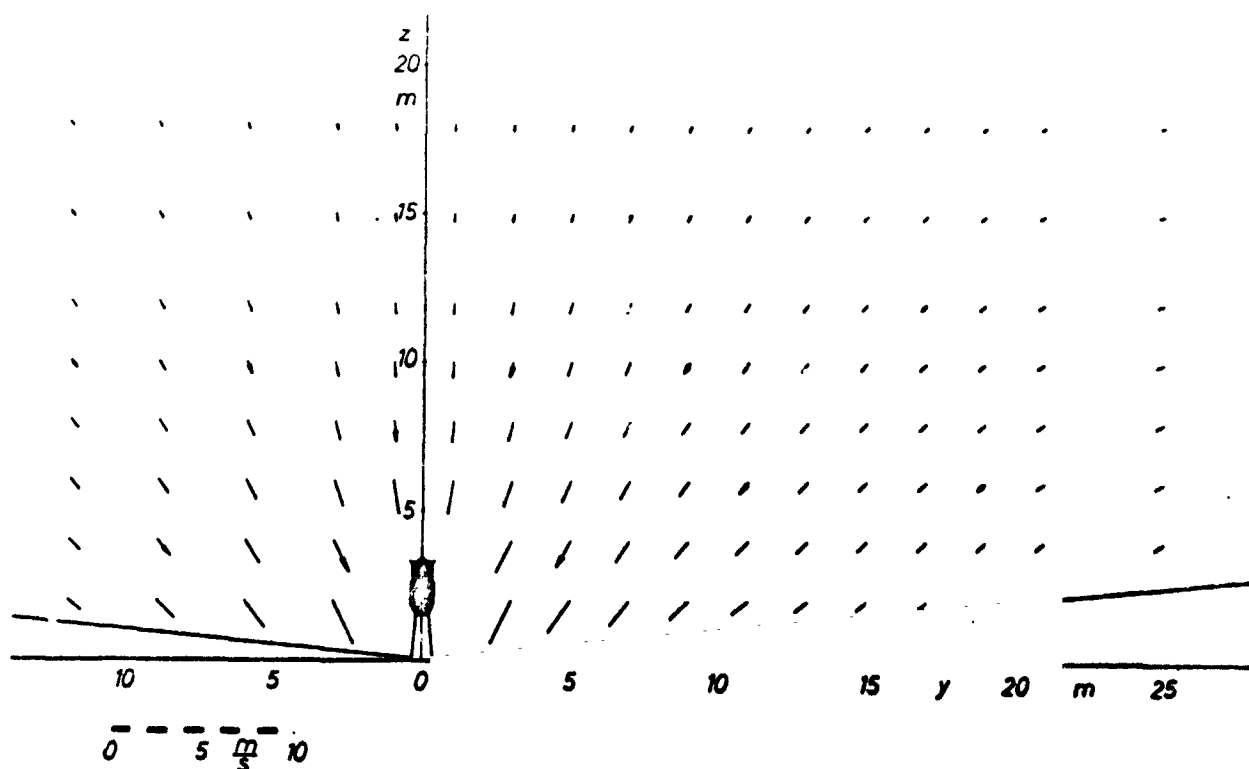


Figure 12. Calculated velocities in the y-z plane of the secondary flow field of the RB 162-31 lift engine, without wind.
 $M_0 = 1$, $H/D = 3$.

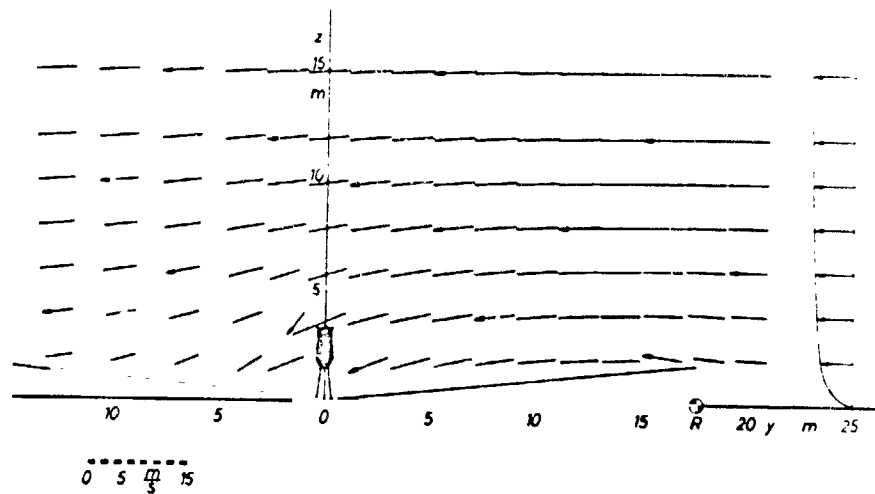


Figure 13. Calculated velocities in the y-z plane of the recirculation flow field of the RB 162-31 lift engine. $M_0 = 1$, $H/D = 3$, $W = 5$ m/s
 • Separation radius of the wall jet.

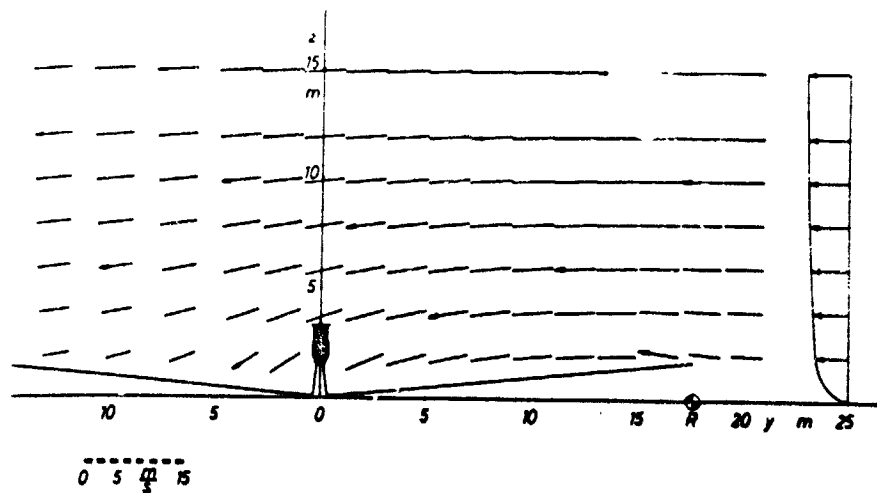


Figure 14. Calculated velocities in the y-z plane of the recirculation flow field of the RB 162-31 lift engine, without intake sink. $M_0 = 1$, $H/D = 3$, $W = 5$ m/s.

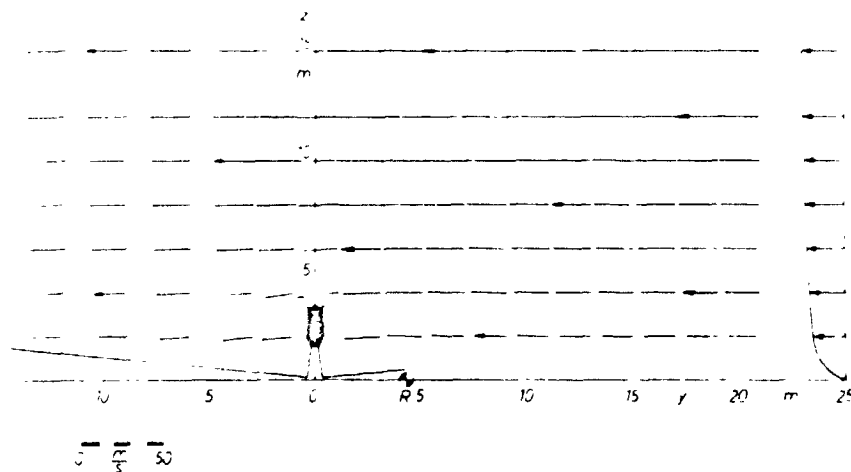


Figure 15. Calculated velocities in the y-z plane of the recirculation flow field of the RB 162-31 lift engine.
 $M_0 = 1$, $H/D = 3$, $W = 20$ m/s.

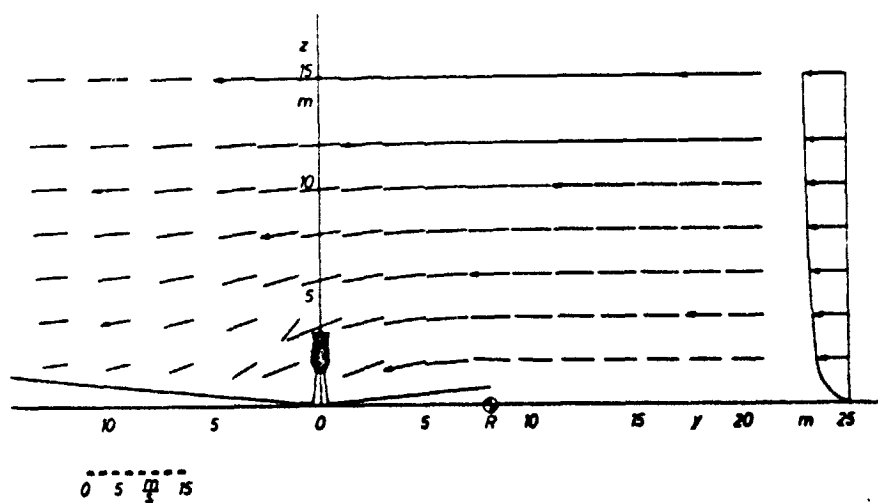


Figure 16. Calculated velocities in the y-z plane of the recirculation flow field of the RB 162-31 lift engine.
 $M_0 = 0.7$, $H/D = 3$, $W = 5$ m/s.

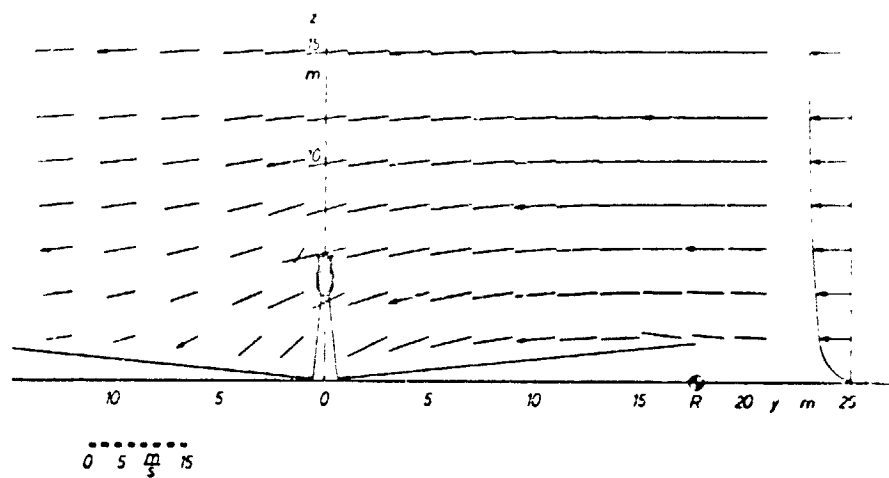


Figure 17. Calculated velocities in the y - z plane of the recirculation flow field of the RB 162-31 lift engine. $M_0 = 1$, $H/D = 8$, $W = 5$ m/s.

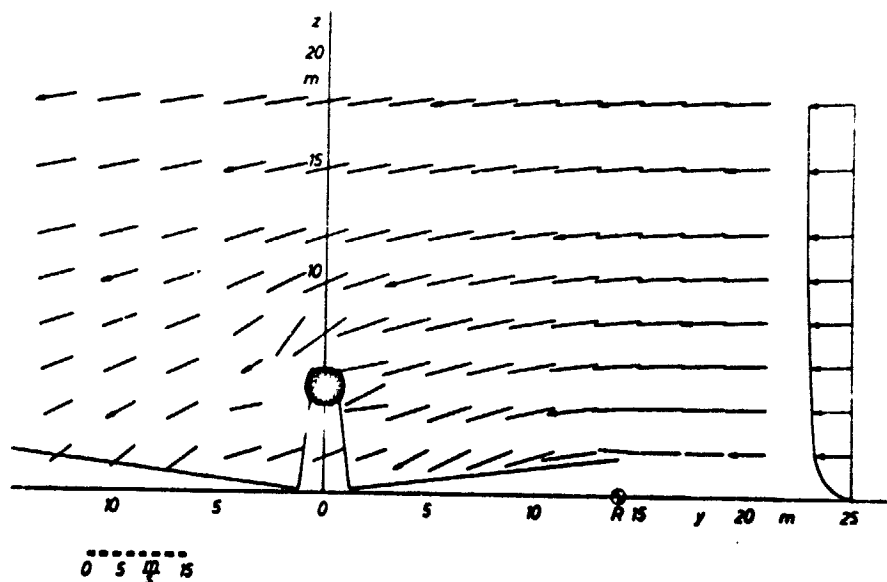


Figure 18. Calculated velocities in the y - z plane of the recirculation flow field of the RB 202 lift engine. $M_0 = 0.55$, $H/D = 3$, $W = 5$ m/s.

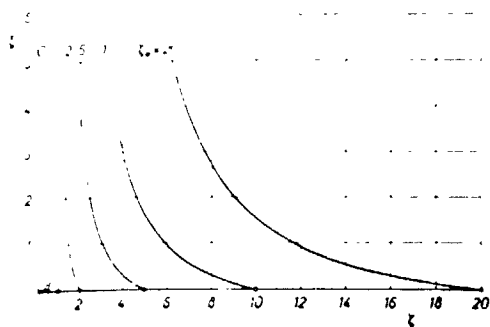


Figure 19. Velocity of a plane ascending flow as a function of the height.

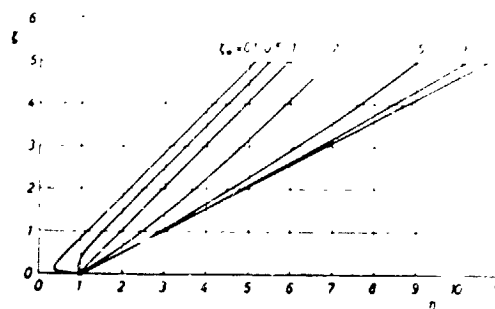


Figure 20. Width of a plane ascending flow as a function of the height.

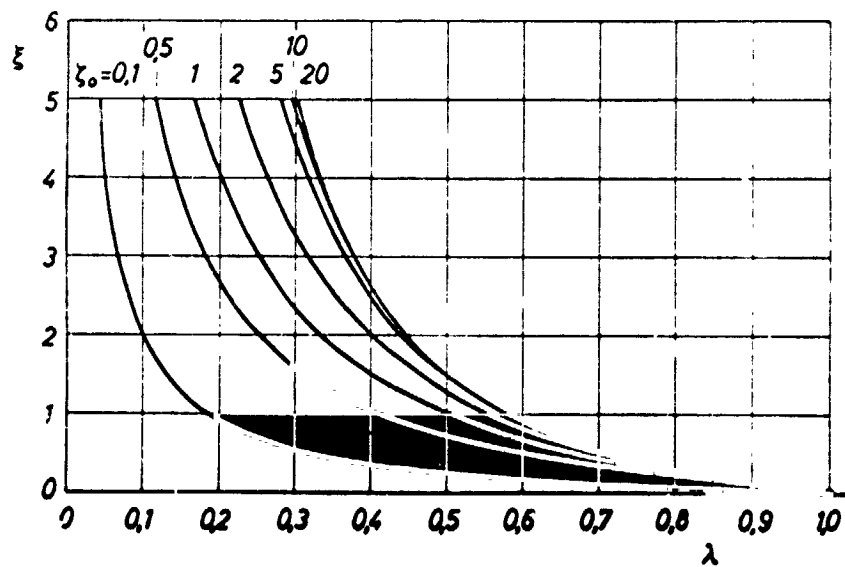


Figure 21. Temperature of a plane ascending flow as a function of the height.



Figure 22. Ground effect test system with Model engine 1.

Figure 23. Model engine 2 during a test run.

/ 72

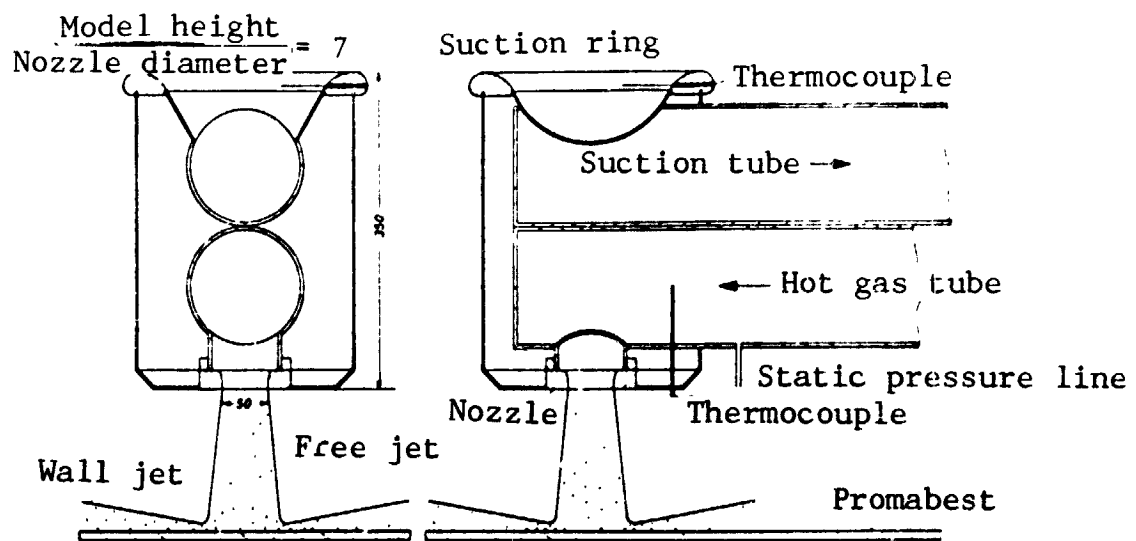


Figure 24. Engine model 1.

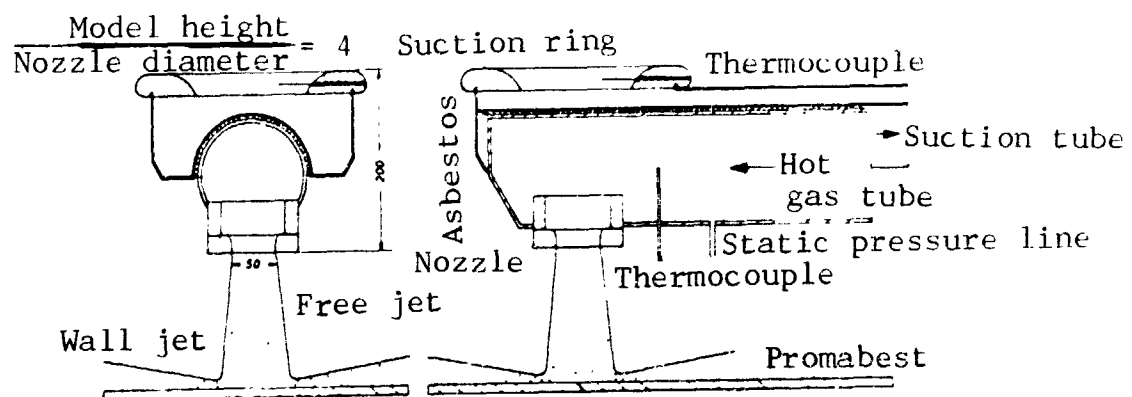


Figure 25. Engine model 2.



Figure 26. Light plane projector to visualize flows.

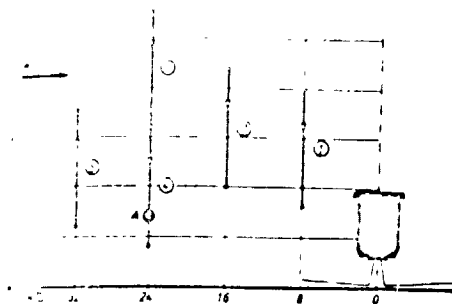


Figure 27. Path of adjustment of the movable velocity and temperature probes in the y-z plane of the recirculation flow field.

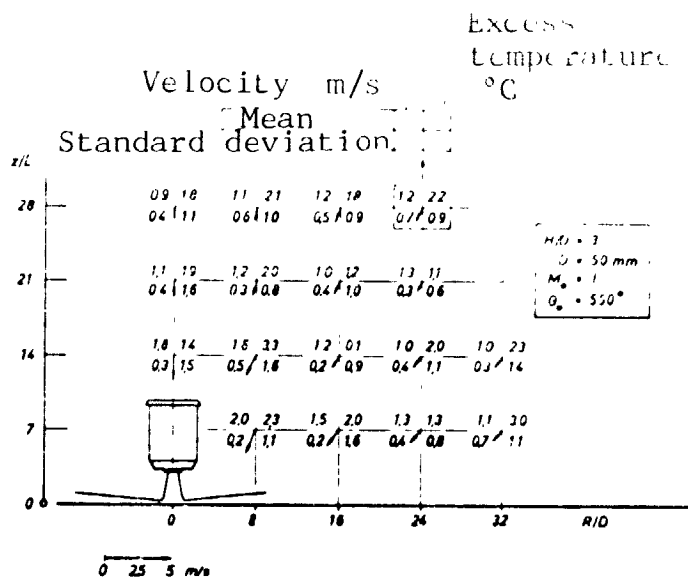


Figure 28. Velocities and excess temperatures of the secondary flow field in the y-z plane, without wind.

Figure 29.

Velocities and excess temperatures measured in the y-z plane of the recirculation flow field.

R^* = separation radius of the wall jet.

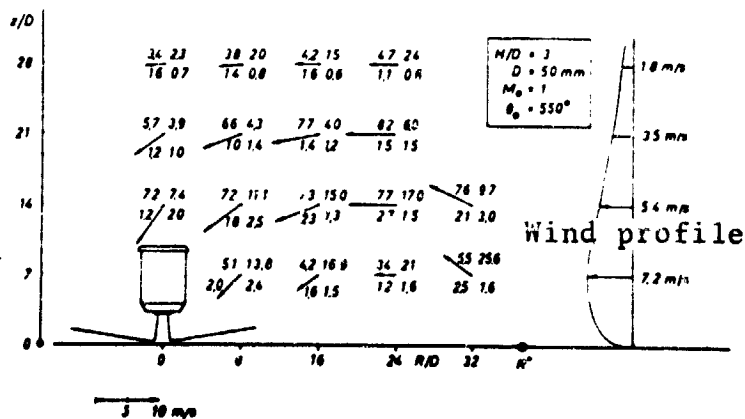
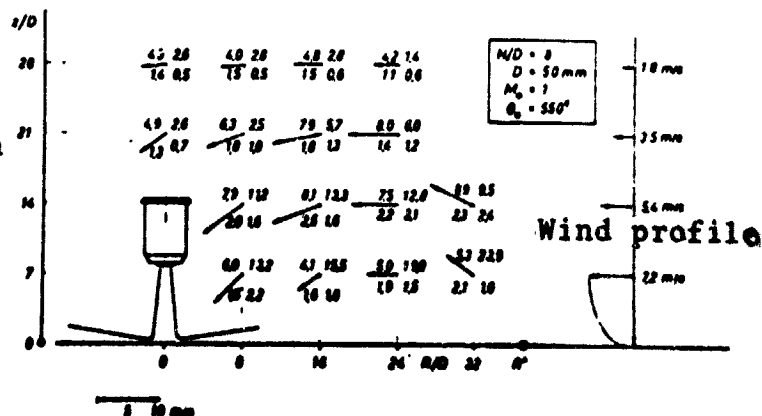


Figure 30.

Velocities and excess temperatures measured in the y-z plane of the recirculation flow field.



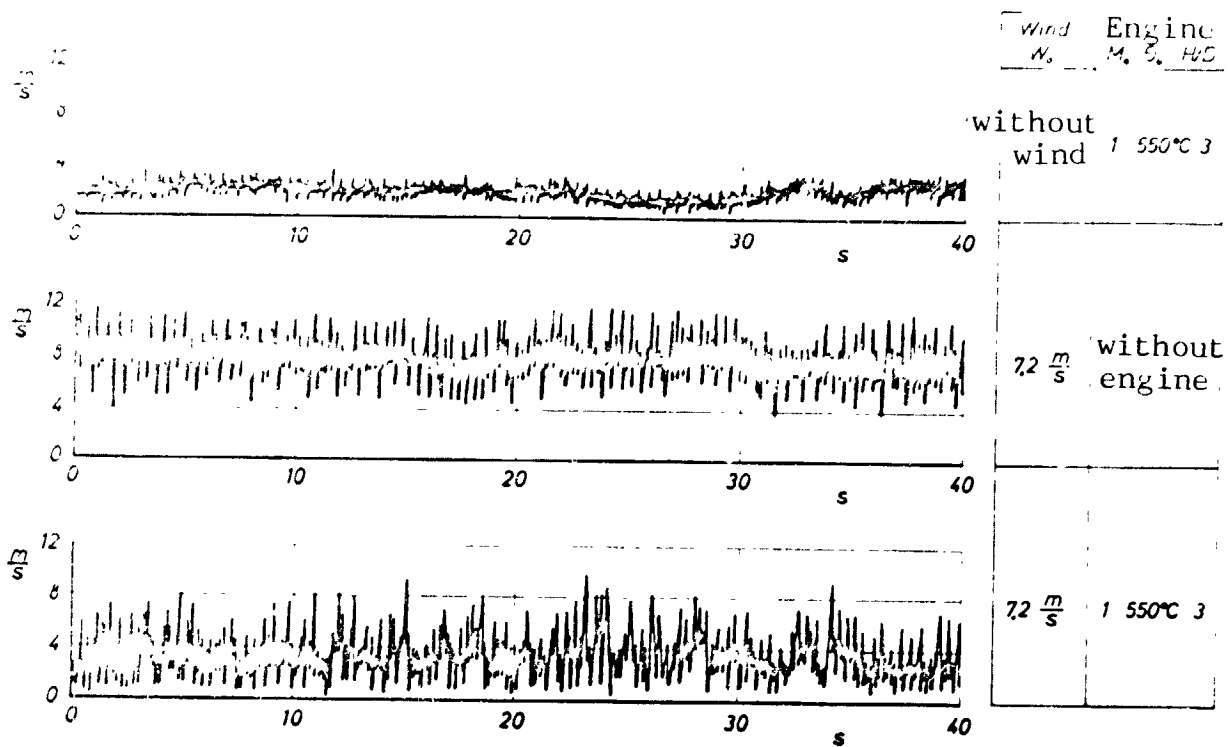


Figure 31. Velocity fluctuations in the recirculation flow field at measuring point A (visible in Figure 27).

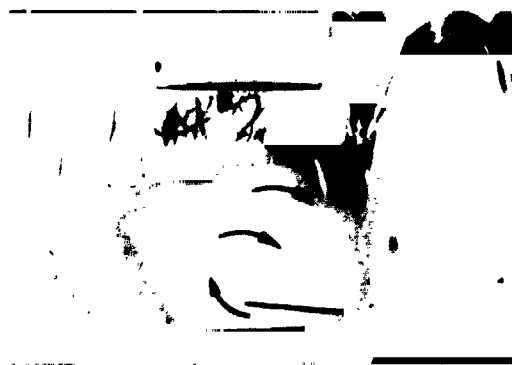


Figure 32. Light section photo of the wall jet separation, made visible by coloring the engine jet.
 $M_o = 1$, $\theta_o = 550^\circ\text{C}$, $W_o = 8 \text{ m/s}$,
 $H/D = 3$.



Figure 33. Light section photo of the wall jet separation, made visible by coloring the wind.
 $M_o = 1$, $\theta_o = 550^\circ\text{C}$, $W_o = 8 \text{ m/s}$,
 $H/D = 3$.

Figure 34.
 Light section photo of the recirculation flow field, configuration of Figure 33.



/ 75

Figure 35.
 Light section photo of the recirculation flow field, configuration of Figure 33.

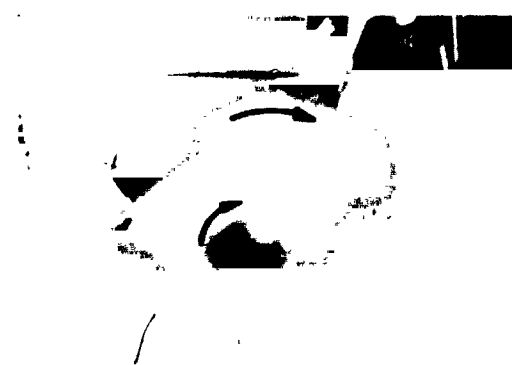


Figure 36.

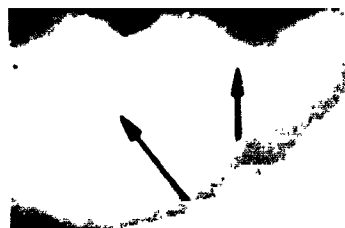
Light section photo of the
recirculation flow field,
configuration of Figure 33.



Figure 37.

Horizontal light section
through the wall jet, 50 mm
above the plate surface.

$M_0 = 1$, $\theta_0 = 50^\circ\text{C}$, $W_0 = 14 \text{ m/s}$,
 $H/D = 3$.



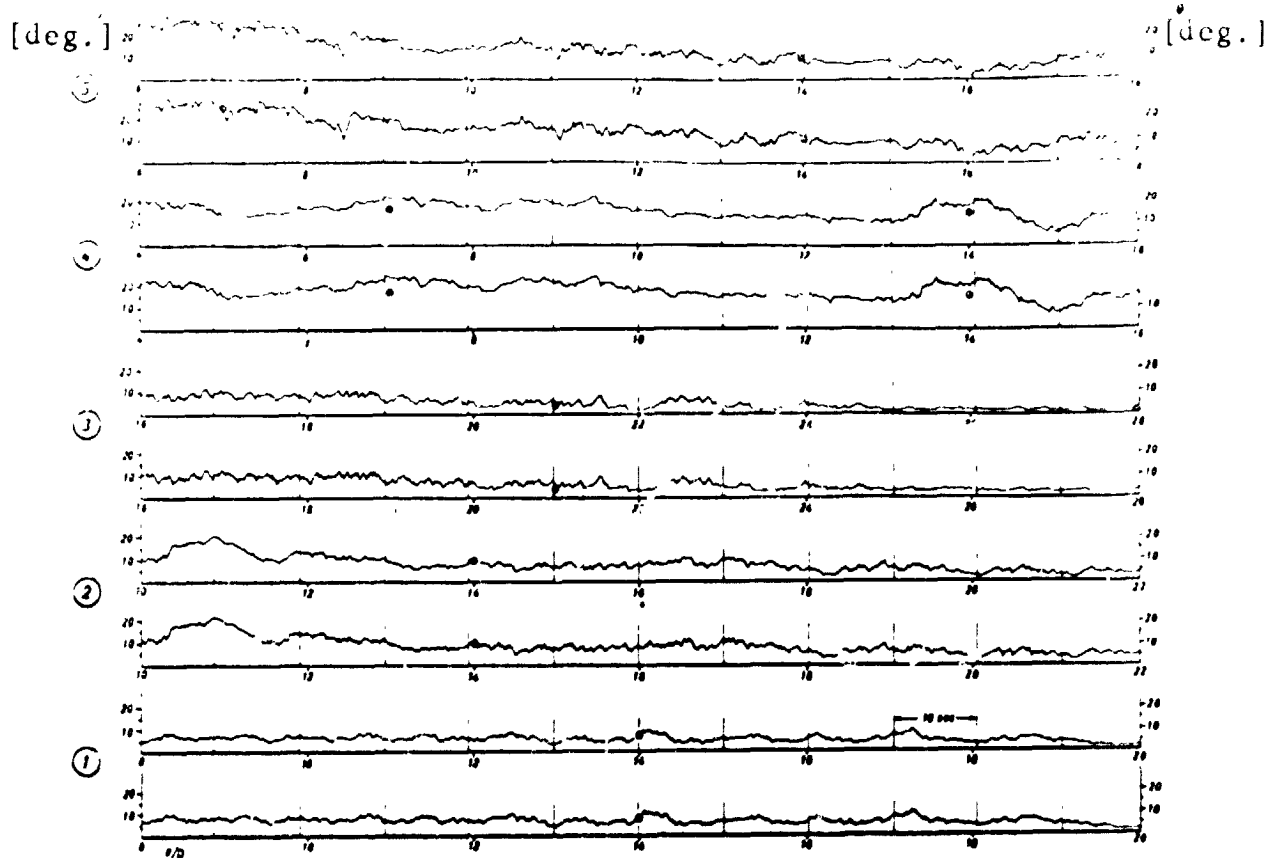


Figure 38.

Temperature measurement in the recirculation flow field, measured from two thermocouples 1 mm apart (0.5 mm diameter). Upper half of the figure: $H/D = 3$; Lower half, $H/D = 8$. Coordinates can be seen from Figure 27. ● : independently measured mean of 40 individual measurements.

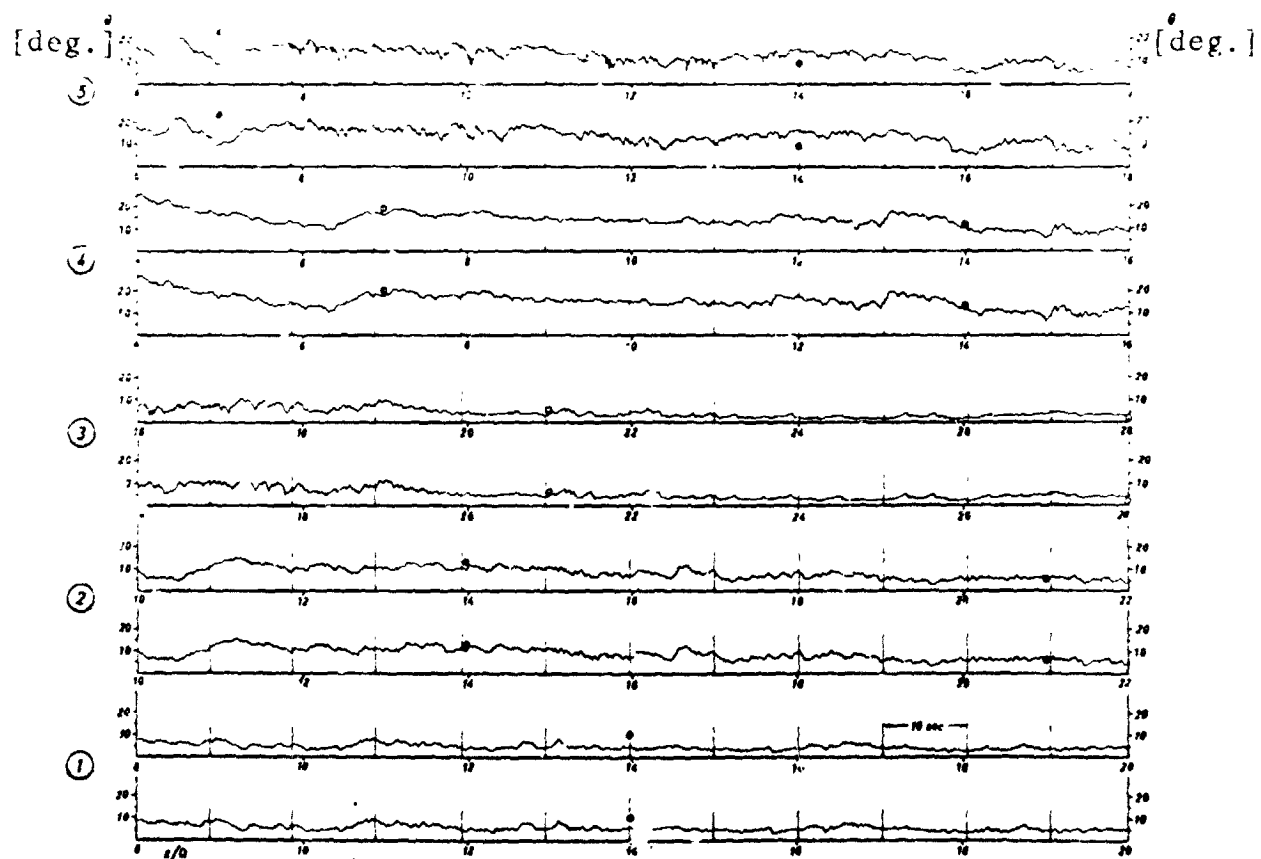


Figure 38. (Continued)

Figure 39.

Distribution of the excess temperatures in the recirculation flow field, $H/D = 3$. Shaded area: range of variation of the measurements.

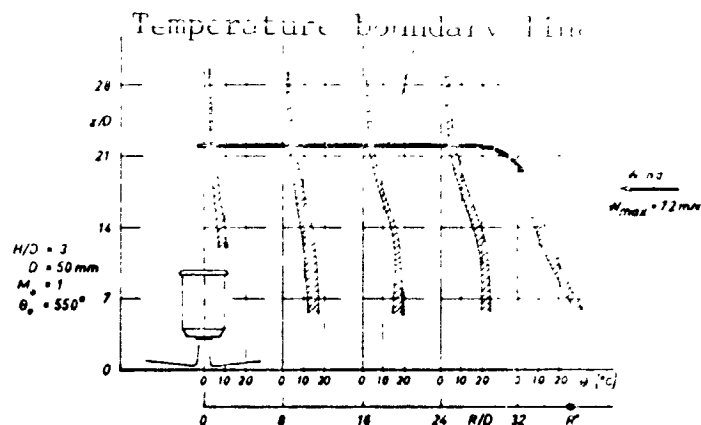


Figure 40.

Distribution of the excess temperatures in the recirculation flow field, $H/D = 8$. Shaded area: range of variation of the measurements.

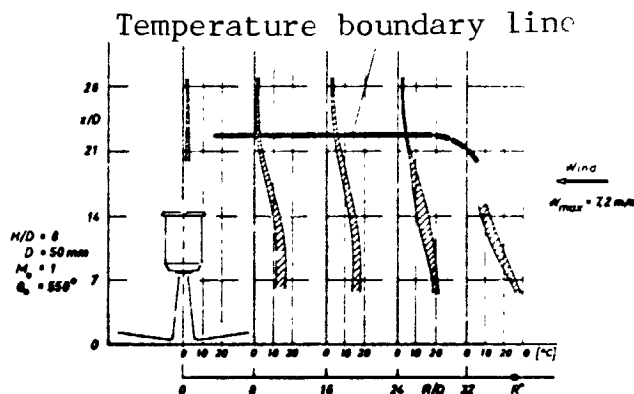
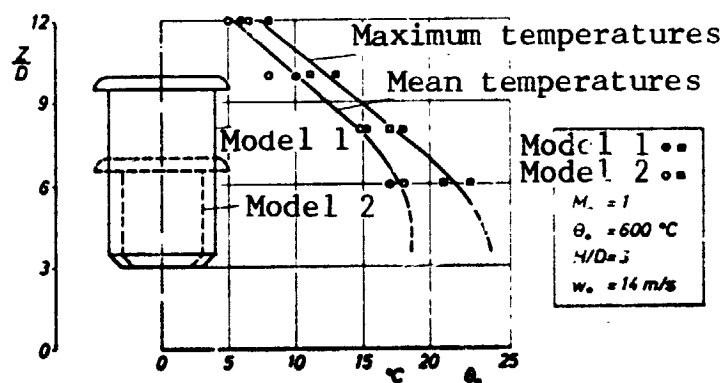


Figure 41.

Measured temperature profile of the recirculation flow on the engine center axis.



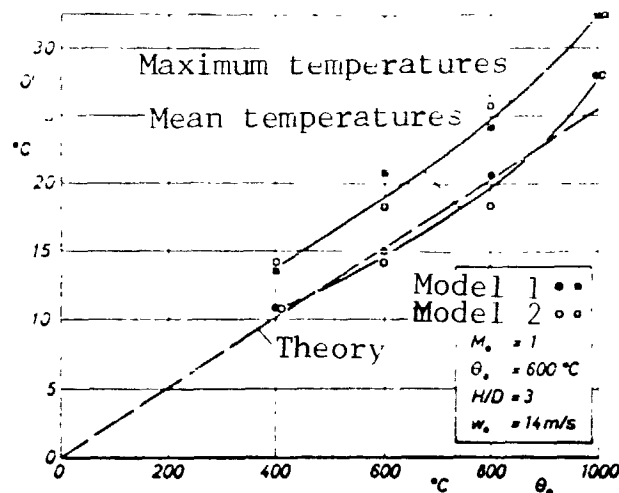


Figure 42. Calculated and measured temperature rise at the compressor intake as a function of the exhaust gas jet temperature.

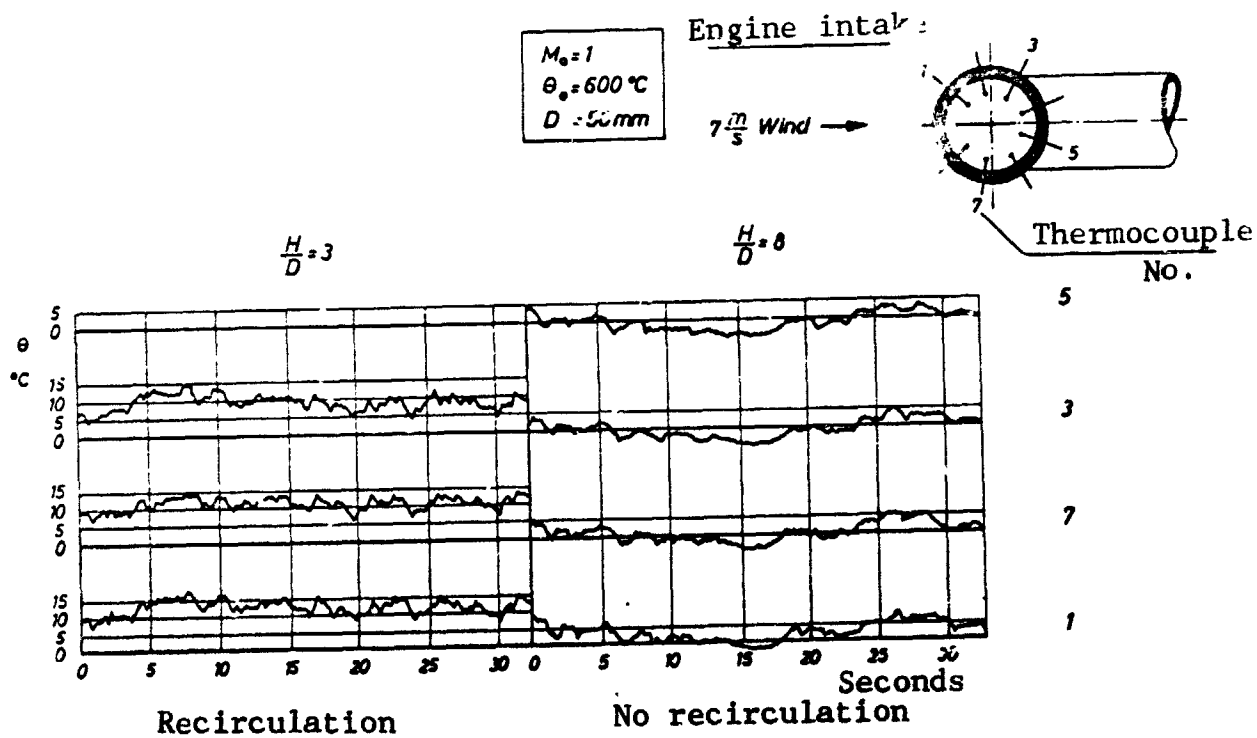


Figure 43. Temperature fluctuations at the engine intake.

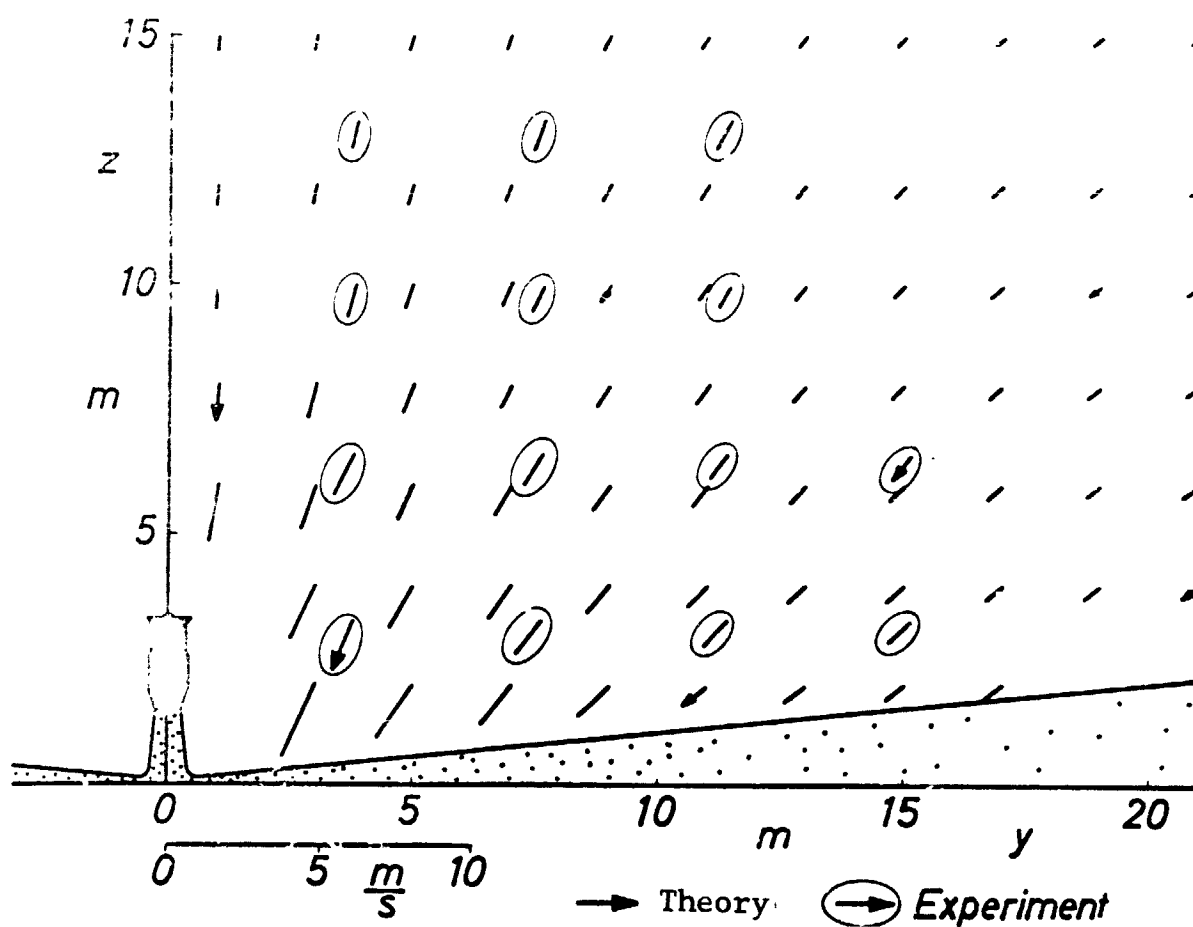
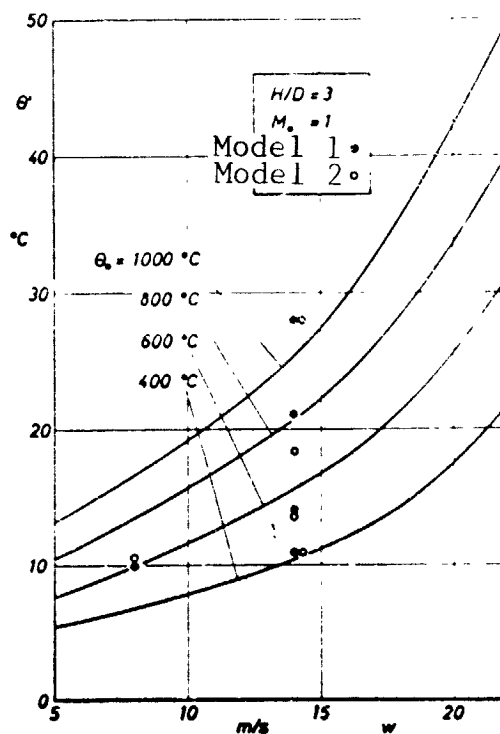


Figure 44. Calculated and measured velocities in the y - z plane of a lift engine (superimposition of Figure 12 and Figure 28).

Figure 45.

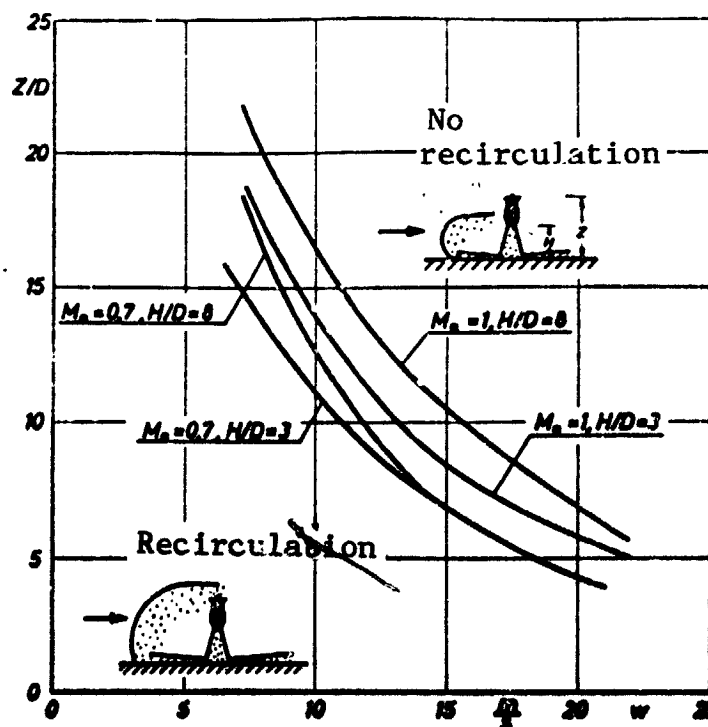
Calculated and measured temperature rises at the compressor intake



/ 80

Figure 46.

Height of the temperature boundary line on the engine central axis.



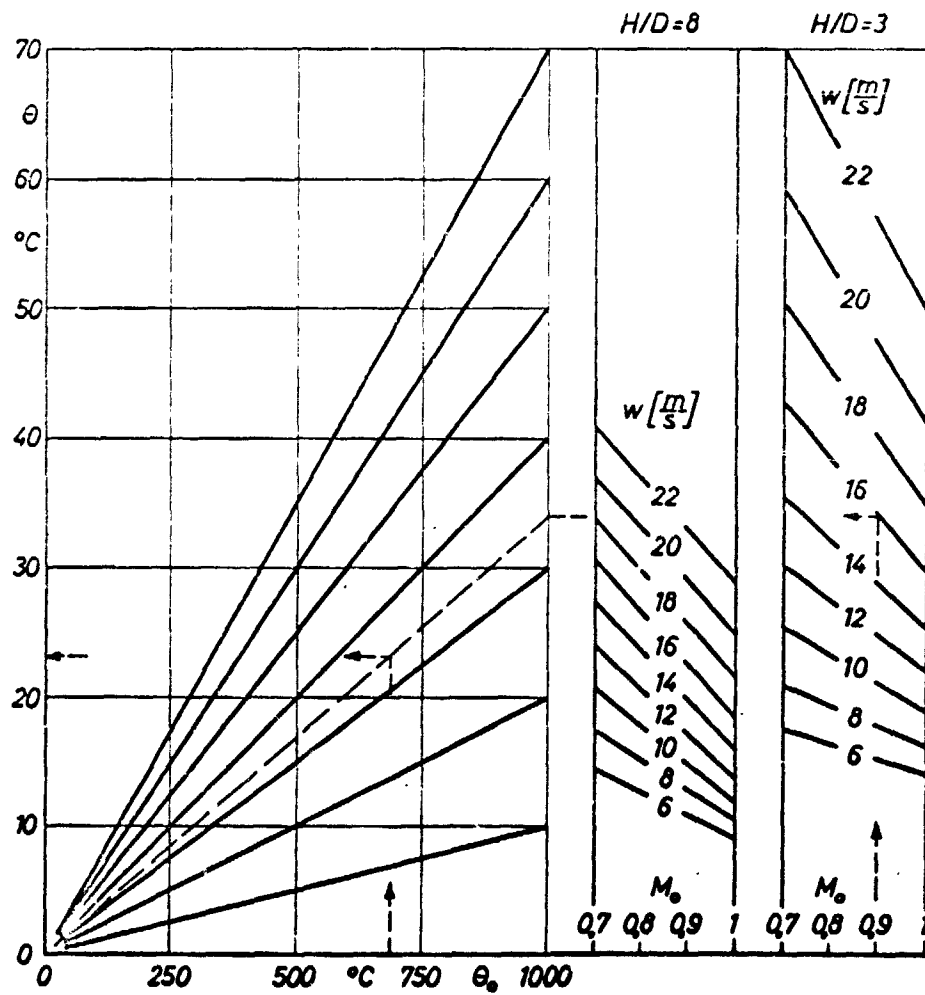


Figure 47. Temperature rise at the engine intake due to wind recirculation as a function of M_o , w , θ_o , H/D .

APPENDIX

9. Appendix

9.1 Engine process

Special abbreviations in Section 9.1

a	Speed of sound
b^*	Specific fuel consumption
c_p	Molecular heat
F	Thrust
H_u	Lower heating value
i	Specific enthalpy
I	Molar enthalpy
L	Molar amount of air
M	Molecular weight
O	Molar oxygen requirement
P	Power
p	Pressure
r	Volume proportion
S	Molar entropy
β	Correction factor for the IS table
η	Efficiency
λ	Air excess coefficient
ξ	Mass proportion
σ	Mollier number

Indices

2,3,4,9	States in the IS diagram
2', 3', 4', 9'	Isentropic states in the IS diagram
ad	Adiabatic
B	Fuel
BK	Combustion chamber
D	Nozzle
L	Air
mech	Mechanical
Str	Jet

T Turbine
th Thermal
V Compressor

/ 2

Calculation of the thrust loss of the RB 162 life engine with temperature rise at the intake

Here, with the Rolls-Royce RB 162-31 lift engine as an example, we shall show how sensitive jet engines are to a change in the intake air temperature (Figure 1). This engine, which is one of the second generation lift engines, has a 6-stage axial compressor. The first stage is of aluminum and all the other rotor and stator buckets are of glass-fiber-reinforced plastic. A titanium wheel with uncooled blades is used as the single-stage turbine. By means of this extremely light construction, the engine attains the outstanding thrust-weight ratio of 16:1.

The calculation of the engine process is based on the following data:

Compressor air throughput	\dot{m}_L	=	40 kg/s
Compressor pressure ratio	P_3/P_2	=	4.25
Turbine intake temperature	T_4	=	978°C
Thrust with $T_\infty = 15^\circ\text{C}$	F	=	24,500 N
Fuel	JP4 ($H_u = 42,700 \text{ kJ/kg}$)		

As no data can be found about the efficiency, it must be estimated or calculated. We estimate that

Combustion chamber efficiency	η_{BK}	=	0.965
Mechanical efficiency	η_{mech}	=	0.99

The remaining efficiencies can be calculated iteratively through the engine process, with the cyclic process calculated through until the two independent determining equations (Equation 9.28 and Equation 9.30) give the same result. This method leads to the following efficiencies:

Compressor efficiency	η_c	=	0.84
Turbine efficiency	η_T	=	0.84
Nozzle efficiency	η_D	=	0.935

These relatively poor efficiencies are interesting. They are caused by the extreme light construction and the short length of the lift engine.

The calculation of the engine process is done from the IS table of Lutz-Wolf [39] (Figure 48).

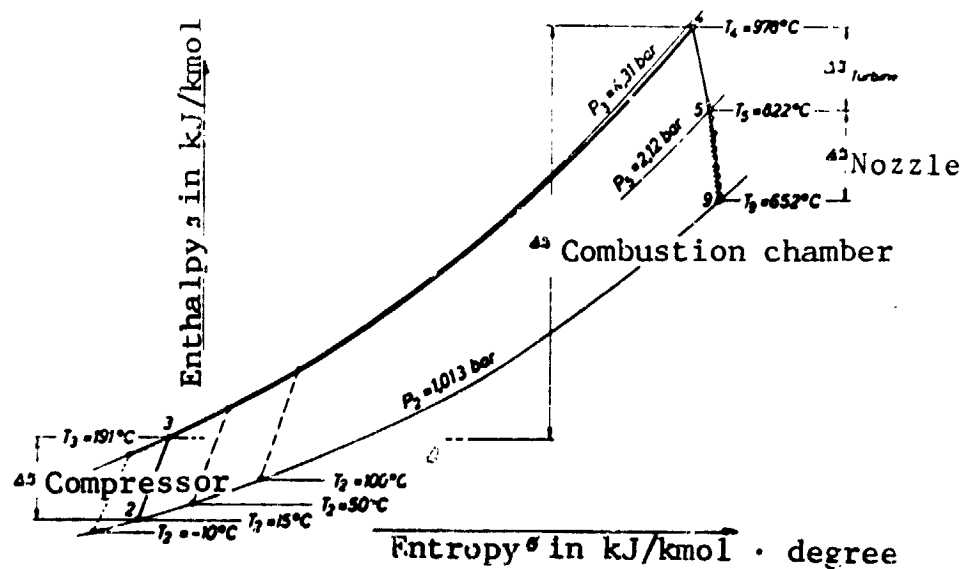


Figure 48. Engine process of the RB 162-31 in the IS diagram according to Lutz-Wolf.

Point 2 of the IS diagram is determined by the ICAO standard atmosphere. The volume flow through the compressor is considered constant here for various intake temperatures:

/83

$$\dot{V} = \frac{\dot{m}_v}{\rho} = \text{constant.} \quad (9.1)$$

Final compressor pressure:

$$p_3 = p_2 \cdot \frac{p_3}{p_2}. \quad (9.2)$$

Isentropic compression temperature:

$$T_{3'} = T_2 \left(\frac{p_3}{p_2} \right)^{\frac{\kappa-1}{\kappa}}. \quad (9.3)$$

Final compressor temperature:

$$T_3 = \frac{T_{3'} - T_2}{\eta_v} + T_2. \quad (9.4)$$

Compressor efficiency:

$$\eta_v = \frac{i_{3'} - i_2}{i_3 - i_2}. \quad (9.5)$$

Enthalpy difference in the combustion chamber:

/ 84

$$\Delta i_{BK} = c_{PBK} \cdot (T_4 - T_3) \quad (9.6)$$

$$= \eta_{BK} \cdot H_u \cdot \frac{\dot{m}_B}{\dot{m}_L + \dot{m}_B}. \quad (9.7)$$

\dot{m}_B is the fuel consumption.

The specific fuel consumption is

$$b^* = \frac{\dot{m}_B}{F}. \quad (9.8)$$

Air requirement and molecular weight of the exhaust gas:

The fuel, JP4, is composed of the following percentages by weight:

c	Carbon	-	85.4%
h	Hydrogen	=	14.4%
s	Sulfur	=	0.15%
o	Oxygen	=	0.03%
			<hr/>
			99.98%

According to Baehr [2], the oxygen required for complete combustion is

$$o_{\min} = 2.664 \cdot c + 7.937 \cdot h + 0.998 \cdot s - c = 3.41 \left[\frac{\text{kg } O_2}{\text{kg fuel}} \right] \quad (9.9)$$

The air requirement is

$$L_{\min} = \frac{o_{\min}}{\xi_{O_2}} = 14.7 \left[\frac{\text{kg } O_2}{\text{kg fuel}} \right] \quad (9.10)$$

in which $\xi_{O_2} = 0.232$ is the mass proportion of oxygen in air.

m_B [kg] fuel required for combustion with $m_B \cdot L_{\min}$ [kg] air.
Air excess coefficient:

$$\lambda = \frac{\text{amount of air actually passed through}}{\text{amount of air needed for stoichiometric combustion}} =$$

$$\lambda = \frac{m_L}{m_L \cdot L_{\min}} = 3.6 \quad (9.11)$$

Mollier number:

/85

$$\sigma = 1 + 3 \frac{h - (\frac{O-s}{8})}{c} = 1.51 \quad (9.12)$$

Volume proportion of fuel:

$$r_{CO_2} = \frac{0.21 \cdot c}{c[\sigma(\lambda - 0.21) + 0.21] + 1.26 \cdot h} = 0.038 \quad (9.13)$$

$$r_{O_2} = r_{CO_2} \cdot (\lambda - 1) \cdot \sigma = 0.149 \quad (9.14)$$

$$r_{N_2} = r_{CO_2} \frac{0.79}{0.21} \lambda \cdot \sigma = 0.775 \quad (9.15)$$

$$r_{H_2O} = r_{CO_2} \frac{6 \cdot h}{c} = 0.038 \quad (9.16)$$

	1.000
Residual air gas	0.0
	1.000

According to Lutz-Wolf [39] the β -value is:

$$\beta = 0.94 \cdot r_{N_2} + 1.23 \cdot r_{O_2} + 2.20 \cdot r_{H_2O} + 4.0 \cdot r_{CO_2} = 1.15. \quad (9.17)$$

Molecular weight of the exhaust gas:

$$M = 28.16 \cdot r_{N_2} + 32.0 \cdot r_{O_2} + 18.02 \cdot r_{H_2O} + 44.01 \cdot r_{CO_2} = 28.925 \left[\frac{kg}{kmol} \right] \quad (9.18)$$

Now the compression process can be expressed by the molar enthalpy:

$$\Delta I_V = \epsilon_{p_m} \cdot (T_3 - T_2) \quad (9.19)$$

in which the mean molecular heat is defined as:

$$\epsilon_{p_m} = c_{p_m} \Big|_{T_2}^{T_3} \cdot M. \quad (9.20)$$

/ 86

The combustion chamber final state is:

$$p_4 = p_3 \cdot \text{combustion chamber pressure loss} \quad (9.21)$$

$$I_4 = \epsilon_{p_4} \cdot T_4. \quad (9.22)$$

The turbine process:

$$\Delta I_T = \frac{v}{\eta_m} \quad (9.23)$$

$$\Delta I_{ad} = \frac{\Delta I_v}{\eta_m \cdot \eta_T} \quad (9.24)$$

so that it can be determined in the IS diagram, point 5.

The nozzle process:

In the nozzle, the exhaust gas expands to the ambient pressure p_2 . The enthalpy difference of the nozzle is read in the IS diagram.

$$\Delta I_D = \Delta I_{ad} \cdot \eta_D \quad (9.25)$$

Thus, point 9 is fixed in the IS diagram.

Nozzle outflow velocity:

$$U_9 = \frac{F}{\dot{m}} = \frac{F}{\dot{m}_L + \dot{m}_D} = \sqrt{2 \cdot \eta_{th} \cdot \Delta I_{ex}} \quad (9.26)$$

Outflow Mach number:

$$M_9 = \frac{U_9}{a_9} \quad (9.27)$$

where a_9 is the sonic velocity in the exhaust gas.

The thermal efficiency, which is defined by the individual efficiencies and the enthalpy differences, is:

$$\eta_{th} = \frac{(I_4 - I_5)\eta_T + (I_5 - I_9)\eta_D - (I_3 - I_2)/\eta_v}{I_4 - I_3} \quad (9.28)$$

It must be equal to the efficiency determined from the ratio of 187
jet power and fuel power:

$$\eta_{th} = \frac{P_{str}}{P_B} \quad (9.29)$$

$$= \frac{(\dot{m}_L + \dot{m}_B) \frac{u_3^2}{2}}{\dot{m}_B \cdot H_u} \quad (9.30)$$

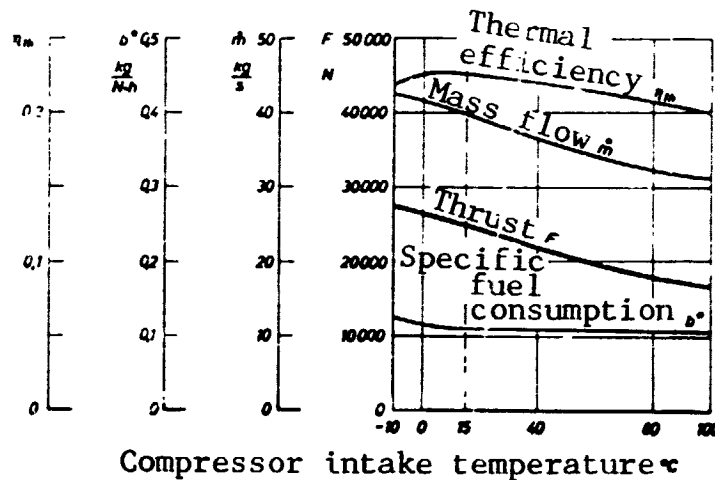


Figure 49. Engine parameters of the RB 162-31 as functions of the compressor intake temperature.

The results of the calculation are plotted in Figures 2 and 49 versus the compressor intake temperature.

9.2 Potential Theory

Special abbreviations in Section 9.2

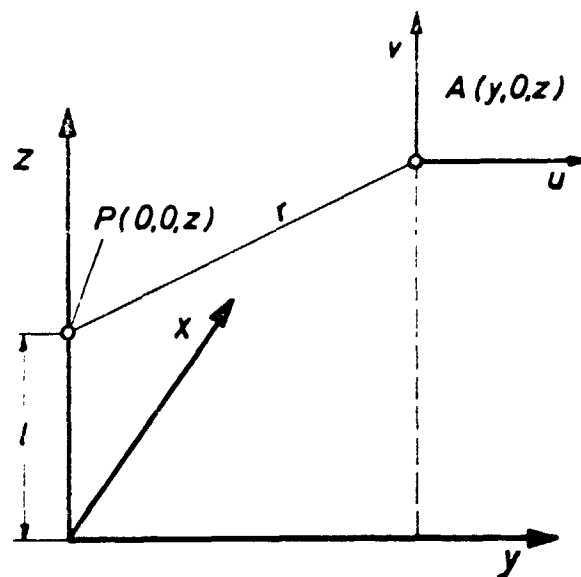
- a Ellipse radius
- A Distance
- B Constant value for the sink distribution
- $h_{1,2}$ Cylinder height in the z direction
- $l_{1,2}$ Lengths on the z axis
- u Velocity component in the positive y direction
- v Velocity component in the positive z direction
- x Horizontal coordinate from the jet impact point outward,
across the wind direction
- y Horizontal coordinate, from the jet impact point outward,
opposite to the wind direction
- z Vertical coordinate, from the jet impact point outward
across the wind direction
- γ Moving coordinate in the z direction
- η Moving coordinate in the x or z direction
- ξ Moving coordinate in the y direction.

In the following, the velocity components u and v in the / 89 y-z plane of the yxz coordinate system are derived from the potential equations 3.2, 3.3 and 3.4.

Point source:

The potential equation of the point source is:

$$\phi = - \frac{1}{4\pi} \cdot \dot{V} \cdot \frac{1}{r} \quad . \quad (3.2)$$



If the source point is at point P on the z axis of the yxz coordinate system:

$$\phi = - \frac{\dot{V}}{4\pi} \cdot \frac{1}{\sqrt{y^2 + (z-l)^2}} \quad (9.31)$$

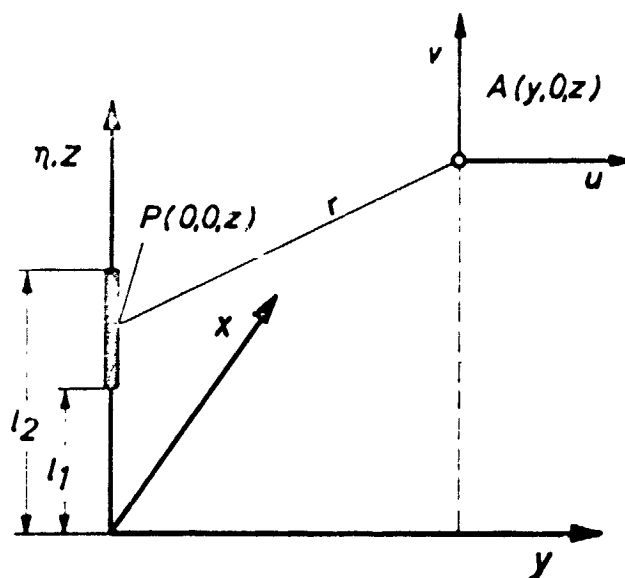
Differentiation provides the velocities at the field point A:

$$u = \frac{\partial \phi}{\partial y} = \frac{\dot{V}}{4\pi} \cdot \frac{y}{[y^2 + (z-l)^2]^{3/2}} \quad (9.32)$$

$$v = \frac{\partial \phi}{\partial z} = \frac{\dot{V}}{4\pi} \cdot \frac{z-l}{[y^2 + (z-l)^2]^{3/2}} \quad (9.33)$$

Line source:

$$\phi = - \frac{1}{4\pi} \cdot \frac{\dot{V}}{l} \int \frac{1}{r} \cdot ds \quad (3.3)$$



$$\phi = - \frac{1}{4\pi} \cdot \frac{\dot{V}}{l} \int_{l_1}^{l_2} \frac{d\eta}{\sqrt{(z-\eta)^2 + y^2}} \quad (9.34)$$

where η is the moving coordinate of the source in the z direction.

$$u = \frac{\partial \phi}{\partial y} = \frac{1}{4\pi} \cdot \frac{\dot{V}}{l} \int_{l_1}^{l_2} \frac{y}{[(z-\eta)^2 + y^2]^{3/2}} d\eta \quad (9.35)$$

The integral gives

$$u = - \frac{1}{4\pi} \cdot \frac{\dot{V}}{l \cdot y} \cdot \left(\frac{z-\eta}{\sqrt{(z-\eta)^2 + y^2}} \right) \Big|_{l_1}^{l_2} \quad (9.36)$$

$$= - \frac{1}{4\pi} \cdot \frac{\dot{V}}{l \cdot y} \cdot \left(\frac{z-l_2}{\sqrt{(z-l_2)^2 + y^2}} - \frac{z-l_1}{\sqrt{(z-l_1)^2 + y^2}} \right) \quad (9.37)$$

$$V = \frac{\partial \phi}{\partial z} = \frac{1}{4\pi} \cdot \frac{\dot{V}}{l} \int_{l_1}^{l_2} \frac{z-\eta}{[(z-\eta)^2 + y^2]^{3/2}} d\eta \quad (9.38)$$

$$= \frac{1}{4\pi} \cdot \frac{\dot{V}}{l} \cdot \left(\frac{1}{\sqrt{(z-\eta)^2 + y^2}} \right) \Big|_{l_1}^{l_2}$$

$$V = \frac{1}{4\pi} \cdot \frac{\dot{V}}{l} \cdot \left(\frac{1}{\sqrt{(z-l_2)^2 + y^2}} - \frac{1}{\sqrt{(z-l_1)^2 + y^2}} \right) \quad (9.39)$$

Circular area source

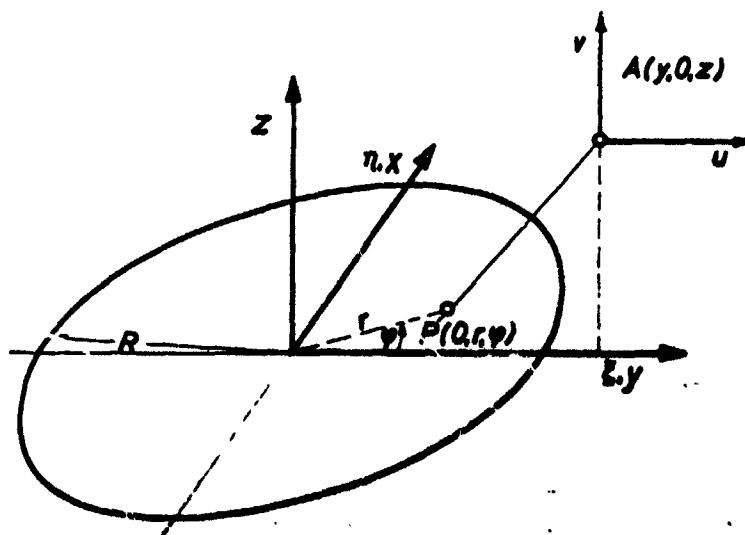
If one covers a circular disk with the sink distribution

$$q = \frac{\dot{V}}{F} \quad (9.40)$$

the potential equation for such a surface is

$$\phi = \frac{q}{4\pi} \iint_F \frac{d\xi \cdot d\eta}{\sqrt{(x-\xi)^2 + (y-\eta)^2 + z^2}} \quad (9.41)$$

where ξ and η are the coordinates of the area sink.



Because of the rotational symmetry, the field point A may be placed in the x-y plane.

If we select polar coordinates, then we have for the

Inducing point P:

Field point A:

$$\xi = r \cdot \cos \varphi$$

$$y = y$$

$$\eta = r \cdot \sin \varphi$$

$$x = 0$$

$$z = 0$$

$$z = z.$$

The potential equation of the area sink in polar coordinates is:

$$\phi = \frac{q}{4\pi} \int_0^{2\pi} \int_0^R \frac{r \cdot dr \cdot d\varphi}{\sqrt{r^2 - 2y \cdot r \cdot \cos \varphi + y^2 + z^2}}. \quad (9.42)$$

Then the radial velocity component u is:

$$u = \frac{\partial \phi}{\partial y} = - \frac{q}{4\pi} \int_0^{2\pi} \int_0^R \frac{(-2r \cdot \cos \varphi + 2y) \cdot r \cdot dr \cdot d\varphi}{2(\sqrt{r^2 - 2y \cdot r \cdot \cos \varphi + y^2 + z^2})^3}. \quad (9.43)$$

The integral is split up and integrated separately:

$$u = - \frac{q}{4\pi} \int_0^{2\pi} \left[\int_0^R \frac{-r^2 \cdot \cos \varphi \cdot dr}{(\sqrt{\quad})^3} + \int_0^R \frac{r \cdot y \cdot dr}{(\sqrt{\quad})^3} \right] d\varphi. \quad (9.44)$$

According to Bronstein-Semendjajew Integral No. 253 [9]:

$$-\cos \varphi \int_0^R \frac{r^2 \cdot dr}{(\sqrt{\quad})^3} = -\cos \varphi \cdot \left\{ \frac{[2 \cdot y^2 \cdot \cos^2 \varphi - (y^2 + z^2)] \cdot r - y \cdot \cos \varphi (y^2 + z^2)}{[(y^2 + z^2) - y^2 \cdot \cos^2 \varphi] \cdot \sqrt{\quad}} \right. \\ \left. + \ln [2 \cdot (\sqrt{\quad} + r - y \cdot \cos \varphi)] \right\} \Big|_0^R$$

and according to Bronstein-Semendjajew Integral No. 250 [9]:

$$\int_0^R \frac{y \cdot r \cdot dr}{(\sqrt{\quad})^3} = - \frac{[-y \cdot r \cdot \cos \varphi + (y^2 + z^2)] \cdot y}{(y^2 + z^2) - y^2 \cdot \cos^2 \varphi \cdot \sqrt{\quad}} \Big|_0^R$$

$$\begin{aligned}
u = & -\frac{q}{4\pi} \int_0^{2\pi} \left\{ y \cdot \left[\frac{R \cdot y \cdot \cos \varphi - y^2 - z^2}{(y^2 + z^2 - y^2 \cos^2 \varphi) \cdot \sqrt{R^2 - 2Ry \cos \varphi + y^2 + z^2}} \right. \right. \\
& + \left. \frac{y^2 + z^2}{(y^2 + z^2 - y^2 \cos^2 \varphi) \sqrt{y^2 + z^2}} \right] - \cos \varphi \left(\frac{2Ry^2 \cos^2 \varphi - Ry^2 - Rz^2 - y \cos \varphi (y^2 - z^2)}{(y^2 + z^2 - y^2 \cos^2 \varphi) \sqrt{R^2 - 2Ry \cos \varphi + y^2 + z^2}} \right. \\
& + \left. \frac{y \cos \varphi (y^2 + z^2)}{(y^2 + z^2 - y^2 \cos^2 \varphi) \sqrt{y^2 + z^2}} + \ln \left[2 \cdot (\sqrt{R^2 - 2Ry \cos \varphi + y^2 + z^2} + R - y \cos \varphi) \right] \right. \\
& \left. \left. - \ln \left[2 \cdot (\sqrt{y^2 + z^2} - y \cos \varphi) \right] \right) \right\} d\varphi .
\end{aligned} \quad (9.45)$$

The vertical velocity component v is

$$v = \frac{\partial \phi}{\partial z} = -\frac{q}{4\pi} \int_0^{2\pi} \int_0^R \frac{z \cdot r \cdot dr \cdot d\varphi}{(\sqrt{r^2 - 2yr \cos \varphi + y^2 + z^2})^3} . \quad (9.46)$$

The integration is performed according to Bronstein-Semendjajew
Integral No. 250 [9]

$$\begin{aligned}
V &= -\frac{q}{4\pi} \int_0^{2\pi} z \cdot \left(\frac{-[-y \cdot r \cdot \cos \varphi + (y^2 + z^2)]}{(y^2 + z^2) + y^2 \cos^2 \varphi \cdot \sqrt{r^2 - 2y \cdot r \cdot \cos \varphi + y^2 + z^2}} \right) \Big|_0^R d\varphi \\
V &= -\frac{q}{4\pi} \int_0^{2\pi} z \cdot \left[-\frac{R \cdot y \cdot \cos \varphi - y^2 + z^2}{(y^2 + z^2 - y^2 \cos^2 \varphi) \sqrt{R^2 - 2Ry \cdot \cos \varphi + y^2 + z^2}} \right. \\
&\quad \left. - \frac{y^2 + z^2}{(y^2 + z^2 - y^2 \cos^2 \varphi) \sqrt{y^2 + z^2}} \right] d\varphi .
\end{aligned} \tag{9.47}$$

/ 94

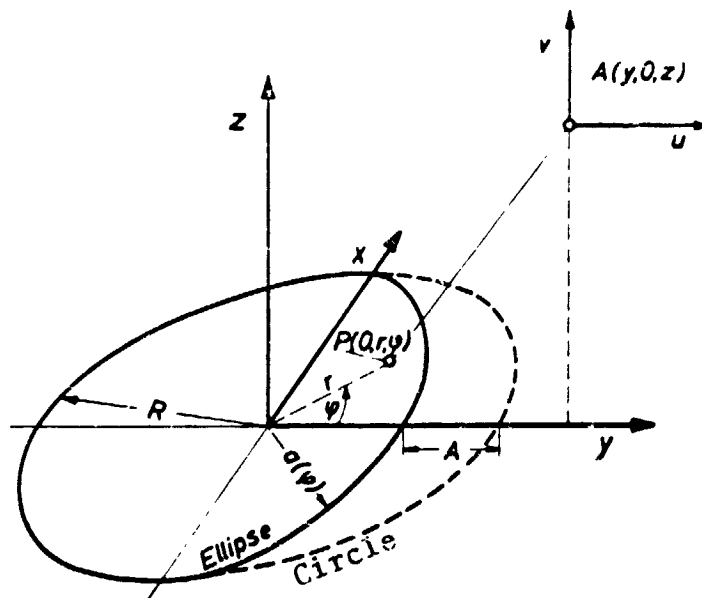
Elliptical area source

This is described by the potential equation (9.41), in which we insert

$$a(\varphi) = R - R \cdot |\cos \varphi| \tag{9.48}$$

for the integration limit R .

As the flow is to be calculated only for the y - z plane, the field point A may also lie in this plane. The solution is reached as for the circular area source, with, to be sure, the new integration limit a .



Circular ring source

The potential equation for a circular ring source is derived from the line source

$$\phi = - \frac{\dot{V}}{4\pi \cdot l} \int_s \frac{1}{r} \cdot ds \quad (3.3)$$

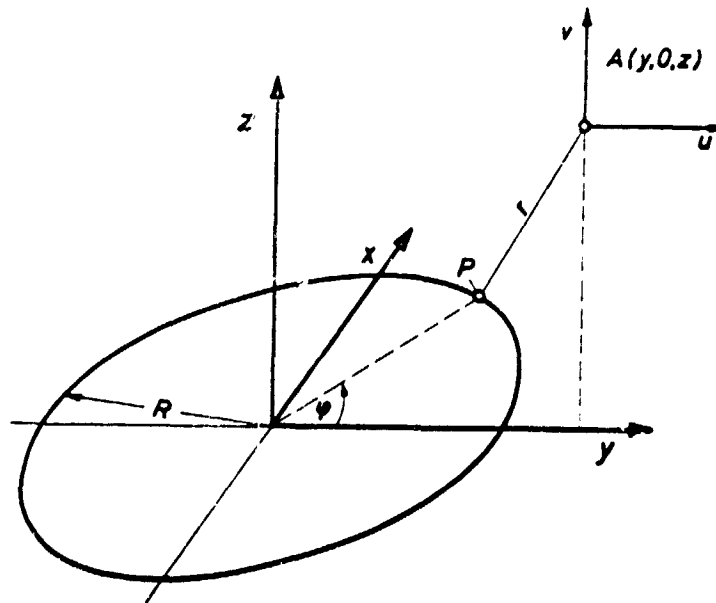
with the sink distribution

$$q = \frac{\dot{V}}{l} \quad (9.49)$$

and the segment R expressed in polar coordinates becomes the potential equation of the circular ring source

/ 95

$$\phi = -\frac{q}{4\pi} \int_0^{2\pi} \frac{R \cdot d\varphi}{\sqrt{y^2 - R^2 + z^2 - 2R \cdot y \cdot \cos\varphi}} \quad (9.50)$$

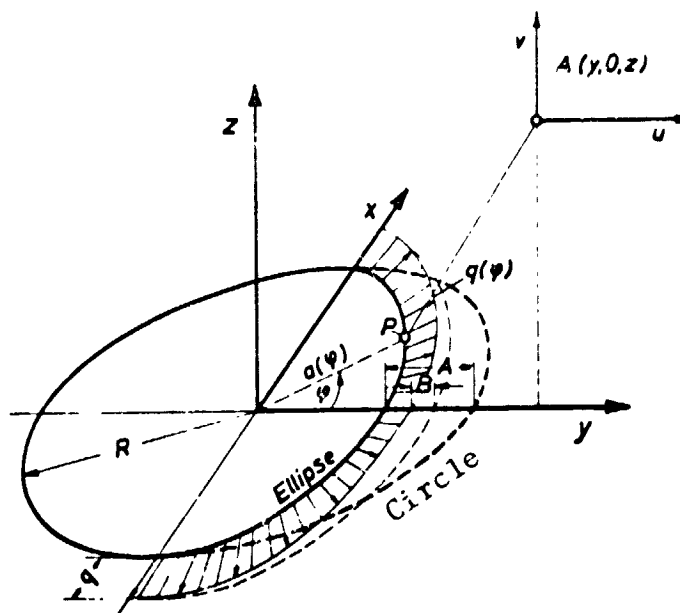


$$u = \frac{\partial \phi}{\partial y} = \frac{q}{4\pi} \int_0^{2\pi} \frac{R \cdot (y - R \cdot \cos\varphi)}{(y^2 - R^2 + z^2 - 2R \cdot y \cdot \cos\varphi)^{3/2}} d\varphi \quad (9.51)$$

$$v = \frac{\partial \phi}{\partial z} = \frac{q}{4\pi} \int_0^{2\pi} \frac{R \cdot z}{(y^2 - R^2 + z^2 - 2R \cdot y \cdot \cos\varphi)^{3/2}} d\varphi \quad (9.52)$$

Elliptical ring source with variable source distribution

The potential equation of the circular ring source, Equation 9.50, applies here.



In Equations 9.51 and 9.52 we place, instead of the constant source radius, the variable

$$a(\psi) = R - R \cdot |\cos \psi| \quad (9.53)$$

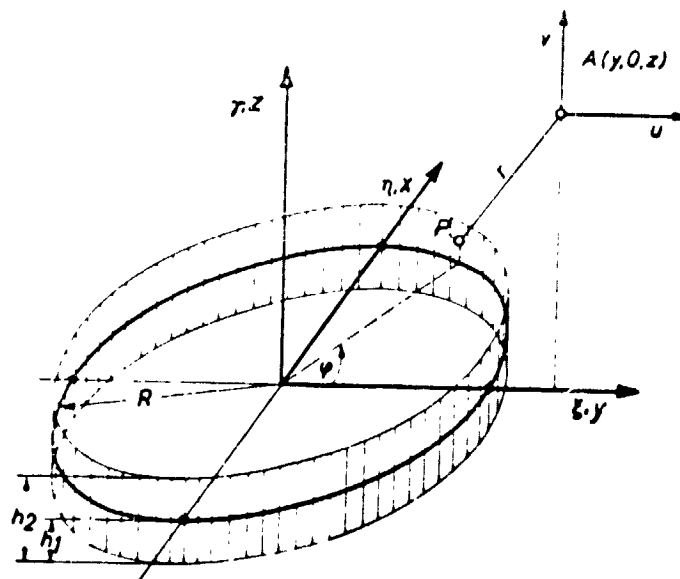
and for the variable sink distribution

$$q(\psi) = q - \beta \cdot |\cos \psi| \quad (9.54)$$

Source on the covering surface of a circular cylinder

Proceeding from the potential equation of the area source, 3.4,

$$\phi = -\frac{1}{4\pi} \cdot \frac{\dot{V}}{F} \iint_F \frac{d\eta \cdot d\beta}{\sqrt{(y-\beta)^2 + \eta^2 + (z-\gamma)^2}} \quad (9.55)$$



in which the distance between the inducing point P and the field point A is expressed in polar coordinates

$$\xi = R \cdot \cos \varphi$$

$$\eta = R \cdot \sin \varphi$$

γ

the potential equation of a source on the surface of a cylinder becomes

$$\phi = \frac{1}{4\pi} \cdot \frac{\dot{V}}{F} \int_0^{2\pi} \int_{h_1}^{h_2} \frac{R \cdot d\varphi \cdot d\gamma}{\sqrt{y^2 - 2y \cdot R \cdot \cos \varphi + z^2 - 2z \cdot \gamma + R^2 + \gamma^2}} \quad (9.56)$$

Differentiation with respect to y leads to the radial velocity component u

$$u = \frac{\partial \phi}{\partial y} = \frac{1}{4\pi} \cdot \frac{\dot{V}}{F} \int_0^{2\pi} \int_{h_1}^{h_2} \frac{(y - R \cdot \cos \varphi) \cdot R \cdot d\varphi \cdot d\gamma}{(\sqrt{y^2 - 2y \cdot R \cdot \cos \varphi + z^2 - 2z \cdot \gamma + R^2 + \gamma^2})^3} \quad (9.57)$$

The integral is split up and integrated separately

$$u = \frac{1}{4\pi} \cdot \frac{\dot{V}}{F} \int_0^{2\pi} \left[- \int_{h_1}^{h_2} \frac{R^2 \cdot \cos \varphi \cdot d\gamma}{(\sqrt{\quad})^3} + \int_{h_1}^{h_2} \frac{y \cdot R \cdot d\gamma}{(\sqrt{\quad})^3} \right] \cdot d\varphi .$$

According to Bronstein-Semendja [w Integral No. 242 [9],

/ 98

$$\int_{h_1}^{h_2} \frac{d\gamma}{(\sqrt{\quad})^3} = \frac{\gamma - z}{(y^2 + R^2 - 2y \cdot R \cdot \cos \varphi) \sqrt{(y^2 + R^2 - 2y \cdot R \cdot \cos \varphi)(y^2 + R^2 + z^2 - 2y \cdot R \cdot \cos \varphi)}} \Big|_{h_1}^{h_2}$$

so that

$$u = \frac{1}{4\pi} \cdot \frac{\dot{V}}{F} \int_0^{2\pi} \left[(y \cdot R - R^2 \cdot \cos \varphi) \cdot \left(\frac{h_2 - z}{NE2} - \frac{h_1 - z}{NE1} \right) \right] \cdot d\varphi . \quad (9.58)$$

Here

$$NE2 = (y^2 + R^2 - 2y \cdot R \cdot \cos \varphi) \sqrt{(h_2^2 - 2zh_2 + y^2 + R^2 + z^2 - 2y \cdot R \cdot \cos \varphi)} \quad (9.59)$$

and

$$NE1 = (y^2 + R^2 - 2y \cdot R \cdot \cos \varphi) \sqrt{(h_1^2 - 2zh_1 + y^2 + R^2 + z^2 - 2y \cdot R \cdot \cos \varphi)} . \quad (9.60)$$

The vertical velocity component v is obtained from differentiation with respect to z

$$\begin{aligned} v &= \frac{\partial \phi}{\partial t} = \frac{1}{4\pi} \cdot \frac{\dot{V}}{F} \int_0^{2\pi} \int_{h_1}^{h_2} \frac{(z - \gamma) \cdot R \cdot d\varphi \cdot d\gamma}{(\sqrt{z^2 - 2z\gamma + y^2 + R^2 + \gamma^2 - 2y \cdot R \cdot \cos \varphi})^3} \\ &= \frac{1}{4\pi} \cdot \frac{\dot{V}}{F} \int_0^{2\pi} \left[\int_{h_1}^{h_2} \frac{z \cdot R \cdot d\gamma}{(\sqrt{\quad})^3} - \int_{h_1}^{h_2} \frac{\gamma \cdot R \cdot d\gamma}{(\sqrt{\quad})^3} \right] \cdot d\varphi . \end{aligned} \quad (9.61)$$

The first part of the equation is Integral No 2+2, which we have already solved. The second part can be solved by use of the Bronstein-Semendjajew Integral No. 250 [9]:

$$\int \frac{\delta d\gamma}{(\sqrt{\quad})^3} = \frac{z \cdot \gamma - y^2 - R^2 - z^2 - 2y \cdot R \cdot \cos \varphi}{(y^2 + R^2 - 2y \cdot R \cdot \cos \varphi) \sqrt{\gamma^2 - 2z \cdot \gamma + y^2 + R^2 + z^2 - 2y \cdot R \cdot \cos \varphi}} \Big|_{h_1}^{h_2}.$$

Now

/ 99

$$V = \frac{1}{4\pi} \cdot \frac{\dot{V}}{F} \int_0^{2\pi} \left[z \cdot R \cdot \left(\frac{h_2 - z}{NE2} - \frac{h_1 - z}{NE1} \right) - R \cdot \left(\frac{z \cdot h_2 - y^2 - R^2 - z^2 + 2yR \cos \varphi}{NE2} - \frac{z \cdot h_1 - y^2 - R^2 - z^2 + 2yR \cos \varphi}{NE1} \right) \right] d\varphi \quad (9.62)$$

in which NE1 and NE2 are the expressions introduced on the previous page.

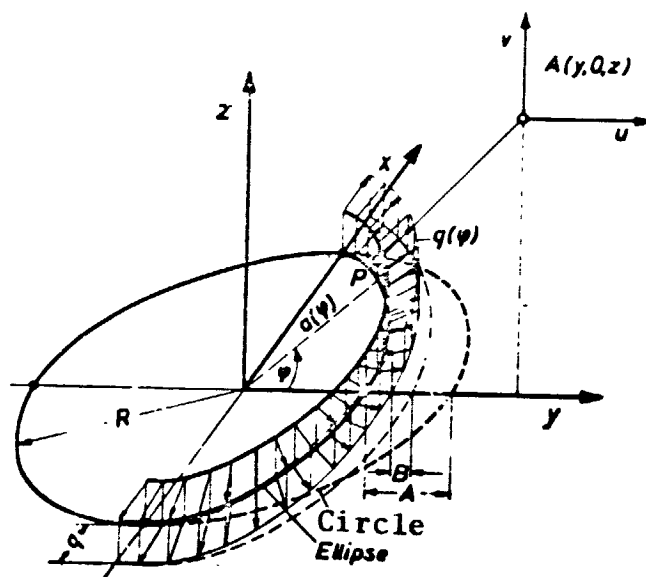
Source with variable source distribution on the surface of a cylinder with an elliptical base.

The potential equation set up in the last section, 9.56, applies here. Now, in the potential equation and in the velocity components u and v calculated from it we must insert instead of R

$$a(\varphi) = R - R \cdot |\cos \varphi| \quad (9.63)$$

and instead of the constant source distribution q we must insert

$$q(\varphi) = q - \beta \cdot |\cos \varphi| \quad (9.6.1)$$



/ 100

9.3 Ascending flow

Special abbreviations in Section 9.3

- A Buoyant force
- p Pressure
- R Gas constant
- u Velocity component in the positive x direction
- v Velocity component in the positive y direction
- x Vertical coordinate, out from the origin in the direction of flow
- y Horizontal coordinate, out from the origin across the direction of flow
- β Expansion coefficient of gases
- κ Isentropy exponent

Starting equations:

In this section, we shall show how one proceeds from the general equation system 3.7, 3.8, 3.9 to the special equation system 3.10, 3.11, 3.12 for turbulent convective flows.

Continuity equation:

$$\frac{\partial \rho \cdot u}{\partial x} + \frac{\partial \rho \cdot v}{\partial y} = 0 \quad (3.7)$$

Motion equation:

$$\rho \cdot \left(\frac{\partial u}{\partial t} + u \cdot \frac{\partial u}{\partial x} + v \cdot \frac{\partial u}{\partial y} \right) = X - \frac{\partial P}{\partial x} + \mu \cdot \left(\frac{\partial^2 u}{\partial x^2} + \frac{\partial^2 u}{\partial y^2} \right) \quad (3.8)$$

Energy equation:

$$\rho \cdot c_p \cdot \left(\frac{\partial T}{\partial t} + u \cdot \frac{\partial T}{\partial x} + v \cdot \frac{\partial T}{\partial y} \right) = \lambda \cdot \left(\frac{\partial^2 T}{\partial x^2} + \frac{\partial^2 T}{\partial y^2} \right) \quad (3.9)$$

Simplifications:

$$\text{Time term:} \quad \frac{\partial T}{\partial t} \approx 0$$

$$\text{Pressure term:} \quad \frac{\partial P}{\partial x} \approx 0$$

$$\text{Friction term:} \quad \mu \cdot \left(\frac{\partial^2 u}{\partial x^2} + \frac{\partial^2 u}{\partial y^2} \right) \approx 0$$

$$\text{Heat conductivity:} \quad \lambda \cdot \left(\frac{\partial^2 T}{\partial x^2} + \frac{\partial^2 T}{\partial y^2} \right) \approx 0$$

According to Reichardt [50] the pressure term and the friction term for flows of the free turbulence may be neglected.

/101

Potential temperature

Pressure and temperature in the free atmosphere change with the altitude. The buoyant force of a rising volume of air changes both because of the decrease in pressure and due to the change in ambient temperature.

Assuming an adiabatic change of state, a new temperature is defined in meteorology. This is the potential temperature, which is independent of the variation of the pressure.

The potential temperature θ of dry air is the temperature which a volume of air assumes if it is brought adiabatically from its actual pressure p to a reference pressure p_0 , usually the pressure at ground level.

Therefore:

$$\theta = T \cdot \left(\frac{p_0}{p} \right)^{\frac{\kappa-1}{\kappa}} \quad (9.65)$$

in which T is the actual absolute temperature of the air volume.

The gradient of the potential temperature (temperature change/path distance, °C/m) can be expressed well by the gradients of the actual absolute temperature and the adiabatic gradient:

$$\begin{aligned} \frac{1}{\theta} \cdot \frac{d\theta}{dx} &= \frac{1}{T} \cdot \frac{dT}{dx} - \left(\frac{\kappa-1}{\kappa} \right) \cdot \frac{1}{p} \cdot \frac{dp}{dx} \\ &= \frac{1}{T} \cdot \frac{dT}{dx} + \left(\frac{\kappa-1}{\kappa} \right) \cdot \frac{g}{R \cdot T} \end{aligned}$$

with

$$\begin{aligned}\Delta p &= -g \cdot \rho \cdot \Delta x \\ \Delta x \rightarrow 0 : \quad \frac{dp}{dx} &= -g \cdot \rho \\ \frac{1}{p} \cdot \frac{dp}{dx} &= - \frac{g}{R \cdot T}\end{aligned}$$

The expression

$$\Gamma = \frac{\kappa-1}{\kappa} \cdot \frac{g}{R} \quad (9.65)$$

is called the adiabatic gradient.

For the atmosphere,

$$\Gamma \approx \frac{1^\circ\text{C}}{100\text{m}} = 0,01 \left[\frac{^\circ\text{C}}{\text{m}} \right] .$$

Thus, the gradient of the potential temperature becomes

$$\frac{1}{\theta} \frac{d\theta}{dx} = \frac{1}{T} \left(\frac{dT}{dz} + \Gamma \right) . \quad (9.67)$$

At the ground, the potential temperature and the absolute temperature are identical by definition. Near the ground, then, this approximation holds:

$$\theta = T + \Gamma \cdot x . \quad (9.68)$$

Figure 50 shows the course of the absolute and the potential temperature as a function of the altitude.

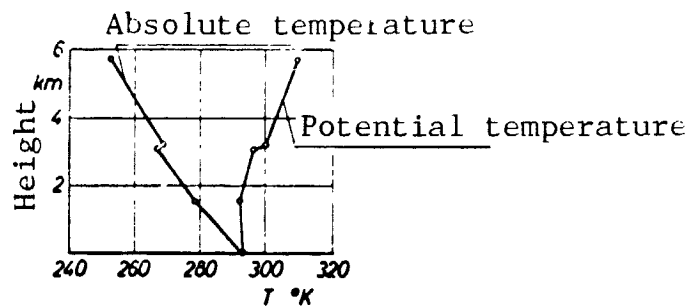


Figure 50. Absolute and potential temperature in the atmosphere.
(1 August 1957, Seattle, USA)

/ 103

In the equation of motion, X is the buoyant force per unit volume in the x direction:

$$X = \frac{F}{l^3} \quad (9.69)$$

where

$$F = g \cdot l^3 \cdot (\rho_a - \rho) \quad (9.70)$$

l is a length unit, and ρ_a, ρ the densities outside and inside the rising air stream, respectively. With the general gas equation

$$\rho = \frac{p}{R \cdot T}$$

we obtain

$$X = g \cdot \rho \cdot \frac{T \cdot (\rho_a \cdot T - T_a \cdot \rho)}{\rho \cdot (T_a \cdot T)} \quad (9.71)$$

As p is constant on one line of altitude, we obtain

$$X = g \cdot \rho \cdot \frac{\Delta T}{T_a} . \quad (9.72)$$

We introduce the potential temperature

$$X = g \cdot \rho \cdot \beta \cdot \theta' \quad (9.73)$$

where

$$\beta = \frac{1}{\theta_a}$$

is the expansion coefficient of gases, and

$$\theta' = \theta - \theta_a . \quad (9.74)$$

θ and θ_a are the potential temperatures inside and outside the rising volume.

/ 104

As Murgai and Emmons [45] have shown, the absolute temperature in the energy equation can be replaced with the potential temperature. With this assumption, we obtain the equation system for a laminar ascending flow.

Continuity:

$$\frac{\partial \rho \cdot u}{\partial x} + \frac{\partial \rho \cdot v}{\partial y} = 0 \quad (9.75)$$

Motion:

$$u \cdot \frac{\partial u}{\partial x} + v \cdot \frac{\partial u}{\partial y} = g \cdot \rho \cdot \beta \cdot (\theta - \theta_a) \quad (9.76)$$

Energy:

$$\rho \cdot c_p \cdot \left(u \cdot \frac{\partial \theta}{\partial x} + v \cdot \frac{\partial \theta}{\partial y} \right) = 0 \quad (9.77)$$

Turbulent ascending flow

Now we introduce turbulent fluctuation quantities into equation system 9.75, 9.76, 9.77. The quantities with dashes above them are time averages. Primed quantities indicate momentary variations:

$$\begin{aligned} u &= \bar{u} + u' \\ v &= \bar{v} + v' \\ \theta &= \bar{\theta} + \theta' \\ \rho &= \bar{\rho} + \rho' \end{aligned}$$

Density variations are neglected!

Continuity:

$$\frac{\partial}{\partial x} (\bar{u} + u') + \frac{\partial}{\partial y} (\bar{v} + v') = 0 \quad (9.78)$$

As the flow is supposed to be steady, on a time average, then

$$\frac{\partial \bar{u}}{\partial x} + \frac{\partial \bar{v}}{\partial y} + \frac{\partial \bar{u}'}{\partial x} + \frac{\partial \bar{v}'}{\partial y} = 0$$

$$\frac{\partial \bar{u}'}{\partial x} = - \frac{\partial \bar{v}'}{\partial y} = 0$$

$$\frac{\partial \bar{v}'}{\partial x} = - \frac{\partial \bar{u}'}{\partial y} = 0$$

/ 105

Continuity:

$$\frac{\partial \bar{u}}{\partial x} + \frac{\partial \bar{v}}{\partial y} = 0 \quad (9.79)$$

As one can write

$$\frac{\partial u^2}{\partial x} + \frac{\partial u \cdot v}{\partial y} = \cancel{u \cdot \frac{\partial u}{\partial x}} + \cancel{u \cdot \frac{\partial v}{\partial y}} + u \cdot \frac{\partial u}{\partial x} + v \cdot \frac{\partial u}{\partial y}$$

the motion equation 9.76 becomes

$$\begin{aligned} \frac{\partial u^2}{\partial x} + \frac{\partial u \cdot v}{\partial y} &= g \cdot \beta \cdot (\theta - \theta_a) \\ &= u \cdot \frac{\partial u}{\partial x} + v \cdot \frac{\partial u}{\partial y} \end{aligned} \quad (9.80)$$

Insertion of the turbulent fluctuation quantities gives:

$$\rho \left[\frac{\partial}{\partial x} (\bar{u}^2 + 2\bar{u} \cdot u' + u'^2) + \frac{\partial}{\partial y} (\bar{u} \cdot \bar{v} + 2\bar{u} \cdot v' + u' \cdot v') \right] = \rho \cdot g \cdot \beta \cdot (\bar{\theta} + \bar{\theta}' - \theta_a) \quad (9.81)$$

For the flow which is steady on a time average, we have

$$\begin{aligned} 2 \cdot \frac{\partial (\bar{u} \cdot u')}{\partial x} &= 0 \\ \frac{\partial (\bar{u} \cdot \bar{v}')}{\partial y} &= \frac{\partial (\bar{u} \cdot v')}{\partial y} = 0 \\ \overline{g \cdot \beta \cdot \theta} &= 0 \end{aligned}$$

Now the equation of motion is

$$\rho \cdot \left(\bar{u} \cdot \frac{\partial \bar{u}}{\partial x} + \bar{v} \cdot \frac{\partial \bar{u}}{\partial y} \right) = \rho \cdot g \cdot \beta \cdot (\bar{\theta} - \theta_a) - \rho \cdot \left(\frac{\partial \bar{u}'}{\partial x} + \frac{\partial \bar{u}'v'}{\partial y} \right) \quad (9.82)$$

Fluctuation products, $\overline{u'^2}$ are neglected!

The expression

$$\frac{\partial u \cdot \theta}{\partial x} + \frac{\partial v \cdot \theta}{\partial y} = u \cdot \frac{\partial \theta}{\partial x} + v \cdot \frac{\partial \theta}{\partial y} + \theta \cdot \left(\frac{\partial u}{\partial x} + \frac{\partial v}{\partial y} \right)$$

and the insertion of the turbulent fluctuation quantities into the energy equation, 9.77, gives

$$\rho \cdot c_p \cdot \left[\frac{\partial}{\partial x} (\bar{u} \bar{\theta} + \bar{u}' \theta' + u' \bar{\theta} + u' \theta') + \frac{\partial}{\partial y} (\bar{v} \bar{\theta} + \bar{v}' \theta' + v' \bar{\theta} + v' \theta') \right] = 0 \quad (9.83)$$

/106

Because of the time averaging,

$$\frac{\partial \overline{u' \theta'}}{\partial x} = \frac{\partial \overline{u' \bar{\theta}}}{\partial x} = \frac{\partial \overline{\bar{v} \theta'}}{\partial y} = \frac{\partial \overline{v' \bar{\theta}}}{\partial y} = 0$$

According to Reichardt [50] we may neglect the fluctuation product $\overline{\theta' \cdot u'}$. Thus, the energy equation becomes

$$\rho \cdot c_p \cdot \left(\bar{u} \cdot \frac{\partial \bar{\theta}}{\partial x} + \bar{v} \cdot \frac{\partial \bar{\theta}}{\partial y} + \frac{\partial \bar{\theta}' v'}{\partial y} \right) = 0 \quad (9.84)$$

The new equation system for the turbulent ascending flow is:

Continuity:

$$\frac{\partial \bar{u}}{\partial x} + \frac{\partial \bar{v}}{\partial y} = 0 \quad (9.79)$$

Motion:

$$\rho \cdot \left(\bar{u} \cdot \frac{\partial \bar{u}}{\partial x} + \bar{v} \cdot \frac{\partial \bar{u}}{\partial y} \right) = \rho \cdot g \cdot \beta \cdot (\bar{\theta} - \theta_0) - \rho \cdot \frac{\partial}{\partial y} (\overline{u'v'}) \quad (9.82)$$

Energy:

$$\rho \cdot c_p \cdot \left(\bar{u} \cdot \frac{\partial \bar{\theta}}{\partial x} + \bar{v} \cdot \frac{\partial \bar{\theta}}{\partial y} \right) = - \rho \cdot c_p \cdot \frac{\partial}{\partial y} (\overline{\theta'v'}) \quad (9.84)$$

The turbulent heat conduction in the direction of flow

$$\frac{\partial}{\partial x} (\overline{\theta'u'})$$

is small in comparison to the turbulent heat conduction in the horizontal direction. The heat flux density produced by the turbulence transverse to the flow direction is

$$q = \rho \cdot c_p \cdot \overline{\theta'v'}$$

If we introduce into the equation system 9.79, 9.82, 9.84:

$\tau = -\rho \cdot \overline{u'v'}$	apparent turbulent viscosity
$q = \rho \cdot c_p \cdot \overline{\theta'v'}$	turbulent heat conduction
$\theta' = \bar{\theta} - \theta_0$	temperature difference

then the equation system for the plane turbulent convection flow in the gravity field of the earth becomes: / 107

Continuity:

$$\frac{\partial \bar{u}}{\partial x} + \frac{\partial \bar{v}}{\partial y} = 0 \quad (3.10)$$

Motion:

$$\rho \cdot \left(\bar{u} \cdot \frac{\partial \bar{u}}{\partial x} + \bar{v} \cdot \frac{\partial \bar{u}}{\partial y} \right) = \rho \cdot g \cdot \frac{\bar{\theta} - \theta_a}{\theta_a} - \rho \cdot \frac{\partial \tau}{\partial y} \quad (3.11)$$

Energy:

$$\rho \cdot \left(\bar{u} \cdot \frac{\partial \theta'}{\partial x} + \bar{v} \cdot \frac{\partial \theta'}{\partial y} + \bar{u} \cdot \frac{\partial \theta_a}{\partial x} + \bar{v} \cdot \frac{\partial \theta_a}{\partial y} \right) = - \frac{1}{c_p} \cdot \frac{\partial q}{\partial y} \quad (9.85)$$

Now, if we set $\frac{\partial \theta_a}{\partial y} = 0$, because the ambient temperature is constant on an altitude line, and if we introduce the gradient of the potential temperature

$$\frac{\partial \theta_a}{\partial x} = \frac{d\theta_a}{dx}$$

then the energy equation becomes

$$\rho \cdot \left(\bar{u} \cdot \frac{\partial \theta'}{\partial x} + \bar{v} \cdot \frac{\partial \theta'}{\partial y} \right) = - \frac{1}{c_p} \cdot \frac{\partial q}{\partial y} - \rho \cdot \bar{u} \cdot \frac{d\theta_a}{dx} \quad (3.12)$$

Integration of Equations 3.10, 3.11, 3.12.

We assume a rectangular profile for the distribution of the velocity and the temperature in the ascending flow:

$$\left. \begin{array}{l} -b \leq y \leq b \\ u_{(x,y)} = u_m(x) = \text{const.} \\ \theta'_{(x,y)} = \theta'_m(x) = \text{const.} \end{array} \right\} \text{ for } x = \text{constant}$$

Outside the ascending flow

$$u_m = C_m = 0 .$$

Integration of the continuity equation

/108

$$\frac{d}{dx} \int_0^b u_m \cdot dy + \bar{v} \Big|_0^b = 0 \quad (9.86)$$

$$\frac{d}{dx} (u_m \cdot b) = - \bar{v} \Big|_0^b . \quad (9.87)$$

For $y = b$, v_b is the inflow velocity of the surrounding air.
According to Morton-Taylor-Turner [44]

$$\bar{v}_b = \alpha \cdot u_m \quad (3.15)$$

Continuity:

$$\frac{d}{dx} u_m \cdot b = \alpha \cdot u_m . \quad (3.16)$$

Integration of the motion equation:

$$\frac{d}{dx} \int_0^b \rho \cdot \bar{u}^2 \cdot dy + \rho \cdot \bar{v} \cdot \bar{u} \Big|_0^b = \int_0^b \rho \cdot g \cdot \frac{\bar{\theta} - \theta_a}{\theta_a} \cdot dy - \tau \Big|_0^b . \quad (9.88)$$

For $u = u_m = \text{constant}$ and $\theta = \theta_m = \text{constant}$, within the limits $-b$ to $+b$, this relation applies:

$$\frac{d}{dx} b \cdot u_m^2 \Big|_0^b + \rho \cdot \bar{v} \cdot \bar{u} \Big|_0^b = \rho \cdot g \cdot b \frac{\theta'_m}{\theta_a} \Big|_0^b - \tau \Big|_0^b . \quad (9.89)$$

The thrust potential term vanishes, as Schmidt [57] has proved, because $\bar{v} = 0$ on the jet axis and $\bar{u} = 0$ at the edge of the jet. Therefore, the motion equation is:

$$\frac{d}{dx} b \cdot u_m^2 = g \cdot b \cdot \frac{\theta_m'}{\theta_a} \quad (3.17)$$

Integration of the motion equation:

$$\frac{d}{dx} \int_0^b \rho \cdot \bar{u} \cdot \theta' \cdot dy + \rho \cdot \bar{v} \cdot \theta' \Big|_0^b = - \int_0^b \rho \cdot \bar{u} \cdot \frac{d\theta_a}{dx} \cdot dy - \frac{1}{c_p} \cdot q \Big|_0^b \quad (9.90)$$

/109

As $\bar{v} = v' = 0$ on the x axis, and $\theta' = 0$ at the edge of the jet, then

$$\begin{aligned} \rho \cdot \bar{v} \cdot \theta' \Big|_0^b &= 0 \\ q &= \rho \cdot c_p \cdot \theta' \cdot v' \Big|_0^b = 0 \\ \frac{d}{dx} u_m \cdot \theta_m' \cdot b &= - u_m \cdot b \cdot \frac{d\theta_a}{dx} \end{aligned}$$

Energy equation:

$$\frac{d}{dx} g \cdot b \cdot u_m \cdot \frac{\theta_m'}{\theta_a} = - u_m \cdot b \cdot g \cdot \frac{1}{\theta_a} \cdot \frac{d\theta_a}{dx} \quad (3.18)$$

Special abbreviations in sections 9.4 and 9.5

A	Buoyant force
a	Coefficient
c	Factor
C_s	Black body radiation coefficient
$h_{0.5 q_{\max}}$	Height at which the half-maximum value of the dynamic pressure occurs
$h_{0.5 u_{\max}}$	Height at which the half-maximum value of the velocity occurs
$h_{0.5 \theta_{\max}}$	Height at which the half-maximum value of the excess temperature occurs
I	Momentum flow
Nu	Nusselt number
P	Power
p	Pressure
Pr	Prandtl number
Δq	Pitot probe measuring error
R	Gas constant
R^*	Separation radius
r^*	Thermocouple recovery factor
$R_{0.5 q_{\max}}$	Radius at which half the axial value of the dynamic pressure occurs
$R_{0.5 u_{\max}}$	Radius at which half the axial value of the velocity occurs
$R_{0.5 \theta_{\max}}$	Radius at which half the axial value of the total excess temperature occurs
R_s	Probe radius
T	Time for one period
T_u	Degree of turbulence
w	Inflow velocity in the secondary field
α	Heat transfer coefficient, exponent
β	Coefficient of expansion for gases
ϵ	Compressibility factor, emission ratio

r	Normalized free jet radius
κ	Isentropic exponent
τ	Time constant
ω	Frequency

Indices

/111

a	Exterior
ab	Heat dissipation
grenz	Boundary state
i	Interior
M	Measurement
St	Static
Stau	State at the impact point
Str	Jet
x	State before the compression shock
y	State after the compression shock

/112

9.4 Rotationally symmetric free jet

Coordinates and velocity components in Section 9.4

u	Velocity component in the positive x direction
u'	Turbulent fluctuation velocity in the x direction
v'	Turbulent fluctuation velocity in the y direction
w'	Turbulent fluctuation velocity in the z direction
x	Horizontal coordinate, from the nozzle outlet plane outward in the direction of the jet
y	Horizontal coordinate, from the nozzle outlet plane outward across the direction of the jet
z	Vertical coordinate, from the nozzle outlet plane outward perpendicular to the direction of the jet

9.4.1 Turbulence of the free jet

The thrust jet of a jet engine behind the nozzle opening is a turbulent hot gas free jet with a critical nozzle pressure ratio. Data on its expansion behavior are only rarely to be found in the literature. With turbulent flows, an irregular fluctuation motion is superimposed on the average motion. It also affects the average motion and the transport processes of momentum and heat. Turbulent motions can be treated theoretically only if a physical relation is found between the fluctuation quantities and average motion. According to Ebrahimi [14] a purely theoretical calculation of the turbulent movement is not possible because all known turbulence theories seek to establish a relation between the apparent viscosity forces, given by the time average of the squared fluctuation quantities, and the time average of the velocity.

With his mixing path theory, Prandtl [46] for the first time made possible the analytical treatment of turbulent exchange processes. He proceeded from the fact that in turbulent flow, individual turbulence balls, retaining their initial velocity, move for a certain distance transverse to the main flow direction, the "mixing path", and then mix with the surroundings. As the turbulence balls lead their own existence for a certain period, the turbulence balls would have to exchange / 113 each property connected with the flow, such as temperature and concentration, in the same way. But in a turbulent flow the distribution curves of temperature and velocity do not coincide. As Hinze-Hegge-zijnen [28] have measured, heat expands more rapidly than momentum. Taylor [73] provided an explanation of this with his vortex transport theory. This states that it is not the velocity but the vorticity which is the characteristic property of the turbulence balls. According to Taylor, the exchange magnitude for heat transport is twice as great

as for the momentum. Reichardt [51] developed a similarity theory on the basis of measurements of the momentum and temperature profile, and treated the transport process of turbulent flows independent from special turbulence hypotheses. Reichardt arrived at the result that the momentum of the turbulent free jet is constant over the distance which it runs, because the total longitudinal flow of momentum which moves off transversely is proportional to the longitudinal decrease in momentum.

These older basic works on the expansion of free jets were without exception concerned with the fully expanded region and with jets of low nozzle outlet velocity and excess temperature. But with single cycle turbine engines the exhaust gas jet leaves the nozzle at sonic velocity and high excess temperature, so that we can expect jet expansion differing from that of the incompressible cold gas jet. Laurence [35] has demonstrated that the degree of turbulence decreases with rising Mach number. He measured turbulence spectra with a hot wire in turbulent free jets up to nozzle velocities of Mach 0.7. Corrsin and Uberoi [10] investigated heated free jets and established a higher degree of turbulence with higher temperature. The nozzle Mach number and nozzle temperature are, therefore, decisive parameters for the jet expansion.

As we could find in the literature no systematic documentation about heated free jets with sonic velocity at the nozzle outlet, from which we could determine the sink strength of such jets, extensive basic studies on circular hot gas jets were undertaken at the DFVLR. Circular ring nozzles with a hub body - corresponding to the real engine jets - have not been studied here. The angular momentum of engine jets has also not been considered. According to Higgins-Wainwright [26], however, the angular momentum scarcely affects the breakup of the Mach 1 jet on the jet axis. All free jet investigations have been performed with

critical nozzle pressure ratio. The total temperatures in the nozzle orifice varied between 40°C and 550°C above the ambient temperature. The jet expansion was studied along a length of 30 nozzle diameters.

/ 11+

Knowledge of the turbulent fluctuation velocities is important for an exact evaluation of free jet measurements in order to be able to consider measuring errors of the probes caused by turbulence. No turbulent fluctuation velocities were measured in the heated high velocity free jet as part of these free jet studies, because of the great measuring difficulties. Thus, this work is based on the turbulence spectra measured by Corrsin-Überoi [10], Laurence [35] and others [7, 14, 16, 17, 40].

According to the studies cited, the turbulent fluctuation velocities increase transverse to the jet axis in the direction of the edge of the jet, reaching a maximum in the mixing zone (Figure 56). The turbulence along the jet axis increases strongly behind the nozzle in the jet direction, attains a maximum at $x/D = 7$ to 10, and then decreases gradually. According to measurements by Laurence [35], an increase in the nozzle Mach number causes a decrease in the turbulence (Figure 57), while an increase in the jet temperature increases the turbulence and shifts the turbulence maximum on the jet axis in the direction of the nozzle (Figure 58). (According to measurements of Corrsin and Überoi [10]). According to Bradshaw, Ferries and Johnson [7] the turbulent transverse fluctuations v' and w' are equal to the longitudinal fluctuations u' up to some 3 nozzle diameters behind the nozzle. From there on they become smaller and become about 80% of the longitudinal fluctuations.

9.4.2 Experimental design and measuring technique

In the free jet studies, the hot gas line behind the combustion chamber consisted of a cylindrical tube (80 mm inside diameter and 10 mm wall thickness) 2 m long, made of stainless steel with extremely smooth surface, at the end of which the exchangeable experimental nozzle was mounted so that the free jet blasted horizontally 1,200 mm above the floor. The transition from the hot gas line to the nozzle was flush so that the internal flow was not disturbed. 200 mm ahead of the test nozzle, 4 static pressure holes, 2 mm in diameter, were distributed around the periphery of the cylindrical line and connected together by a ring line. 25 mm in the flow direction behind the plane with the pressure measuring points, two NiCr-Ni thermocouples, 1.6 mm in outside diameter, projected some 30 mm into the tube flow for temperature measurement.

/ 115

The free jets from 5 differently shaped convergent nozzle forms (Figure 51, 52) were studied. Three nozzles had a bell-shaped constriction region connected to a cylindrical outlet with a length of 2, 1, or 0 diameters. A conical nozzle was also used. It corresponds somewhat to the engine nozzles used now, aside from the hub body. There was also a diaphragm with a very short cylindrical outlet among the nozzles studied. The final diameter was 50 mm for all the nozzles. The internal contour lines ended sharply at the nozzle orifice.

The free jet measurements were done with a probe rack which could be moved on the jet axis with a remotely operated moving system (Figure 53). Initially, the impact pressure measurements in the hot gas jet were undertaken with a single movable pitot probe. Because the probe operation was too fast, the measured pressure profiles were always too wide. Because of the high viscosity of hot gases, the build-up time for the pressure in

the measuring line extended from the exact value up to 1 minute. Thus, it appeared desirable to prefer probe racks of movable individual probes for hot gas studies. On the probe rack used, 31 pitot probes and 20 NiCr-Ni thermocouples were distributed along a width of 200 mm (Figure 54). The probe capillaries, of 1.2 mm outside diameter and 0.8 mm inside diameter projected 20 mm free of the 5 mm thick probe holder. The temperature measuring points of the probe rack consisted of 1.6 mm thick NiCr-Ni thermocouples with high-temperature-resistant Inconel jackets with tips welded shut and free globules inside. The total pressures measured at the probe rack were led through 4 m long tubing of 1.6 mm inside diameter through a pressure measuring point selector switch (scanning valve) to a DMS differential pressure transducer with a range of ± 12.5 PSI.

Static pressure measurements were done on the axis of the cold free jet. A cylindrical tube 2 m long and 4 mm thick was used as the static pressure probe (Figure 61). At about the center, 4 static pressure holes were distributed around the periphery of the tube. The tube was movable and mounted in a star-shaped holder inside the hot gas pipeline and fastened to one arm of the probe moving device outside the nozzle. In this way the static pressure measuring point could be moved about 500 mm in the region of the nozzle. This design was preferred to the hook probe because it works almost without oscillation and does not disturb the flow by the compression shock caused by the probe head, because the probe tip was in the low velocity region inside the pipeline far ahead of the nozzle.

/ 116

9.4.3 Calculation of the velocity and temperature from the measurements

The calculation of the local velocities in the region near the speed of sound is quite tedious, and possible only through

repeated iteration. It was done with electronic computers. The Raleigh pitot probe formula (Equation 9.96) was used to test whether supersonic or subsonic velocity was present. From the pitot pressure, the static ambient pressure, and the local isentropic exponent κ a Mach number. If this is smaller than 1, the velocity is calculated according to the laws of compressible subsonic dynamics (Equations 9.91 to 9.95). If the Mach number is greater than 1, then the value of the undisturbed flow before the shock must be determined from the measurements behind the compression shock (Equations 9.96 to 9.99).

In subsonic flow the measured dynamic pressure is

$$q = \frac{\rho}{2} \cdot u^2 \cdot \epsilon \quad (9.91)$$

with the compressibility factor

$$\epsilon = \frac{\kappa-1}{\kappa} \cdot \frac{\left(\frac{p_0}{p_{st}}\right) - 1}{\left(\frac{p_0}{p_{st}}\right)^{\frac{\kappa-1}{\kappa}} - 1} \quad (9.92)$$

The dynamic pressure must already be diminished by Δq - the measuring error due to turbulence, explained in the next section. The density ρ is

$$\rho = \frac{p_{st}}{R \cdot T_{st}} \quad (9.93)$$

The measured temperature is made up of

$$T_M = T_{st} + \frac{u^2}{2 \cdot c_p} \cdot r^* \quad (9.94)$$

in which r^* is the recovery factor of the thermocouple (see Section 9.4.5). After some transformations, we obtain for the velocity:

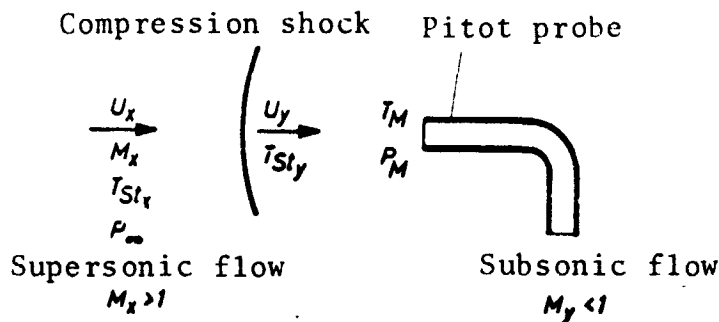
/ 117

$$u^2 = \frac{2 \cdot c_p \cdot T_M \cdot q}{(q \cdot R \cdot r^*) + (p_{st} \cdot \epsilon \cdot c_p)} \quad (9.95)$$

As supersonic velocity, according to Shapiro [67], the Mach number is calculated from

$$\frac{p_M}{p_\infty} = \frac{\left(\frac{\kappa+1}{2} \cdot M_x^2\right)^{\frac{\kappa}{\kappa-1}}}{\left(\frac{2\kappa}{\kappa+1} \cdot M_x^2 - \frac{\kappa-1}{\kappa+1}\right)^{1/(\kappa-1)}} \quad (9.96)$$

where p_M is the measured pitot pressure and p_∞ is the static ambient pressure ahead of the compression shock.



The measured temperature after the compression shock is

$$T_M = T_{c,y} + \frac{u^2}{2 \cdot c_p} \cdot r^* \quad (9.97)$$

Here T_{St_y} is the static temperature of the subsonic region

behind the compression shock. Between the static temperatures T_{St_x} before and T_{St_y} after the compression shock we have

the relation

$$\frac{T_{Sty}}{T_{Stx}} = \frac{(1 + \frac{\kappa-1}{2} M_x^2) \cdot (\frac{2\kappa}{\kappa-1} M_x^2 - 1)}{\frac{(\kappa+1)^2}{2 \cdot (\kappa-1)} \cdot M_x^2} \quad (9.98)$$

Then the supersonic velocity of the undisturbed flow ahead of the / 118 compression shock is

$$u_x = M_x \cdot \sqrt{\kappa \cdot R \cdot T_{Stx}} \quad (9.99)$$

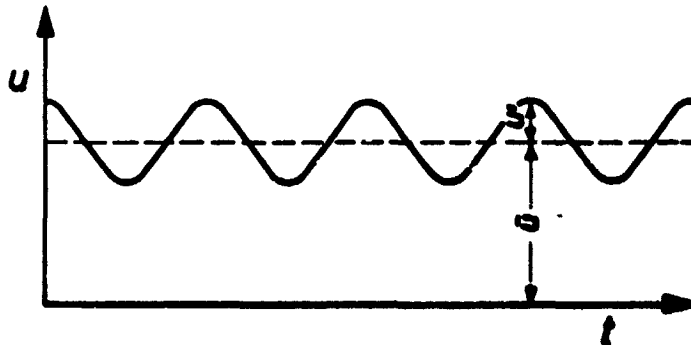
The velocities and temperatures are calculated with the exact c_p and κ values determined for the static temperatures encountered. The gas constant R is always calculated as a function of the air-fuel mixture.

9.4.4 Pitot probe measurement errors due to turbulence

If we use a pitot probe in turbulent flow, an excessively high dynamic pressure is measured. With incompressible flow, the impact pressure measured with the pitot probe is

$$q = \frac{\rho}{2} \cdot u^2$$

where u is the current velocity, made up of the mean of the velocity, \bar{u} , and the instantaneous deviation from the mean, u' .



$$u = \bar{u} + u'$$

$$u^2 = (\bar{u} + u')^2 = \bar{u}^2 + 2\bar{u}u' + u'^2 .$$

If we integrate the velocity over the time, then the expression $2\bar{u}u'$ becomes zero and we obtain

$$\frac{1}{T} \int u^2 dt = \frac{1}{T} \int \bar{u}^2 dt + \frac{1}{T} \int u'^2 dt . \quad / 119$$

If we assume a sinusoidal curve for the fluctuation velocity u' , then

$$u^2 = \bar{u}^2 + \frac{1}{2} u'^2 .$$

The measured impact pressure is then

$$q = \frac{\rho}{2} \cdot (\bar{u}^2 + \frac{1}{2} u'^2) . \quad (9.100)$$

Pitot probes measure a dynamic pressure greater by the value

$$\Delta q = \frac{\rho}{4} \cdot u'^2 \quad (9.101)$$

than the dynamic pressure from the mean velocity. But because the flow has velocity fluctuations about all 3 axes, then

$$\Delta q = \frac{\rho}{4} \cdot (u'^2 + v'^2 + w'^2) . \quad (9.102)$$

It should be noted that in the literature it is usually the effective value \bar{u}' which is given for the turbulent fluctuation velocities. This can be measured with hot wire probes. That is, they are time averages of the turbulent fluctuation velocities. With the effective values, the dynamic pressure measured with pitot probes becomes

$$q = \frac{\rho}{2} \cdot (\overline{u'^2} + \overline{v'^2} + \overline{w'^2}) . \quad (9.103)$$

In the present free jet study, we have used as a basis for the cold gas jet the turbulent fluctuation velocities reported by Laurence [35] for $M_0 = 0.7$. According to this, the degree of turbulence for each measuring point is

$$\tau_u = \frac{\sqrt{1/3(\overline{u'^2} + \overline{v'^2} + \overline{w'^2})}}{\overline{u}} \quad (9.104)$$

and the measuring error of the pitot probe which results from that is calculated.

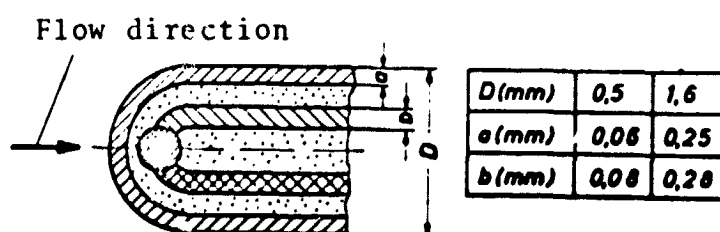
In the hot gas jet, for which there are no turbulence investigations, we have accepted, in the lack of better information, the curve for the turbulent longitudinal fluctuation velocity u' found by Corrsin and Uberoi [10]. There are, however, strong reservations against applying turbulence regularities found at nozzle Mach numbers of $M_0 = 0.07$ and excess temperatures of $\theta_0 = 170^\circ\text{C}$ to nozzle conditions of $M_0 = 1$ and $\theta_0 = 550^\circ\text{C}$. /120

For a free jet with critical nozzle pressure ratio and a nozzle impact pressure of 735 mm Hg, the pitot probe measuring error for a cold jet increases along the jet axis from the value 0 directly behind the nozzle to 16 mm Hg at the axial distance $x/D = 9$. For a jet heated to 550°C it increases to as much as 22 mm Hg (Figure 59). Transverse to the jet axis, the maximum pitot probe measuring error is in the plane $x/d = 6$ behind the nozzle, in the mixing zone at $y/D = 0.5$. For a cold jet it amounts to 24 mm Hg, and for a jet heated to 550°C , 41 mm Hg (Figure 60). With these values, we are not dealing with negligible magnitudes. Therefore, all the experimental results introduced in

this work are corrected by the pitot probe measuring error caused by turbulence.

9.4.5 Systematic error in temperature measurement with thermocouples

The thermocouples used were closed versions of miniature jacketed thermocouples. The two chromel-alumel thermocouple conductors were spot-welded at the measuring point and imbedded in a magnesium oxide (MgO) insulation material, insulated from the jacket. The outer Inconel jacket (NiCrFe alloy) was welded pressure-tight and humidity-tight without changing the outside diameter.



Thermocouples of two different diameters were used. Those 1.6 mm / 121 were used in the jet investigations, and those 0.5 mm thick were used to measure the temperatures in the surrounding field and in the engine intake.

A temperature measurement by these thermocouples is influenced by:

Recovery factor

Heat conduction away from the thermocouple

Radiation of heat

Catalytic effects

Time constant

In the following we shall estimate how great these effects were in the studies.

Recovery factor

Depending on the design of the measuring probe and the state of the flow, the thermocouple may not convert the kinetic energy of the gas completely into thermal energy. The recovery factor indicates the ratio of the actual to the ideal dynamic temperature

$$r^* = \frac{T_M - T_{St}}{T_{ges} - T_{St}} \quad (9.105)$$

The thermocouple does not measure the total temperature T_{ges} of the gas, obtained from the sum of the static and the dynamic temperature, but the somewhat smaller value

$$T_M = T_{St} + \frac{u^2}{2 \cdot c_p} \cdot r^* \quad (9.106)$$

According to Alvermann and Stottman [1], for the thermocouple type used here, with longitudinal incident flow in the Mach number range from 0.1 to 1, the recovery factor is

$$r^* = 0.86 \pm 0.09 .$$

The numerical value 0.84 is used for the evaluation of all experimental data. Calibration measurements showed that this value is accurate to $\pm 2\%$.

The temperature decrease at the thermoelement measuring point due to conduction of heat through the steel jacket and the thermocouple wires into the probe mount is

$$\theta_{ab} = (T_M - T') \frac{1}{\cosh\left(\frac{\alpha_m \cdot U}{\lambda \cdot F} \cdot l\right)} \quad (9.107)$$

Here the abbreviations are:

T_M	temperature measured by the thermocouple
T'	temperature of the thermocouple jacket and wires at the level of the probe mount
α_m	mean heat conductivity coefficient of the thermocouple
λ	thermal conductivity of the jacket material
U	outside circumference of the thermocouple
F	cross-sectional area of the jacket
l	length of the thermocouple from the measuring point to the probe mount

The mean thermal conductivity coefficient, α_m , for the cylindrical body of the thermocouple, with a hemispherical end, with longitudinal incident flow, well between the α -value for a flat plate with longitudinal incident flow and turbulent boundary layer, for which the Nusselt number can be calculated from:

$$\frac{Nu}{Re \cdot Pr} = \frac{0,0297 \cdot Re^{-1/5}}{1 + 0,87 \cdot 1,5 \cdot Pr^{-1/6} \cdot Re^{-1/10} \cdot (Pr - 1)} \quad (9.108)$$

and the thermal conductivity coefficient of a circular tube with transverse incident flow and with a Nusselt number in the

Re range of 1 to 4,000 of

$$Nu = 0.43 + 0.48 \cdot Re^{0.5} \quad (9.109)$$

and for Re numbers of 4,000 to 40,000:

$$Nu = 0.43 + 0.174 \cdot Re^{0.618} \quad (9.110)$$

Alvermann and Stottmann [1] state a Nusselt number for a circular cylinder with longitudinal incident flow:

$$Nu = (0.085 \pm 0.009) \cdot Re^{0.674} \quad (9.111)$$

This is a body shape corresponding to the front spherical cap of the thermocouple used. Between the Nusselt number and the heat transfer coefficient there is the relation: /123

$$\alpha = \frac{Nu \cdot \lambda_{str}}{D} \quad (9.112)$$

Now if we insert the material values prevailing in radiation investigations, we obtain for the hyperbolic cosine of Equation 9.107 a value greater than 10^5 . Then we can establish, without knowing the temperature T' , which is difficult to determine more accurately, that the thermal conduction is negligible and that the error which it causes in the measurement is less than 1°C in any case.

Heat radiation

The thermocouple is in radiation balance with its surroundings. The hot gas jet itself affects the temperature of the thermocouple through the radiation of its CO_2 and H_2O components. The water vapor radiation is so slight, however, that it can be neglected. Using the Stefan-Boltzmann radiation

law, we obtain the temperature loss of the thermocouple due to heat radiation as

$$\Theta_{\text{rad}} = \frac{\epsilon \cdot C_s}{\alpha} \cdot \left(\frac{T_M^4}{100^4} - \frac{T_a^4}{100^4} - \epsilon_{\text{CO}_2} \cdot \frac{T_{\text{Str}}^4}{100^4} \right) \quad (9.113)$$

where it is assumed that the thermocouple has a considerably smaller area than the surroundings radiating back. The symbols in Equation 9.113 are:

- C_s Black body radiation coefficient
- α Heat transfer coefficient at the thermocouple head
- ϵ Emission ratio of steel, in its state during the measurement
- ϵ_{CO_2} Emission ratio of the CO_2 component in the free jet.

From the fuel consumption of the combustion chamber at 500°C jet temperature (0.0074 kg/s) we calculate the CO_2 mass flow after combustion as $\dot{m}_{\text{CO}_2} = 0.023 \text{ kg/s}$. The free jet

consists principally of N_2 , O_2 and CO_2 . The molar proportion of CO_2 can be determined from the molar amount and the molecular weight, giving finally the partial pressure $p_{\text{CO}_2} = 1.7 \cdot 10^{-2} \text{ bar}$

According to Eckert [15], carbon dioxide at this pressure, 500°C temperature, and 30 mm jet radius has an emission ratio of

/124

$$\epsilon_{\text{CO}_2} = 0.02 .$$

This is so small that the last term of Equation 9.113 can be neglected.

The radiation losses for different material values can be taken from the table, with constant values for $\epsilon = 0.6$ and $T_a = 15^\circ\text{C}$.

D	θ_{st}	u	Re	Nu	α	$\theta_{Rad.}$	
mm.	$^{\circ}C$	m/s	-	Accor. to Gl. 9.109 u. 9.110	$\frac{w}{m^2 \text{ deg.}}$	$^{\circ}C$	%
0,5	35	20	162	6,5	340	0,4	1,1
1,6	35	20	520	11,4	186	0,8	2,3
1,6	212	200	$9 \cdot 10^3$	53	1340	1,4	0,7
1,6	512	500	$9 \cdot 10^3$	53	1900	7,3	1,4

The temperature loss due to radiation is decidedly dependent on the heat transfer number α at the head of the thermoelement, but this is very difficult to determine exactly. The local flow conditions are determining for the α -value, so that turbulence increases the heat transfer considerably. As the free jet flow is highly turbulent, the heat transfer to a thermoelement within the free jet will be higher than the heat transfer averaged over a certain length of a plate or a cylinder in longitudinally incident flow with laminar blowing, for which Equations 9.108 and 9.111 apply. For the calculation, then, Equations 9.109 and 9.110 were chosen, because the flow around a circular tube with transverse incidence describes the flow about the thermocouple head well. The high heat transfer in the dead water behind the circular tube, which is also in Equations 9.109 and 9.110, and which cannot occur with the thermocouple because of the presence of the stem, can in this case be evaluated as the additional heat transfer which occurs through the great turbulence of the free jet flow blowing on the thermocouple.

The lowering of the thermocouple probe temperature by radiation varies between 1 and 2% of the measurement. This radiation error is not considered, however, in the evaluation of the experiment.

Catalytic effect

/ 125

As hydrocarbons were used as the fuel for the combustion chamber, there are gas mixtures in the free jet which can carry on exothermic chemical reactions on the surface of the thermocouple if they are released by noble metal catalysts. No such catalytic effects occur, though, with the NiCr-Ni thermocouples with Inconel jackets used here [1].

Time constant

One measure for the response sensitivity of a thermocouple is the thermal time constant τ which indicates the time, after a sudden drop in the temperature, when the thermal potential has dropped to the value $1/e = 36.8\%$ of the initial value.

Temperature drop:

$$\theta_M = \epsilon_{\text{rad}} \cdot e^{-t/\tau} . \quad (9.114)$$

For a sudden temperature rise, the time constant indicates the time after which the thermal potential reaches the value $(1 - 1/e) = 36\%$ of the final value.

Temperature rise:

$$\theta_M = \theta_{\text{rad}} \cdot (1 - e^{-t/\tau}) . \quad (9.115)$$

Neglecting conduction and radiation losses, the time constant is defined as

$$\tau = \frac{\rho \cdot V \cdot c_p}{\alpha \cdot F} \quad (9.116)$$

Here ρ is the density of the thermocouple tip, c_p the specific heat, V the volume, F the surface area, and α the heat transfer coefficient according to Equations 9.109 and 9.110 at the thermocouple tip. The volume of the thermocouple head which comes into question for calculation of the time constant is approximated by a sphere with the diameter of the outer jacket of the thermocouple. For the density and specific heat we must insert averages for the sphere, which consists of the welded bead, the MgO filling, and the Inconel jacket, into Equation 9.116.

With the time constant τ we can define an upper frequency limit

$$\omega_{\text{limit}} = \frac{1}{\tau} \quad (9.117)$$

for the temperature fluctuation, at which the recorded amplitudes of the measurement will amount to only $1/\sqrt{2}$ of the true gas temperature. For turbulent fluctuations above the limiting frequency the measured amplitudes decrease even further. The time constants and upper limiting frequencies of the thermocouples used can be read from the table for different flow conditions. / 126

	D = 0.5 mm			D = 1.6 mm			ρ kg/m ³	c_p Ws/kg deg
	ϕ_i	ϕ_a	V	ϕ_i	ϕ_a	V		
	mm	mm	mm ³	mm	mm	mm ³		
Weld bead	0	0.16	0.00215	0	0.5	0.065	7900	476
Filling MgO	0.16	0.38	0.026	0.5	1.1	0.632	3400	970
Inconel sheath	0.38	0.50	0.036	1.1	1.6	1.45	8000	476

		D = 0.5	D = 1.6 mm		
T	°C	20	20	227	527
u	m/s	5	5	200	500
α	W/m ² deg	340	186	1340	1900
τ	s	0.81	5.3	0.73	0.51
ω_{lim}	1/s	1.2	0.19	1.4	2

The time constant τ increases with decreasing temperature and velocity. That is, the thermocouple follows the temperature fluctuations most poorly at the edge of the jet. Just as the pitot probe, the type of thermocouple used here is unsuitable for measuring the turbulent flow processes at the edge of the jet. Nevertheless these relatively thick thermoelements with protected heads were selected because thinner thermocouples with free welds cannot withstand the mechanical stress of the hot Mach 1 jet and the erosive action of its dirt particles.

A statement of the static pressure is a prerequisite for the exact calculation of free jet velocities. In his basic work on free jet boundaries, Tollmien [74] calculated a static overpressure from the equations of motion for the turbulent free jet. But outside the potential core, experimental free jet studies always yielded underpressures. Still, these early results were little trusted. Even Schlichting [55] in 1930 referred to Tollmien's calculation and considered the underpressures which he had measured in the free jet as measuring errors. Meantime, however, it was confirmed by a series of works, e. g., Miller-Comings [40], Fiedler [17], Eickhoff [16], that the free jet has a static underpressure outside its core. According to Miller and Comings it is equal to the radial component of the apparent turbulent normal force:

$$-\Delta p = \overline{\rho \cdot v'^2} . \quad (9.118)$$

For great density difference we have, according to Eickhoff

$$-\Delta p = \bar{\rho} \cdot \overline{v'^2} + \overline{\rho' v'^2} . \quad (9.119)$$

The course of the static underpressure in the free jet looks similar to the distributions of the turbulent fluctuation velocities shown in Figure 56 and Figure 58. According to measurements of Eickhoff, a certain static overpressure prevails in the core. As early as $x/D = 3.5$ it has changed to an underpressure. At 9 to 10 diameters behind the nozzle, the static pressure reaches its minimum and then increases slowly again. For the transverse distributions of the static pressure in the core region, the pressures fall from positive values on the axis to great underpressures in the center of the mixing zone and then increase again toward the jet edge

to the ambient pressure. In the region of the fully developed free jet the underpressure maximum of the transverse distribution curve moves to the jet axis.

On the basis of the relation of Equation 9.118, the static pressure can be determined by the hot wire method. This avoids the difficulties occurring in the measurement of static pressures by cylindrical probes in turbulent flows. For static pressure measurements in turbulent flows with cylindrical probes, Goldstein [22] established a correction formula. According to Goldstein, the turbulent fluctuation velocities cause a positive / 128 dynamic pressure on the lateral pressure holes of a cylinder as long as the frequency of the turbulent velocity fluctuations transverse to the cylinder axis is higher than a ratio formed from the fluctuation velocities and the probe radius R_s ,

$$\omega > \frac{\sqrt{v'^2 + w'^2}}{R_s} . \quad (9.120)$$

At this turbulence frequency, the probe does not receive any transverse incident flow so that it can form no dead water and underpressure.

For the measured static pressure of a cylindrical probe, Goldstein [22] states the relation

$$P_{StM} = P_{St} + c \cdot \rho \cdot (\overline{u'^2} + \overline{v'^2} + \overline{w'^2}) \quad \text{with } 0 \leq c \leq \frac{1}{3} . \quad (9.121)$$

For the unheated jet, the static pressure curve is measured on the jet axis within the jet and in the free jet out to some 2 diameters behind the nozzle opening. No data on static pressure measurements could be found in the literature. Therefore that of Roscher [53] was expanded and the measuring method with very long cylindrical probe, described in Section 9.4.2, was applied. As the measurement is very strongly affected by the

turbulent fluctuation velocities and these are not known for the high-velocity jet, static pressure measurements succeed only where the turbulence is negligibly small, on the longitudinal axis of the jet in the first section of the potential core. The course of the static pressure measured on the jet axis is plotted in Figure 61 for the five nozzles studied. For all experiments, a nozzle pressure ratio of 1.95 and an excess temperature of $\theta_0 = 40^\circ\text{C}$ were maintained. The high static overpressure in the nozzle orifice of the conical nozzle 4 is striking. It amounts to 30% of the dynamic pressure of the core flow. The assumption often made, that the static pressure for convergent nozzles with critical pressure ratio p_{ges}/p_∞ has decreased to the ambient pressure by the nozzle orifice, must then lead to errors in mass determinations.

At critical nozzle pressure ratio, the velocity in the jet core is above the velocity of sound. Fluctuations of the static pressure, in the region of the first 5 diameters behind the nozzle, have been identified as compression shocks of a supersonic flow by means of Schlieren optics photographs (Figures 62, 63). All the nozzles investigated showed a supersonic flow of Mach 1.02 to 1.04 in the core. Even with exactly critical pressure ratio, a post-expansion to supersonic flow set in behind the nozzle. This can be explained by the sink effect of the jet: In the immediate neighborhood of the nozzle opening, the static pressure of the surroundings is decreased by the contribution of the dynamic pressure to external inflow. This increases the actual nozzle pressure ratio to a supercritical value, and the post-expansion behind the nozzle accelerates the flow to supersonic velocity.

/ 129

For calculation of the free jet velocities from the measured quantities, the static pressure outside the potential core was set equal to the ambient pressure. Because of the lack of data on the turbulence spectrum of the free jet, no statements can be made on the accuracy of static pressure measurements. Only in the forward-most region of the jet core, between the nozzle outlet plane and one nozzle diameter behind the nozzle, were measured static overpressures considered in the velocity calculation.

9.4.7 Axial value

The dynamic pressures and temperatures measured on the free jet axis are plotted in Figures 64 and 65. Here, and in the following, these are always measurements corrected by the Pitot probe measuring error caused by turbulence. The course of the axial velocities calculated from the corrected measurements by Equation 9.95 is plotted in Figures 66 and 67. The varied nozzle temperature is the parameter. The effect of the nozzle Mach number is presented by use of Laurence's results [35], which are also plotted for comparison.

Because of the rise of the degree of turbulence with increasing jet temperature (Figure 58) the hot gas jet mixes more intensely with the surroundings and it breaks up more quickly. Increasing nozzle Mach number has the opposite effect. The degree of turbulence decreases with increasing Mach number (Figure 57). The high-velocity free jet breaks up considerably more slowly than the jet with lower nozzle outlet velocity.

9.4.8 Jet width

110

The half-value radius is a suitable measure of the jet width. This is the distance from the center of the jet to the point at which the dynamic pressure, the temperature, or the velocity has half its axial value. For a Mach 1 free jet, the half value radius of the dynamic pressure and the velocity are nearly independent of the temperature (Figures 68, 72, 73) while the nozzle Mach number has a stronger effect on the jet width. While the Expansion angle for the velocity and the impact pressure in a Mach 1 jet is hardly dependent on the temperature and remains constant for various nozzle temperatures, jets with lower nozzle Mach numbers are wider. In contrast, the temperature expansion of the free jet is dependent on the nozzle Mach number and the nozzle temperature. Low nozzle outlet velocities and high nozzle temperatures produce wider profiles for the temperature distribution (Figures 70, 71).

The results show distinctly that high velocity hot gas jets do not have a greater jet expansion angle than cold gas jets. A trend which is established with free jets having low nozzle Mach number must therefore not also be present with jets of high nozzle Mach number. The decreasing degree of turbulence with increasing Mach number prevents the similarity of the jet expansion laws.

High degrees of turbulence always produce a faster breakup of the jet. But because no turbulence investigations on hot gas jets with high nozzle outlet velocity are yet known, it is impossible to determine the probe measuring error caused by turbulence, to measure exact impact pressure profiles with pitot probes, and to establish from them laws for the expansion of hot gas jets. The turbulence corrections were measured for these measurements by means of the turbulence spectra measured

by Corrsin and Uberoi [10]. Figure 69 shows that consideration of the measurement error due to turbulence leads to smaller jets. Therefore authors who report measurements from free jets with low nozzle outlet velocity, with their still higher degrees of turbulence, establish erroneously large half-value radii if they do not correct the measured dynamic pressures by the turbulence error. (In this respect, see the curves of Reichart, and of Corrsin and Uberoi in Figure 69).

9.4.9 Similarity of the free jet profile

/ 131

Figures 74, 75, and 76 show a plot of dimensionless velocities and temperatures versus the distance from the axis, standardized with the current half-value radius of the velocity or temperature. With increasing distance, x/D , from the nozzle opening, the profiles become flatter. Beyond $x/D = 7$ they take on the same distribution. They are now similar to each other, and one can speak of the fully developed free jet.

The same is true also for the temperature profile. A comparison of the velocity profiles of the cold and heated jets in the region of the developed jet produces only very slight differences in the profile curves in the marginal zone of the jet, which is difficult to cover in measuring technology.

The temperature increase with respect to the isothermal free jet causes no basic change of the expansion laws, because the Gaussian normal distribution

$$\frac{u}{u_{\max}} = e^{-0.69\eta^2} \quad (9.122)$$

given by Reichardt [51] for the velocity curve was confirmed by measurement. Here:

$$\eta = \frac{y}{x} \cdot 0.5 u_{\max}$$

In this diagram, normalized with the half-value radius of the velocity, the temperature distributions are flatter than the velocity profiles. Also, the temperature profiles are now no longer similar. The divergence of the temperature curves from the Corrsin-Uberoi distribution cannot be explained by the higher heating of the DFVLR jet, but rather from the Mach number effect. Increasing nozzle outlet Mach numbers cause smaller jets with smaller half-value radii (Figure 72). In this type of plot, this leads to a broadening of the temperature profile.

9.4.10 Jet edge

A distinct statement of the location of the jet edge is decisive for calculating the volume, mass, and momentum of the free jet. It can be established by measurement only with difficulty, because this is where the turbulence reaches its maximum, due to the low absolute velocities there, making a directional measurement unreasonable. The jet edge cannot be measured even with hot wire probes, because there we are in the range of the inflow, so that the velocity does not vanish. Pitot probes with a longer tubing line and, accordingly, more sluggish pressure indication are best suited to measurement of average values in the turbulent jet edge region. The measurement error caused by turbulence is quite small here because of the low absolute values. In the measurement with the Pitot probe rake, the jet edge is assumed to be where the measured pressure distribution reaches the value of 0. The definition of the jet edge for the hot gas jet is more complicated because of the different width of its pressure and temperature profiles. Here again, for the volume, mass and momentum calculation, the

/132

edge was established where the measured pitot pressure became zero.

The flow-technical phenomena at the jet edge can only difficultly be comprehended for separate velocity and temperature limits. In addition, understanding of the physical process of the input flow becomes difficult. Perhaps, if this highly turbulent region is once studied with suitable measuring methods, it can be shown that the jet edge is not a steady, but a time-variable quantity, and that the velocity and temperature limits of the jet are identical at every instant. But because of the time constant of the temperature transducers, we always measure temperatures more sluggishly and establish wider temperature profiles, while the pressure measurement yields quite good averages.

This difficulty in defining the jet edge becomes quite apparent in considering the jet energy. In the equation for the jet power

$$P = \dot{m} \cdot c_p \cdot \theta + \dot{m} \cdot \frac{u^2}{2} \quad (9.123)$$

The first term represents the thermal energy. It is the predominant portion, so that the heated mass flow must be known as accurately as possible. If one establishes the jet edge where the velocity vanishes, then one cuts off the edges of the temperature profile, even at places where significantly high temperatures are still measured. Now if we define the jet boundary where the temperature has decreased to the ambient value, then one has problems in determining the mass flow between this point and the velocity profile zero point.

Calculations of the jet power always gave a physically unreasonable rise in the value of the thermal portion of

Equation 9.123 with the jet path length. This indicates that the thermocouples, with the existing temperature fluctuations, always measured values which were too high for the desired averages. This error has a particularly strong effect at the edges of the temperature profile, and incorrectly moves this outward. For the volume, mass and momentum calculations in particular, the exact knowledge of the physical quantities in the outer jet edge zone plays an important role, because quantities occurring there must be considered more strongly, because of the relatively greater cross-sectional area, than those from the area of the center of the jet.

Therefore, we must state here that the volume, mass, and momentum curves calculated here for the hot gas jet still contain a certain possible error in case the temperature profile measured within the impact pressure jet limits proves to be erroneous.

9.4.11 Volume, mass and momentum flow

To calculate the volume flow

$$\dot{V} = \int_0^{2\pi} \int_0^R u(r) \cdot r \cdot dr \cdot d\varphi \quad (9.124)$$

the mass flow

$$\dot{m} = \int_0^{2\pi} \int_0^R \rho \cdot u(r) \cdot r \cdot dr \cdot d\varphi \quad (9.125)$$

and the momentum flow

$$\dot{I} = \int_0^{2\pi} \int_0^R \rho \cdot u(r) \cdot r \cdot dr \cdot d\varphi. \quad (9.126)$$

In a certain cross-sectional plane of the free jet, the density and velocity were determined for each measuring point on the probe rack. From those, a partial volume, a partial mass, or a partial momentum were determined. Their sums, out to the jet edge, where the velocity disappeared, yielded the total volume, total mass flow, or total momentum in a cross-sectional plane.

Figure 78 shows the volume flow across the jet axis, calculated from the measurements. Behind the core region, the volume increase proceeds linearly. Here again it becomes clear, by comparison with the curve reported by Liem [38] for the low velocity jet, that the Mach 1 jet mixes less with the surroundings because of its lower degree of turbulence. The very slow volume increase of the hot free jet can be explained by means of the decrease in velocity due to the faster drop in temperature of the hot jet.

/134

Figure 79 shows that the increase in the mass flow of the hot gas jet in the initial region behind the nozzle, which is of interest for VTOL technology, differs considerably from that of the cold gas jet. While the cold jet scarcely increases in mass in the region from 3 to 6 nozzle diameters, it is in just this region that the hot gas jet draws in the greatest mass of secondary air. At $x/D = 6$ the mass flow of the cold gas jet is only 1.3 times the mass at the nozzle, while the hot gas jet at this point has already enlarged to 1.8 nozzle masses. In this initial region the hot gas jet sucks in almost three times as much mass as the cold jet. Up to $x/D = 25$, the hot gas jet has

the greater mass. From there on the nozzle temperature no longer has any effect on the mass increase of the free jet and the mass flow curves of the cold and hot jets coincide on the line

$$\frac{\dot{m}}{\dot{m}_0} = 0.412 + 0.144 \cdot \frac{x}{D} ; \quad \frac{x}{L} \geq 25 . \quad (9.127)$$

The momentum flow curves (Figure 80) make it clear that for the high velocity cold gas jet, the momentum of the jet also is maintained after an initial loss in the core region. In contrast, the hot gas continues to lose momentum even after the core region.

9.4.12 Inflow velocity

The jet inflow velocity, normalized to the nozzle outlet velocity, is plotted in Figure 9. This is the velocity component of the surrounding air perpendicular to the jet axis at the jet edge at $u = 0$ (Figure 73). The inflow velocity can be calculated from the mass growth of the free jet. Due to the non-steady mass increase of the Mach 1 jet immediately behind the nozzle, the inflow velocity reaches its maximum one diameter behind the nozzle for the cold gas jet, and 3.5 diameters behind the nozzle for the hot gas jet. Because of the slow mass increase of the cold gas jet in the core region, the inflow velocity in this section almost completely vanishes after some 2 diameters. Behind the core region, we establish an equally decreasing distribution of the inflow velocities for the cold and hot jets. By comparing these results with those from Liem [38] for the incompressible cold gas jet, it can be shown quite well how much lower the inflow velocity of the high velocity jet is than that of the free jet with lower nozzle outlet velocity. Because of its lower degree of turbulence, the Mach 1 jet affects the state / 135

the surroundings significantly less than does the low-velocity jet, which enters into much greater interaction with the surrounding medium.

The magnitudes of the inflow velocities depend on the size of the model. These statements can be demonstrated with a crude approximation, in which the existing temperature differences need not be considered. For the inflow velocity we have

$$w = \frac{\Delta \dot{V}}{\Delta F_{\text{rad}}} .$$

$\Delta \dot{V}$ is the growth in volume in the jet section of length Δl , having the exterior surface ΔF_{str} and an average diameter D_{str} .

$$w \sim \frac{V_o}{\Delta F_{\text{rad}}} = \frac{u_o \cdot F_o}{\pi \cdot \Delta l \cdot D_{\text{rad}}} .$$

D_{str} and Δl can be expressed as multiples of the nozzle diameter D :

$$w \sim u_o \cdot \frac{\pi/4 \cdot D^2}{\pi \cdot D \cdot D} .$$

The only dimension, D , cancels out completely.

The function $\frac{w}{u_o} = f(x/D)$ is, therefore, valid for all model sizes.

As the inflow velocities are used as boundary conditions for the potential theory calculation, it is reasonable to express the measured curves in Figure 9 as a closed expression. The function of the normalized inflow velocities for the first jet section behind the nozzle is described by a compensating polynomial, which has been determined according to Gauss for the cold gas jet and has been determined by the Tschebyscheff method for the hot gas jet.

For nozzle distances above 6 D the inflow velocity can be expressed by a linear equation.

Cold gas jet

/ 136

Range of x/D : 0 to 6:

$$\frac{w}{u_0} = -8.052 \cdot 10^{-3} + 6.972 \cdot 10^{-2} \cdot \left(\frac{x}{D}\right) - 6.170 \cdot 10^{-2} \cdot \left(\frac{x}{D}\right)^2 + 2.104 \cdot 10^{-2} \cdot \left(\frac{x}{D}\right)^3 - 3.153 \cdot 10^{-3} \cdot \left(\frac{x}{D}\right)^4 + 1.749 \cdot 10^{-4} \cdot \left(\frac{x}{D}\right)^5 \quad (9.128)$$

Range of x/D : 6 to 30:

$$\frac{w}{u_0} = -2.2 \cdot 10^{-4} \cdot \left(\frac{x}{D}\right) + 34 \cdot 10^{-4} \quad (9.129)$$

Hot gas jet

Range of x/D : 0 to 6:

$$\frac{w}{u_0} = -1.483 \cdot 10^{-3} + 5.501 \cdot 10^{-3} \cdot \left(\frac{x}{D}\right) - 7.969 \cdot 10^{-4} \cdot \left(\frac{x}{D}\right)^2 \quad (9.130)$$

Range of x/D : 6 to 30:

$$\frac{w}{u_0} = -1.2 \cdot 10^{-4} \cdot \left(\frac{x}{D}\right) + 42 \cdot 10^{-4} \quad (9.131)$$

9.4.13 Effect of the nozzle shape

No effect of the nozzle shape on the free jet expansion could be detected with the five convergent nozzles studied. Divergences in the measurement of the axial values or the half-value radii can be explained by random variation of the measurements. No systematic variation of the measurements dependent on the nozzle shape can be detected. The free jet with a critical nozzle pressure ratio is distinguished less by its history in the nozzle than the subsonic jet. The laminar supersonic velocity of the core and the thin nozzle boundary layer with its low degree of turbulence due to the high velocity are only insignificant information carriers. The effect of the nozzle shape on the free jet expansion will be stronger for the jet with lower nozzle velocity.

9.5 Rotationally Symmetric Wall Jet

/143

Coordinates and velocity components in Section 9.5:

u	Radial velocity component
w	Wind velocity above the ground boundary layer (at 3 m height)
w'	Wind velocity at the height of the maximum wall jet velocity
w_1	Wind velocity at 1 m height
w_2	Wind velocity at the height z
z	Vertical coordinate, perpendicular to the ground

The hot exhaust gas jet from the lift engine strikes the ground, where it is diverted into the wall jet, which expands radially to all sides (Figure 81). The wall jet increases in mass through turbulent mixing of surrounding air, and its velocity

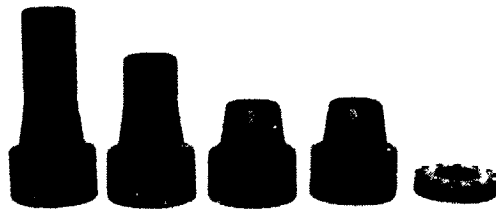


Figure 51. The five examined free jet nozzles, $D = 50$ mm.

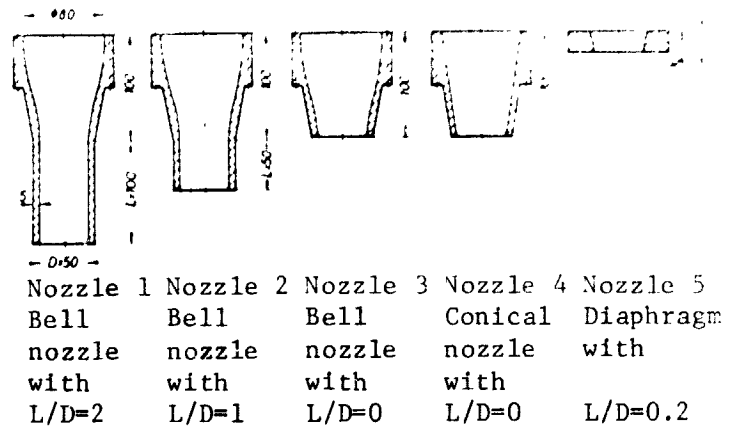


Figure 52. Sectional drawing of the five free jet nozzles.

Figure 53. Probe rake in the hot gas free jet



Figure 54. Free jet probe rake.

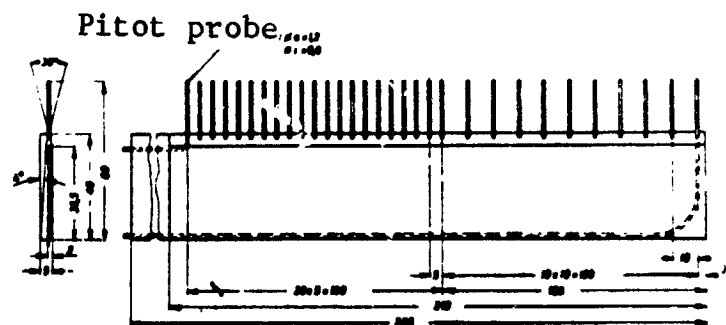
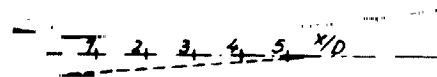


Figure 55. Light section photograph of the free jet.
 $M_0 = 1$.



/ 138

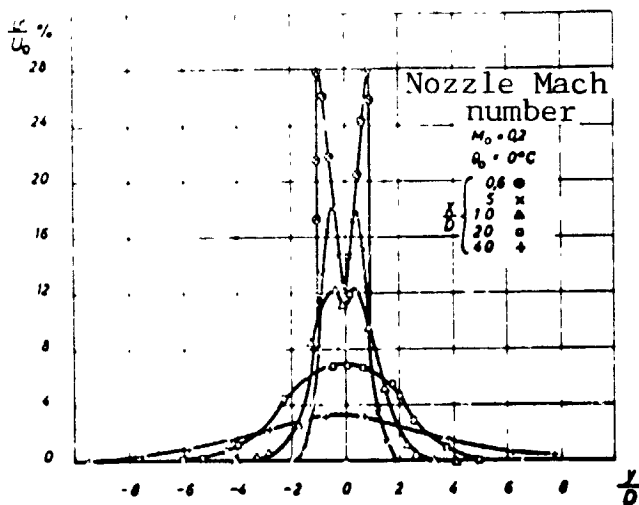


Figure 56. Distribution of the turbulent fluctuation velocity in the free jet, according to measurements by Corrsin and Uberoi [10] and Laurence [35].

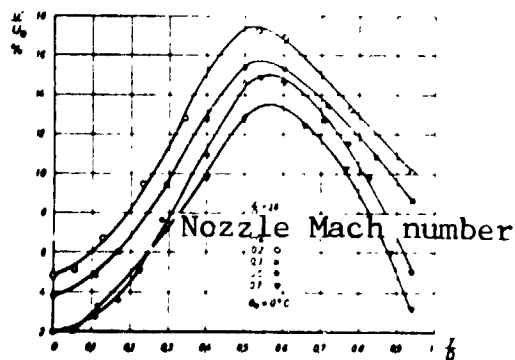


Figure 57. Turbulent fluctuation velocities of the free jet as functions of the nozzle Mach number, according to measurements by Laurence [35].

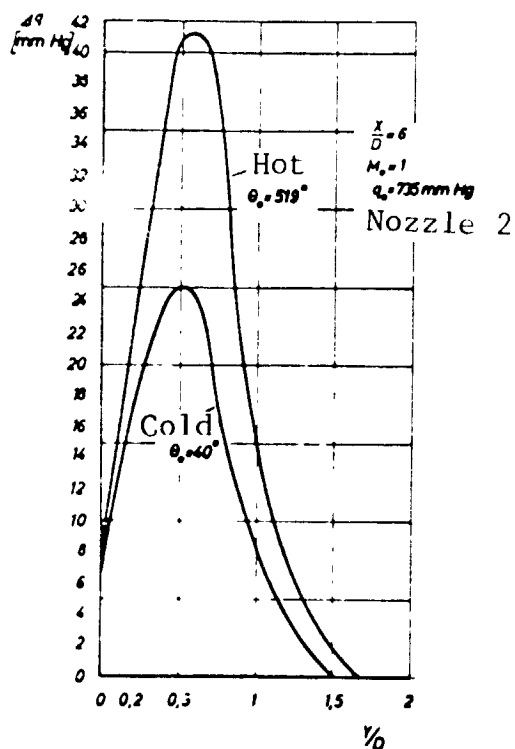


Figure 60. Pitot probe measurement error caused by turbulence transverse to the jet axis.

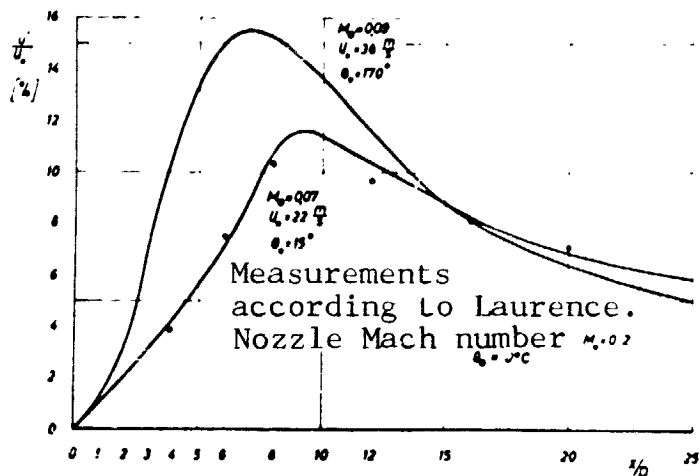


Figure 58. Turbulent fluctuation velocities of the free jet as functions of the nozzle temperature, according to measurements by Corrsin and Uberoi [10].

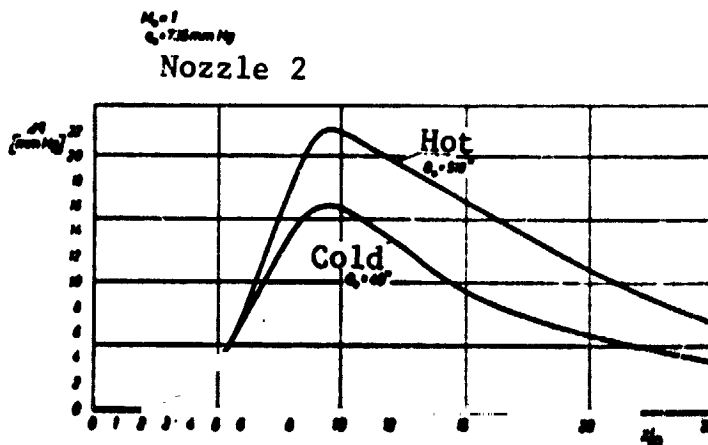


Figure 59. Pitot probe measurement error caused by turbulence along the jet axis.

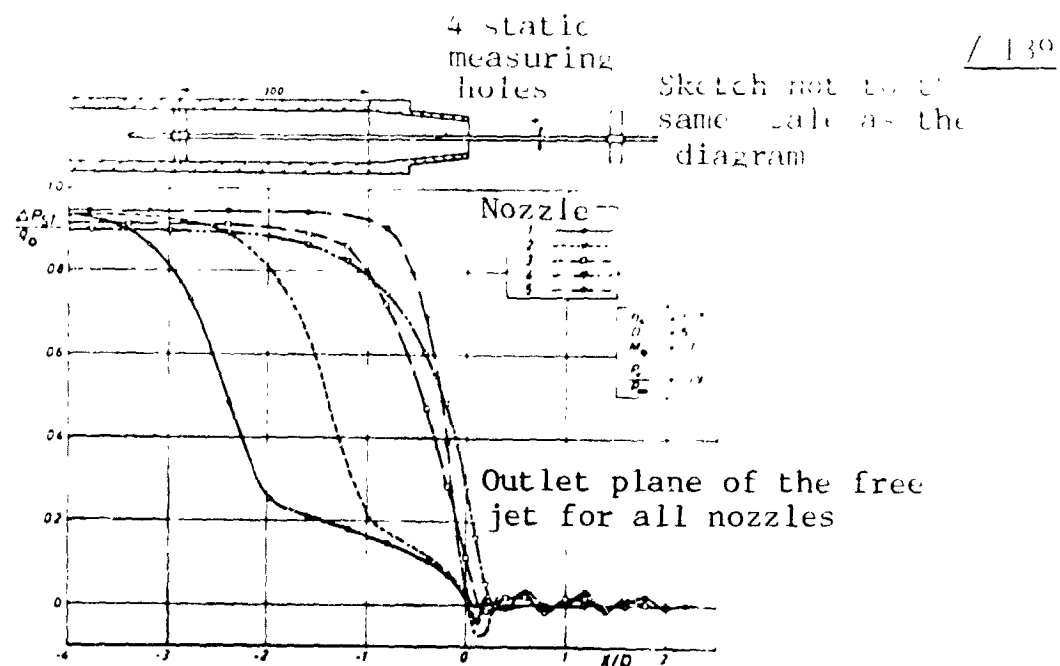


Figure 61. Static pressure curve along the longitudinal axis of the jet.

Figure 62. Schlieren picture of the free jet directly behind the nozzle, nozzle pressure ratio 1.9.

Figure 63. Schlieren picture of the free jet, nozzle pressure ratio 2.2.

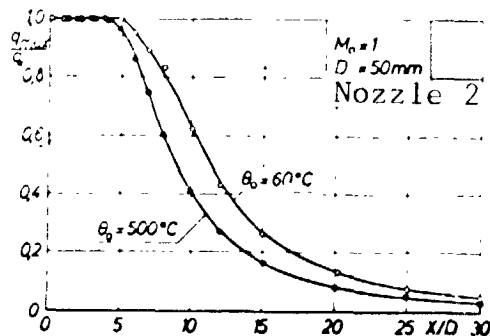


Figure 64. Dynamic pressure along the longitudinal axis of the jet, temperature effect.

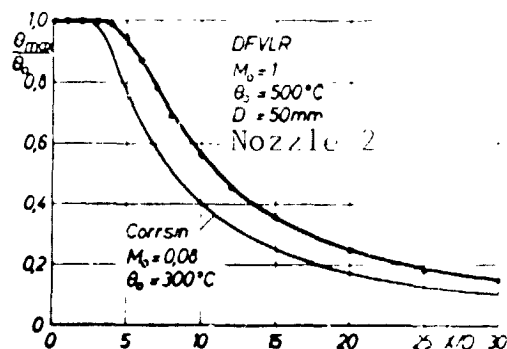


Figure 65. Total temperatures on the longitudinal axis of the jet, Mach number effect.

/ 140

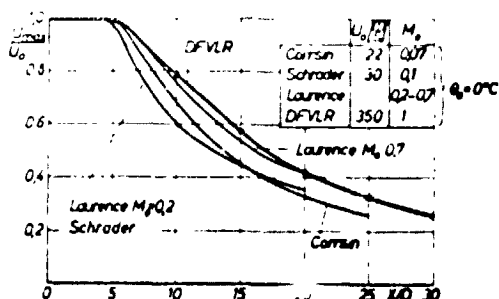


Figure 66. Velocities along the longitudinal axis of the jet, Mach number effect.

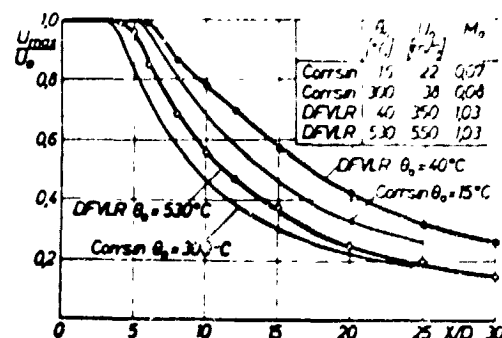


Figure 67. Velocities along the longitudinal axis of the jet, temperature and Mach number effect.

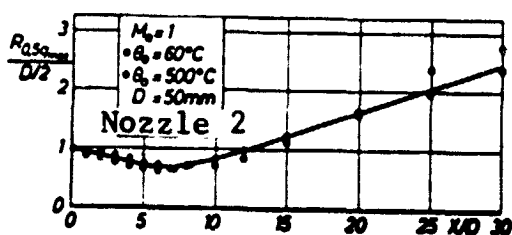


Figure 68. Half-value radius of the dynamic pressure, temperature effect.

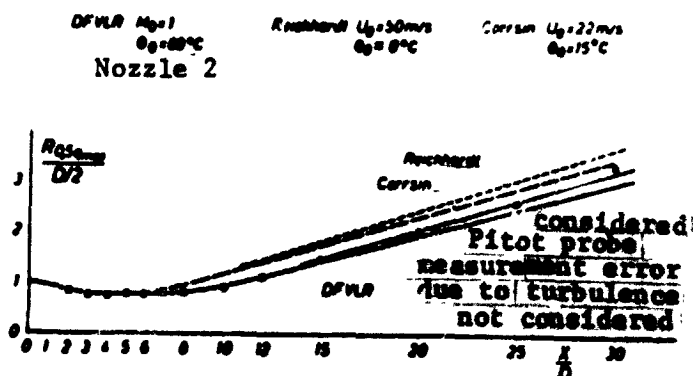


Figure 69. Half-value radius of the dynamic pressure, effect of measurement error from turbulence.

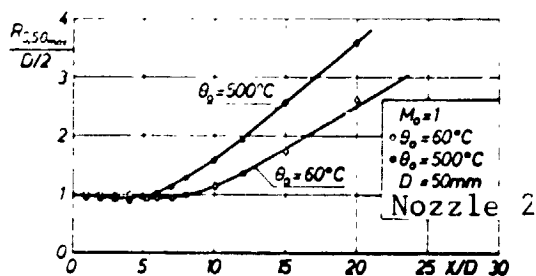


Figure 70. Half-value radius of the total temperature, temperature effect.

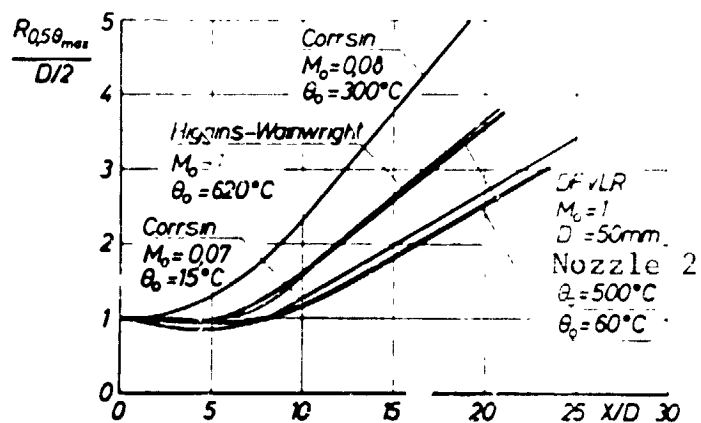


Figure 71. Half-value radius of the total temperature, temperature and Mach number effect.

/ 141

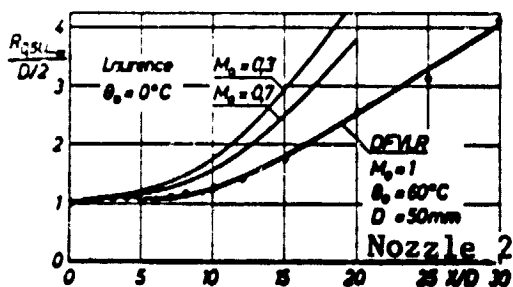


Figure 72. Half-value radius of the velocity, Mach number effect.

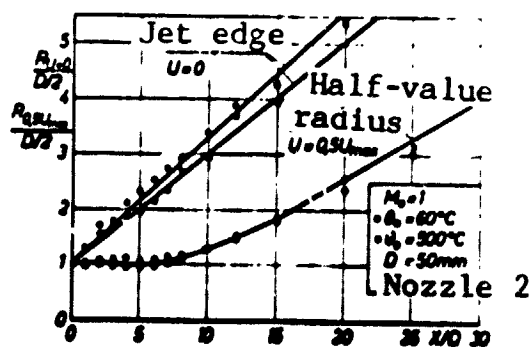


Figure 73. Half-value radius of the velocity and jet edge, temperature effect.

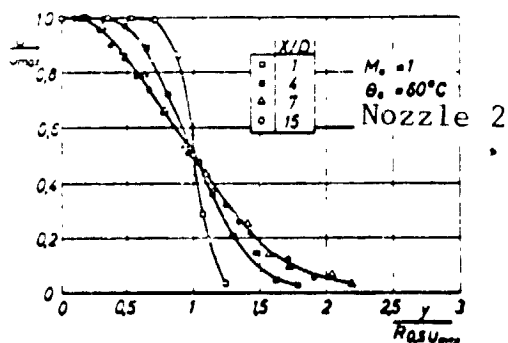


Figure 74. Normalized velocity profile, cold gas jet.

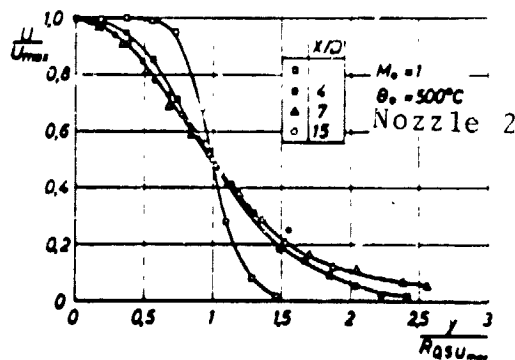


Figure 75. Normalized velocity profile, hot gas jet.

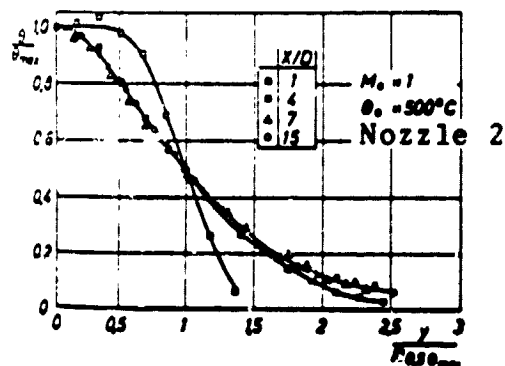


Figure 76. Normalized total temperature profile, referred to the half-value radius for the temperature.

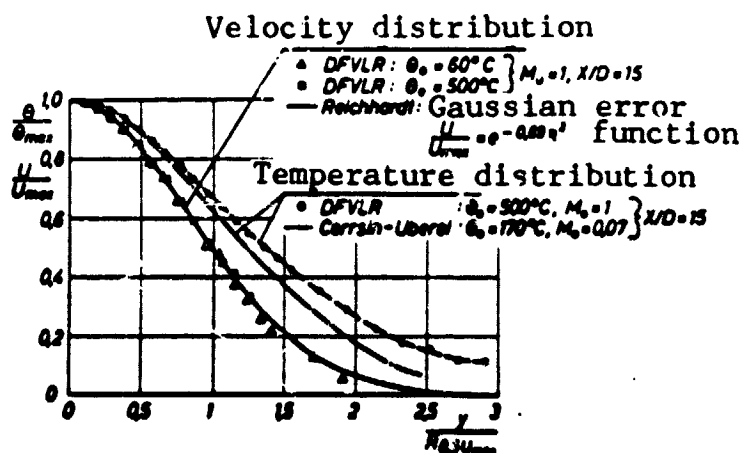


Figure 77. Normalized velocity and temperature profiles, referred to the half-value radius for the velocity.

Figure 78. Increase in volume flow, temperature and Mach number effect.

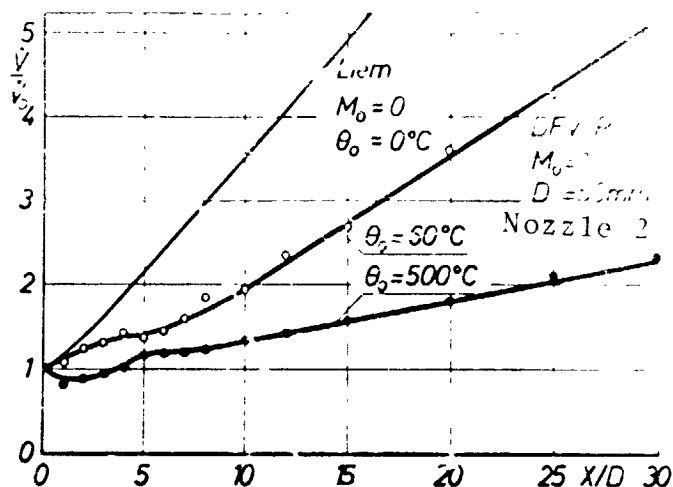


Figure 79. Increase in mass flow, temperature and Mach number effect.

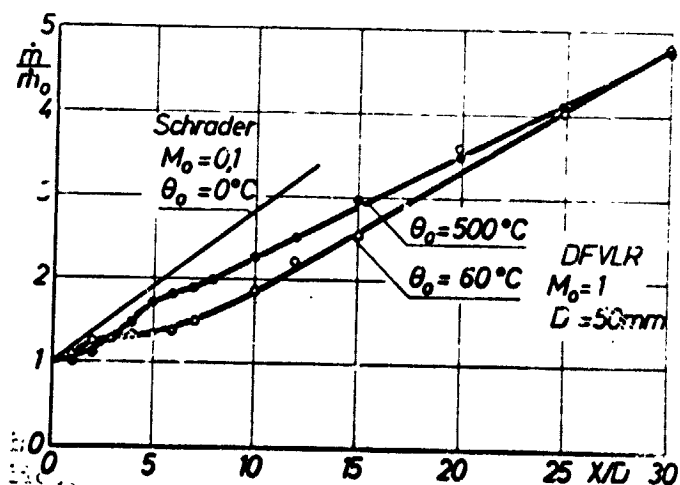
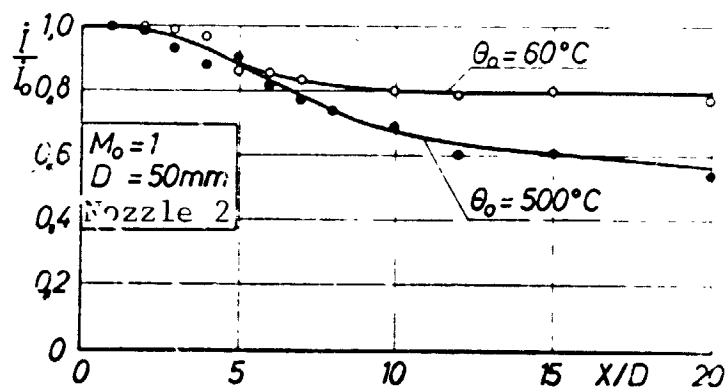


Figure 80. Total
momentum flow,
temperature effect.



and temperature decrease. The static underpressure, which must be present, as for the fully developed free jet, allows the hot wall jet to stick to the ground in opposition to the thermal buoyant force at the ground (Coanda effect). According to [60], only very isolated works on hot gas wall jets have yet been published, as, for example, those of Cox and Abbott [11], Hall and Rogers [24], Higgins, Kelly and Wainwright [27]. These, however, contain no data about the mass increase of the wall jet, which is important for the recirculation calculation. Almost all the basic studies on wall jets are concerned with unheated sub-critical jets. But the exhaust gas jet from the single cycle lift engine strikes the ground with sonic velocity and high excess temperature, producing a wall jet expansion which is different from that of the cold low-velocity jet.

9.5.1 Experimental design and measuring technique

The investigations of the hot gas wall jet on the ground effect test system were done with the jet striking the ground vertically. Measurement of the dynamic pressure in the nozzle plane gave a satisfactory rectangular profile (Figure 85) and allowed us to expect a rotationally symmetric wall jet. A nozzle pressure ratio, P_{ges}/P_{∞} , of 1.95 was maintained in all tests. This is approximately what appears for a single cycle lift engine and corresponds to a nozzle Mach number of 1. The total temperature at the nozzle orifice was either 60°C, 500°C, or 1,000°C above the ambient temperature. The distance between nozzle and ground was varied between 2 and 10 nozzle diameters. The measurements in the wall jet were done at radial distances of 3 to 20 nozzle diameters from the wall jet impact point. / 144

In the wall jet measurements, the hot gas pipeline behind the combustion chamber consisted of a steel tube 1 m long and 113 mm inside diameter. The test nozzle was mounted at the end of the tube

with the opening downward (Figure 82). The nozzle diameter decreased from 80 mm to a final diameter of 50 mm. The nozzle has a cylindrical outlet of 50 mm (Nozzle 2). Immediately ahead of the right-angle deflection of the flow, four static pressure holes of 2 mm diameter were distributed about the periphery of the pipeline. They were connected by a ring line. In the plane of the pressure measuring points, one NiCr-Ni thermocouple of 4 mm outside diameter projected 50 mm into the tube flow.

As the nozzle pressure ratio was critical, the right-angle deflection of the flow immediately ahead of the nozzle did not produce any disturbing asymmetry in the nozzle outlet profile. Measurement of the dynamic pressure in the nozzle plane gave a satisfactory rectangular profile, and allowed us to expect a rotationally symmetric wall jet. The wall jet was studied on a platform with an area of 12 m^2 . Its distance from the nozzle could be adjusted hydraulically. One great problem was the choice of a suitable material for the platform surface. On one hand, it should be similar to the concrete floor at the natural VTOL takeoff site. On the other hand, the material would have to withstand for a long time the enormous erosive action exerted by a jet at sonic velocity and heated up to $1,000^\circ \text{C}$. After many experiments, the best material turned out to be concrete plates 25 mm thick with a 20 mm thick heat shield of Promabest (silica-asbestos). It was used for all the experiments. After about 30 minutes blast time the Promabest coatings were always changed. The roughness of the platform surface was less than 0.3 mm.

The wall jet measurements were done with a probe rake which could be moved by means of a remotely operated moving device which moved on rails at the side of the platform. After checking the rotational symmetry of the wall jet, measurements were made with the probe rake only in a plane perpendicular to the tube axis. Along the 268 mm length of the probe rake were distributed

20 pitot probes of V2A steel, with 1.6 mm outside diameter and 1.1 mm inside diameter, and 20 thermocouples (Figure 83). The temperature measuring points of the probe rake consisted of 1.6 mm thick NiCr-Ni thermocouples with high-temperature-resistant Inconel jackets, with tips welded closed and with the weld bead lying free inside. The total pressures measured by the probe rake were lead through 4 mm long tubing lines of 1.6 mm inside diameter through a pressure measuring point selector (scanning valve) to a DMS differential pressure transducer with a range of ± 2.5 PSI. / 145

In the unheated wall jet, static pressures were measured with pressure holes in the floor plates (Figure 84). In order to do this, a steel plate, polished flat, 50 x 300 mm in size, was inset into one Eternite plate. The steel plate contained 94 pressure holes, each 0.8 mm in diameter. As the static differential pressure of the wall jet at some distance from the wall jet is very small, the pressure values, sampled by two scanning valves, were not electronically measured and recorded, but switched to a Prandtl manometer, where they were read to an accuracy of 1/20 mm water column.

9.5.2 Ground pressures

Static pressure measurements in the wall jet were not done in these studies; only the distribution of the ground pressures over the wall jet radius was determined (Figure 86). From the high dynamic pressure values in the center of the jet impact point, the measured pressure decreases with increasing radius. Beyond radii of 8 nozzle diameters it maintains values between 0.5 and 1.5 mm water. Underpressures could not be detected, in spite of the greatest care in the production of the static pressure holes in the floor plate. No doubt this measured overpressure is caused by the high degree of turbulence in the wall jet. This type of measurement allows us to say nothing about the static pressure of

the wall jet immediately above the floor. More suitable methods for measuring the static pressure distribution in the wall jet were reserved. The dependence of the static pressure on the height (pressure profile) was of particular interest.

9.5.3 Turbulence

/ 146

In the dynamic pressure measurements, the strong variations of the pitot pressure were striking. At $R/D = 10$ they could amount to 15% of the measured value, and up to 40% at $R/D = 20$. In the measurements, a digital voltmeter always averaged the applied value over a period of 20 ms. Even when the integration time of the digital voltmeter was changed to 80 ms, the impact pressure variations did not change. Therefore, they are below 12.5 Hz. The light section photographs (Figures 55 and 81) show distinctly that the edge of the wall jet is much more fragmented than that of the free jet. The turbulent fluctuation velocities of the wall jet are, then, on the order of magnitude of the illumination period, while the smooth outside surface of the free jet allows us to conclude that its turbulent fluctuation frequencies are very high. This conjecture is confirmed by Hall and Rogers [24], who published a spectral density distribution of the wall jet, showing the same frequency for the turbulent fluctuations in the range between 100 and 1 Hz. As the turbulent fluctuation velocities of the wall jet, according to the same authors, are 30% of the local velocity at the ground and up to 50% of the local velocity in the boundary layer with the surroundings, it is not reasonable to undertake dynamic pressure measurements in wall jets with rapidly sampling digital data collection systems which work in the millisecond range. Measurement and integration times of about 1 second, such as the U-tube manometer with long tubing lines has, lead to better results. Here the dynamic pressures are not evaluated directly with the measured values, but with values improved by a compensation curve.

As the Pitot tube nearest the wall lies directly on the floor, there is an error in the measurement because of the velocity gradient at the wall. With measurements at a wall distance of less than 2 probe diameters, the measured velocity is too low. According to Wuest [78], a correction of 1.6% should be added to the measured velocity in this case.

The dynamic pressure and temperature of the wall jet were always measured together, so that the local velocity may be calculated according to the laws of compressible subsonic aerodynamics, with the static pressure of the wall jet set equal to the ambient pressure.

9.5.4 Similarity of the profiles and wall jet breakup / 147

An investigation of the mutual similarity of the wall jet profiles was performed at the radius $R/D = 20$, which was far behind the starting zone, and therefore in the range of the fully developed wall jet. If we plot the dimensionless temperatures versus the distance from the ground, normalized with the half-value height, then the distribution is the same for all the nozzle temperatures and distances from the nozzle to the ground which were studied (Figures 89, 90). In the dimensionless velocity plot the temperature effect produces no deviation from the Glauert normal profile [21], although the change of the distance of the nozzle from the ground does (Figures 87, 88).

If we compare the measured dynamic pressure profiles with each other at a certain radius in the wall jet for various nozzle distances H/D , then we establish, surprisingly, that the maximum dynamic pressures increase with increasing ground distance up to $H/D = 8$ (Figure 91). Although the distance covered from the jet to the measuring point at $R/D = 5$ for a nozzle distance from the ground of $3D$ is almost half as far as when

the nozzle distance from the ground is 10 D, the maximum dynamic pressure for the greater nozzle distance is 24% greater than for the shorter distance. This "reversal effect" cannot be detected in the temperature profiles. At the same measuring point, short nozzle distances here cause higher temperatures (Figure 92). Now if we plot the curve of the maximum impact pressures and velocities versus the radius, the "reversal effect" can be shown clearly. The maximum dynamic pressures and velocities increase with larger nozzle distance up to $H/D = 8$ (Figures 93, 95, 97, 99, 100). If we increase the distance of the nozzle from the ground farther to 10 D, the dynamic pressure and velocity curves remain constant, as reported by Cox and Abbott [11] and Hölscher and Jünke [30]. An explanation for the decrease of the wall jet velocity as the nozzle approaches the ground must be sought in the free jet expansion. If the laminar core flow of the free jet strikes the ground, then the deflection to a wall jet will be linked with greater losses in momentum than on impact of a later region of the free jet with its fully turbulent flow. As the cross-sectional area of the core becomes a larger portion of the total cross-sectional area of the free jet where it strikes the ground, the loss in the deflection becomes greater and the normalized velocity profiles of the wall jets are no longer affinitive. Only when the free jet strikes the ground with its fully developed region are the profiles of the wall jet velocity similar to each other.

As in the free jet, the dynamic pressure and the velocity of the wall jet decrease more rapidly at higher nozzle temperatures (Figures 93, 101). An effect of the nozzle temperature change cannot be detected at the maximum temperatures in the wall jet (Figure 95). Only the distance from the nozzle to the ground is noteworthy. The measurements are distributed on two curves: if the free jet core reaches the ground, as is the case for distances $H/D > 5$, the wall jet temperatures are on the upper

/ 148

curve and are higher than the temperatures at the larger nozzle distances of $H/D = 6$ to 10 . The momentum losses in the deflection of the supersonic core become apparent as a temperature increase in the wall jet.

The parameters with the greatest effect are clearly outstanding on a double-log plot of dynamic pressure, temperature and velocity (Figures 94, 96, and 98). The distance of the nozzle from the ground is the characteristic influencing quantity for the gas-dynamic state of the wall jet.

9.5.5 Half-value heights

The half-value height, $h_{0.5}$, has been selected as a measure for the wall jet height. This is the distance from the ground at which the local dynamic pressure, the local temperature, or the local velocity reaches half its maximum value. It appears from Figures 102, 103 and 104 that, as in the free jet with a critical nozzle pressure ratio, so too in the wall jet, the spatial expansion is independent of the temperature. The half-value heights of the measured dynamic pressure, temperature, and velocity profiles fall together on a straight line for all nozzle temperatures and nozzle distances. The variation in the measurements is caused by the low-frequency turbulent fluctuations, but there is a distinct frequency maximum on the solid lines. Because of the variation of the measurements we cannot establish unambiguously whether greater distances of the nozzle from the ground produce slightly thicker wall jets, as reported by Hrycak, Lee, Gauntner and Livingood [31] and by Hölscher and Jünke [30], who have studied supersonic jets. The measurements of these authors are included in Figure 104 for comparison. From this we can see that the wall jet expansion proceeds quite analogously to the free jet expansion. The subcritical jet with its lower velocity has a higher degree of turbulence than the Mach 1 jet

and, therefore, produces a wider jet which breaks up more quickly.

9.5.6 Volume, mass, and momentum flow

/ 149

For each measuring point of the probe rack, the density and velocity were determined. From these, a partial volume or a partial mass were determined, in order to calculate the volume flow

$$\dot{V} = 2\pi R \int_0^h u \cdot dz \quad (9.132)$$

and the mass flow

$$\dot{m} = 2\pi R \int_0^h \rho \cdot u \cdot dz \quad (9.133)$$

of the wall jet at a certain radius from the jet impact point. The sum of the partial quantities out to the jet edge, where the velocity disappears, yields the local total volume flow or the total mass flow of the wall jet. The volume flow and the mass flow are plotted in Figures 105 and 107 versus the radius, for different H/D values and temperatures. The increase is linear and strongly dependent on the nozzle height and the temperature. The high-loss jet deflection at short nozzle distances also decreases the volume and mass increase of the wall jet. It is striking that the values for H/D = 2 are always above those for H/D = 3. An increase in the temperature causes a faster breakup of the jet and, therefore, a stronger intermixing of surrounding air. The results of Skifstad are included for comparison (Figure 106). He established mass balanced for sub-critical jet studies by other authors. We can see that these

values must be higher than those of the Mach 1 jet. Because of the greater turbulence of the slower jet, it breaks up faster, with greater half-value heights and faster mixing with the surroundings.

The nozzle temperature and the nozzle distance from the ground exert a very strong effect on the mass increase of the wall jet. If we normalize the mass flow of the wall jet, not with the mass flow \dot{m}_0 at the nozzle outlet, but with the mass of the free jet at its point of impact on the ground, \dot{m}_{Stau} , which can be taken from Figure 79, then at ground distances $H/D > 5$ all mass increase curves for various temperatures and H/D values can be described by the straight line

$$\frac{\dot{m}}{\dot{m}_{\text{Stau}}} = 0.4 \cdot \frac{R}{D} \quad (9.134)$$

Figure 108 shows the curve of the momentum flow

/ 150

$$\dot{I} = 2\pi R \int_0^h \rho \cdot u^2 \cdot dz \quad (9.135)$$

calculated from the measured pressure and temperature profiles for various radii, nozzle heights and nozzle temperatures, versus the wall jet radius. Here we determine a partial momentum from the density and velocity at each measuring point of the probe rack, summing them to obtain, finally, the local total momentum flow.

As expected, the momentum flow of the wall jet is practically independent of the radius. Like that of the free jet, it is the same for all measuring cross sections. With decreasing nozzle

distance from the ground, the momentum flow of the wall jet also decreases. At $H/D = 10$ it is 62%, and at $H/D = 3$ only 45% of the initial momentum at the nozzle. The low wall jet momentum appears if the core of the free jet strikes the ground. The momentum flow of the wall jet decreases as the proportion of the core cross section to the total cross section at the point of impact increases. Figure 108 shows that the deflection losses from the free jet to the wall jet, which are expressed as a drop in the wall jet momentum flow, no longer change as the nozzle distances increase beyond 8 D. The momentum and velocity curves at 10 D distance are identical with those from 8 D. The nozzle temperature has no effect on the momentum curve. The distance of the nozzle from the ground is the determining parameter.

The static pressure of the wall jet increases in the vicinity of the jet impact point, but pressure measurements cannot be made there because of measuring difficulties. Thus the calculation of the momentum flow is based on the static ambient pressure. This simplification, however, leads to the drop in the calculated momentum flow at small wall jet radii shown in Figure 108; but the range of influence of the deflection region can be explained with just this drop in the momentum curve. The effect of the impact area does not extend, as Gauntner, Livingood and Hrycak [31], out to a wall jet radius of 3 nozzle diameters. Rather, for a Mach 1 jet, it extends out to $R/D = 10$, as the momentum curves clearly show.

Likewise, the deviation of the velocity curve from a straight line in the double-log plot of Figure 98 is a result of the drop in velocity with approach to the impact point or an erroneous calculation of the velocity due to a rise in the static pressure of the wall jet in this region. The velocity curves also indicate an effect of the impact region out to $R/D = 10$. / 151

9.5.7 Inflow velocity

The inflow velocity for the wall jet calculated from the mass increase is plotted in Figure 10. It decreases as the radius increases or the surface area grows. The nozzle distance is an important parameter for the inflow velocity, as it is for the mass flow. Larger distances of the nozzle from the ground allow a wall jet with higher momentum, which draws in larger amounts of surrounding air, these flowing in faster in agreement with the continuity equation. A comparison with the inflow velocity reported by Liem [38] gives good agreement for the unheated jet at large distances between ground and nozzle. Low nozzle heights generate less turbulent wall jets which interact less with the surroundings.

As for the free jet, the inflow velocities of the wall jet are independent of the model geometry. For the mean inflow velocity out to the radius R we can write

$$w = \frac{\Delta \dot{V}}{F_{\text{rad}}}$$

where $\Delta \dot{V}$ is the volume sucked in over the circular area F_{str} . If we express these quantities as multiples of the nozzle diameter D and the wall jet radius R ,

$$w \sim \frac{v_o}{F_{\text{rad}}} = \frac{u_o \cdot F_o}{\pi \cdot R^2}$$

$$w \sim u_o \cdot \frac{\pi/4 \cdot D^2}{\pi \cdot R^2} .$$

But the ratio D/R deals with the most important similarity parameter, which is always held constant for the model and the full-scale design, so that the inflow velocity is independent of the model size.

Compensation functions have been determined for the measured inflow velocities of the wall jet (Figure 10) by the method of least squared errors. The general function for the sink distribution in the range of $R/D = 3.5$ to 20 is: / 15

$$\frac{w}{u_0} = a_0 + \frac{a_1}{(R/D)} + \frac{a_2}{(R/D)^2} + \frac{a_3}{(R/D)^3} \quad (9.136)$$

where the coefficients for the various configurations can be taken from the table.

H/D	θ_0 °C	a_0	a_1	a_2	a_3
3	60	$+1.337 \cdot 10^{-4}$	$+4.016 \cdot 10^{-2}$	$+3.417 \cdot 10^{-1}$	-1.018
	600	$+2.017 \cdot 10^{-3}$	$-1.416 \cdot 10^{-2}$	$+3.763 \cdot 10^{-1}$	$-7.319 \cdot 10^{-1}$
	1000	$+3.309 \cdot 10^{-4}$	$+2.101 \cdot 10^{-2}$	$+6.728 \cdot 10^{-2}$	$-8.995 \cdot 10^{-2}$
8	60	$+2.630 \cdot 10^{-3}$	$-2.324 \cdot 10^{-2}$	+1.069	-2.586
	500	$+6.685 \cdot 10^{-4}$	$+2.335 \cdot 10^{-2}$	$+2.135 \cdot 10^{-1}$	$-4.258 \cdot 10^{-1}$
	1000	$-1.842 \cdot 10^{-3}$	$+7.280 \cdot 10^{-2}$	$-2.701 \cdot 10^{-1}$	$+7.166 \cdot 10^{-1}$

The coefficients for functions of the inflow velocities of configurations not measured can also be determined by interpolation between the table values.

9.5.8 Separation of the wall jet from the ground by the effect of the wind

When the VTOL exhaust gas jet strikes the ground, it expands radially to all sides as a wall jet. Because of its buoyancy, the attempt of the warm gas jet to separate from the ground, an underpressure develops at the underside of the wall jet, according to Cox and Abbott [11]. Where the ratio of the underpressure to the local maximum dynamic pressure exceeds a certain value, the wall jet separates from the ground. For the hot gas jet, Cox and Abbott define a model parameter, which they derive from the Grashof number:

$$Gr = \frac{l^3 \cdot g \cdot \beta \cdot \theta \cdot \rho}{\mu^2} = \frac{u \cdot \rho \cdot l}{\mu} \cdot \frac{l^3 \cdot g \cdot \beta \cdot \theta \cdot \rho}{\frac{u \cdot l^3 \cdot \mu}{1}} \quad (9.137)$$

With the buoyant force per unit volume

$$A = \beta \cdot g \cdot \rho \cdot \theta \quad (9.138)$$

and the shear stress per unit area (viscosity)

/ 153

$$\tau = \frac{\mu \cdot u}{l} \quad (9.139)$$

we can write:

$$Gr = Re \cdot \frac{\text{Buoyant force}}{\text{Viscous force}} \quad (9.140)$$

Now Cox and Abbott select the ratio

$$\frac{\text{Buoyant force}}{\text{Kinetic force}} = \frac{\frac{l^3 \cdot g \cdot \beta \cdot \theta \cdot \rho}{\rho \cdot u^2 \cdot l^2}}{\frac{1}{u^2}} \sim \frac{l \cdot g \cdot \beta \cdot \theta}{u^2} \quad (9.141)$$

multiplied by the temperature ratio as the characteristic parameter for the warm wall jet

$$\frac{u^2}{\beta \cdot g \cdot \theta \cdot D} \left(\frac{T_a}{T_c} \right)^n$$

For the thermal separation radius of the heated wall jet without a wind effect, Cox and Abbott semiempirically determined the relation

$$\frac{R}{D} = 0.62 \left[\frac{u_o^2}{\beta \cdot g \cdot \theta_o \cdot D} \cdot \left(\frac{T_a}{T_o} \right)^{1/2} \right]^{1/2} \quad (9.142)$$

If a wind flow blows against the wall jet, then the gas jet separates from the ground even before reaching this thermal separation radius. According to Cox and Abbott, it separates where the ratio of the wind velocity to the maximum local wall jet velocity exceeds the critical ratio

$$\frac{w}{u_{\max}} = 0.39 \quad (9.143)$$

We have performed experiments to test this statement on the separation radius under the effect of wind, which is very important for recirculation calculations. Purely thermal separations of the heated wall jet were not investigated, because of the experimental difficulties in the measurement of large separation lengths and their minor practical significance.

The length which the wall jets run against wind flows was measured with a constant nozzle diameter of 50 mm for different nozzle Mach numbers, nozzle temperatures, and distances of the nozzle from the ground. A blower produced a wind flow against the wall jet (Figure 109). Three different wind velocities could

/154

be established. Their curves are plotted on their symmetry line in Figure 110. The gradient of the wind velocity in the direction it ran was small, so that it did not falsify the experimental results. Great care was taken to simulate a realistic wind profile. The velocity profile of the wind in the boundary layer near the ground can generally be described with an exponential relation:

$$w_z = w_1 \cdot z^\alpha \quad (9.144)$$

The exponent α depends on the height. In meteorology, however, it is usually set constant and equal to 0.3 for the ground friction layer. The wind profile, measured at many points over the plate, is shown in Figure 111. In figure 112 the true velocity profile of the wind near the ground is compared with the profile used in the experiments ($w_0 = 8 \text{ m/s}$). The agreement between the two profiles in the area of the wall jet is very good. Only at greater heights above the plate did the velocity profile of the blower jet drop off in comparison to the true wind profile. This difference in the profiles is allowable because it occurs in an area which exerts no effect on the wall jet flow and its separation from the ground. The separation lengths were recorded photographically with the light section method, in which the wall jet flow was colored with the contrast powder (Figure 113, 114). The separation radius was defined as the maximum radial length of run for the wall jet, which could be detected on the light section photograph as a boundary between the white-colored jet and the uncolored, dark wind.

Figure 117 shows the separation radii versus the wind velocity at $H/D = 8$ and critical nozzle velocity for different nozzle temperatures. The wind velocity data in the diagrams are meant to be the maximum velocity of the profiles being investigated. As the wind velocity increases, the separation radius decreases linearly. No effect of the nozzle temperature on the location of

the separation point is detectable at wind velocities above 7 m/s. The nozzle Mach number, in contrast, plays a great part with respect to the separation radius. As the nozzle pressure ratio decreases, the jet momentum decreases and, with it, the distance which the expanding wall jet runs against the wind (Figure 118). /155

The strong dependence of the nozzle distance from the ground on the separation length of the wall jet is striking. The low wall jet momentum at low H/D values also leads to shorter separation lengths when the wind is blowing. The separation radius at $H/D = 3$ and that for $H/D = 8$ are compared in Figure 119.

The horizontal course of the separation line for $H/D = 3$ can be seen in Figures 115 and 116. These figures were obtained with a horizontal light section 50 mm above the ground. The separation line takes on an elliptical shape, with the minor semiaxis corresponding to the separation radius. Here the very irregular separation line is conspicuous. This is due to the low-frequency fluctuations of the separation radius. All the magnitudes for the separation radius given here are means of several individual measurements. Their variation often amounted to as much as 10%.

If we compare these results with those of Cox and Abbott [11] (Figure 113), we establish that their very short separation radii for the wall jet under the influence of wind must be due to the small, not reported, jet Mach number in their experiments. According to Figure 118, decreasing Mach numbers allow the separation radii to contract. Nozzle Mach numbers below 0.5 could lead to the measurements of Cox and Abbott. The critical velocity ratio used by Cox and Abbott, which leads to separation of the wall jet, proves not to be a universal constant for all experiments by any means. It appears that the value is strongly dependent on the jet Mach number and the height of the nozzle above the ground.

For $H/D = 3$ the values scatter:

$$\frac{w}{u_{\max}} = 0.62 - 0.71 \quad (9.145)$$

$$\frac{w'}{u_{\max}} = 0.38 - 0.48 . \quad (9.146)$$

For $H/D = 8$ we obtain fixed critical values:

$$\frac{w}{u_{\max}} = 0.79 \quad (9.147)$$

$$\frac{w'}{u_{\max}} = 0.54 . \quad (9.148)$$

Here w is the wind velocity over the boundary layer near the ground. In the experiments it was the maximum value of the wind profile. w' is the velocity of the wind profile at the height of the maximum wall jet velocity u_{\max} .

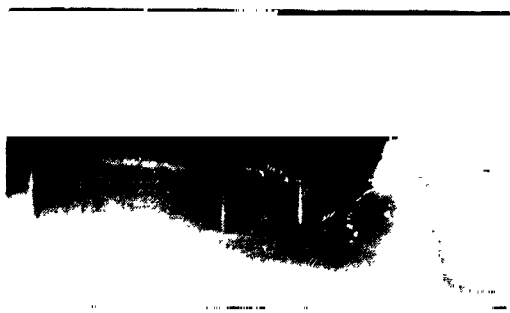


Figure 81. Light section photograph of the wall jet.



Figure 82. Probe rake in the hot gas jet.

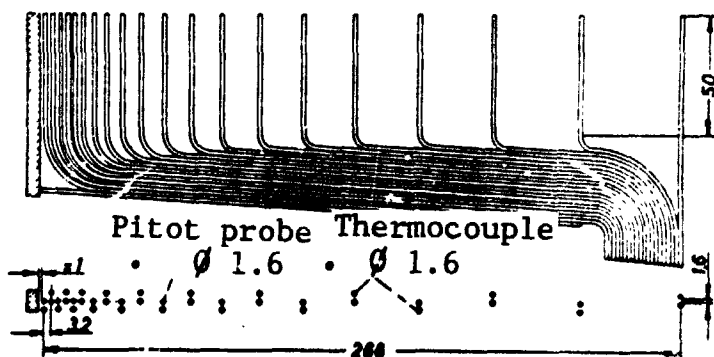


Figure 83. Wall jet probe rack.

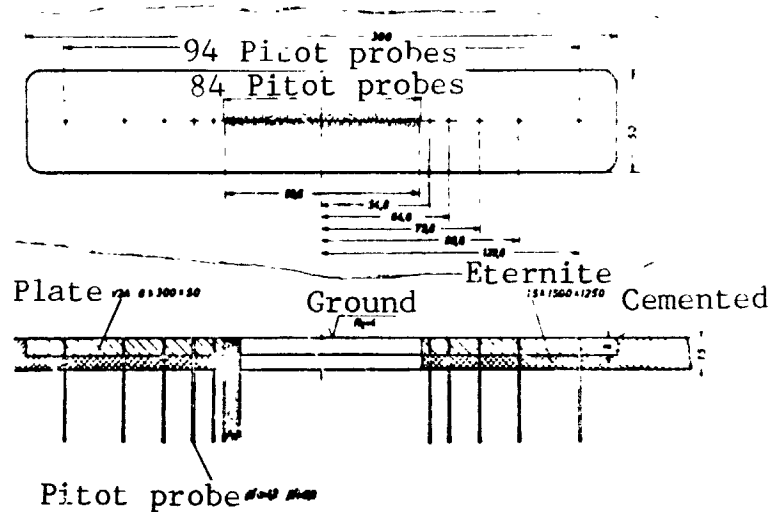


Figure 84. Measuring point arrangement for the ground pressure study.

/ 157

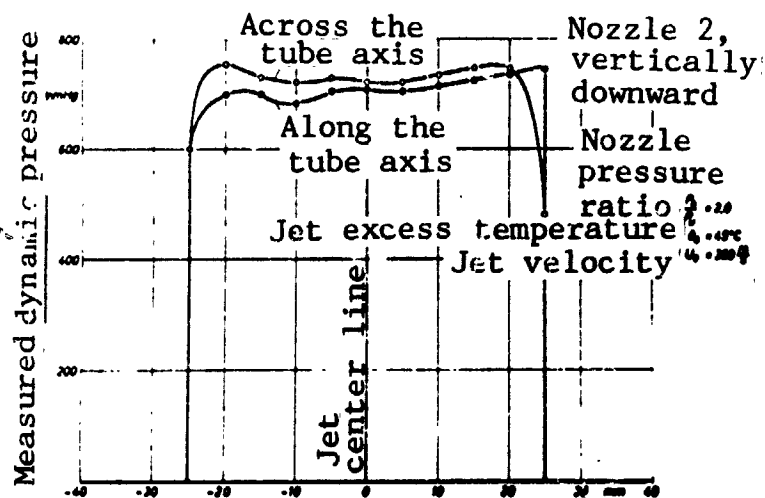


Figure 85. Dynamic pressure profile in the nozzle outlet plane of Model 1.

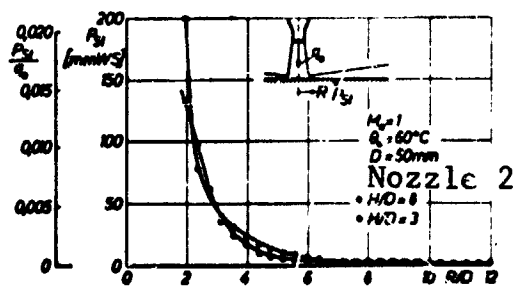


Figure 86. Ground pressure distribution, H/D effect.

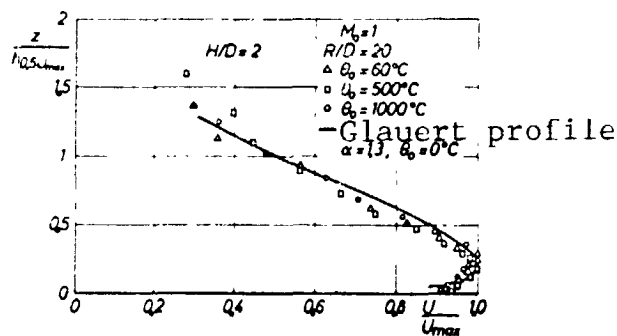


Figure 87. Normalized velocity profile, $H/D = 2$.

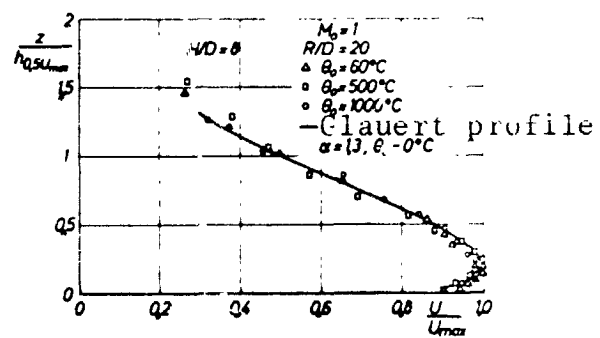


Figure 88. Normalized velocity profile, $H/D = 8$.

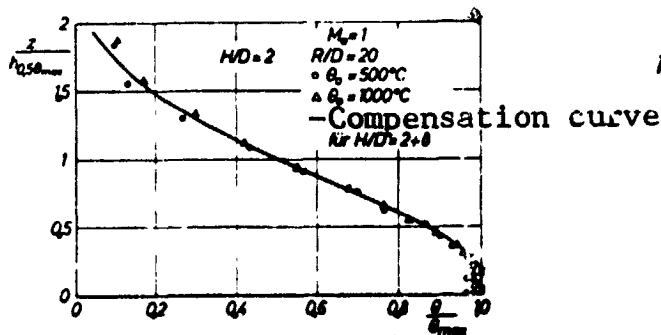


Figure 89. Normalized total temperature profile, referred to the half-value height for the temperature, $H/D = 2$.

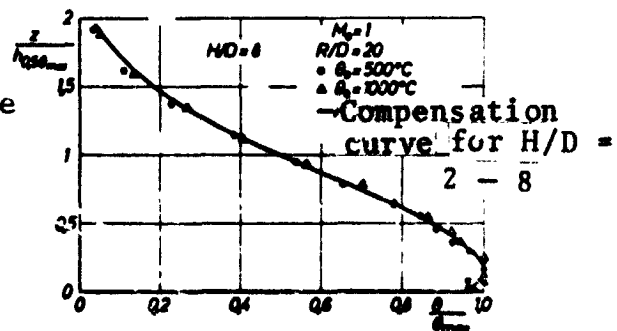


Figure 90. Normalized total temperature profile, referred to the half-value height for the temperature, $H/D = 8$.

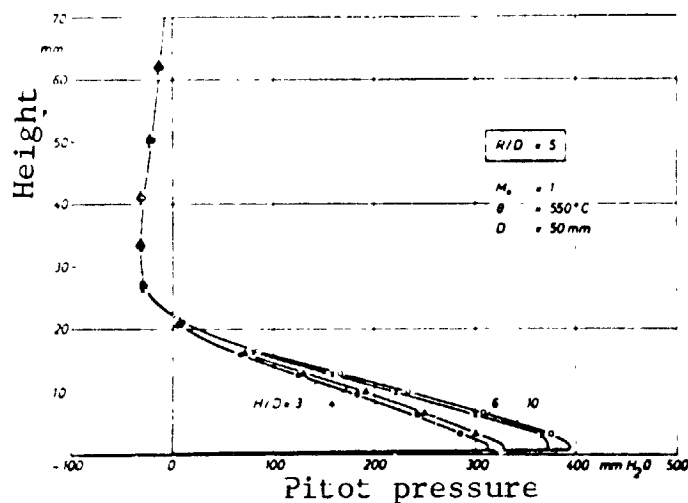


Figure 91. Pressure profile of the wall jet, effect of the nozzle distance H/D .

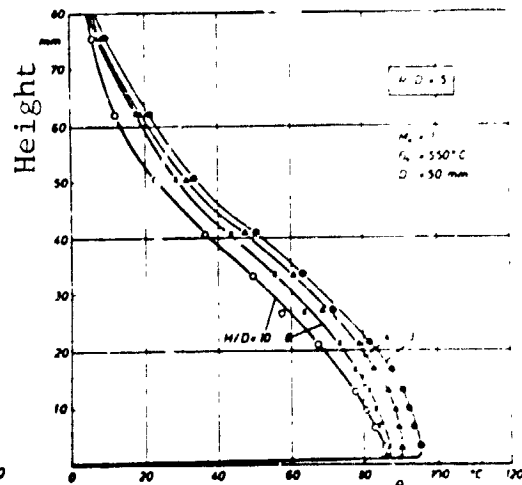


Figure 92. Temperature profile of the wall jet, effect of the nozzle distance H/D .

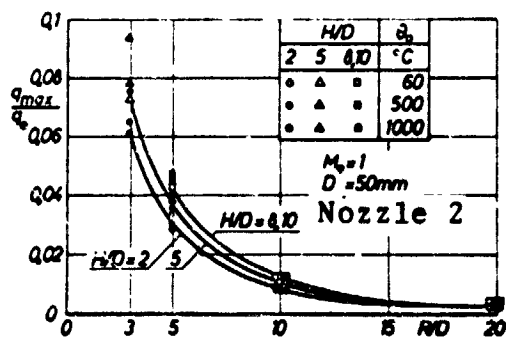


Figure 93. Distribution of the maximum dynamic pressure, temperature and H/D effect.

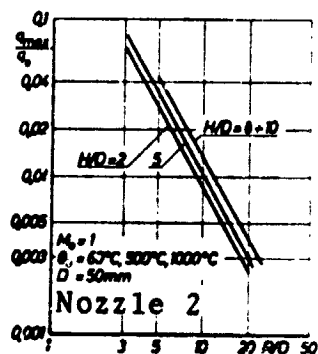


Figure 94. Distribution of the maximum dynamic pressure, temperature and H/D effects.

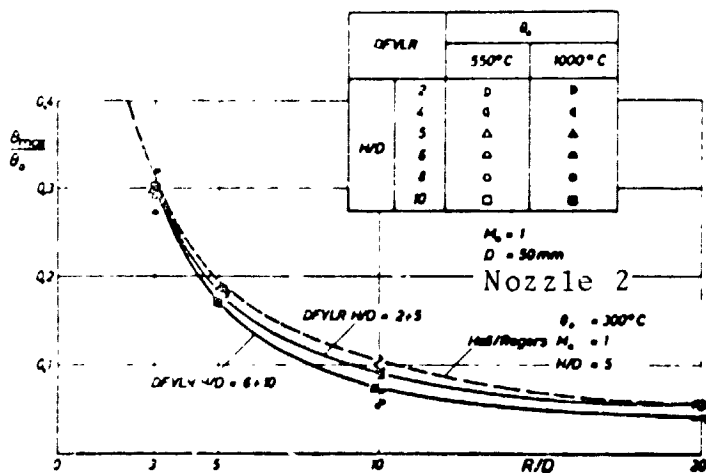


Figure 95. Distribution of the maximum temperatures. Temperature and H/D effects.

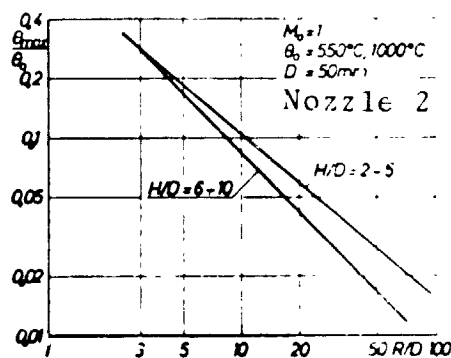


Figure 96. Distribution of the maximum temperatures. Temperature and H/D effects.

/ 159

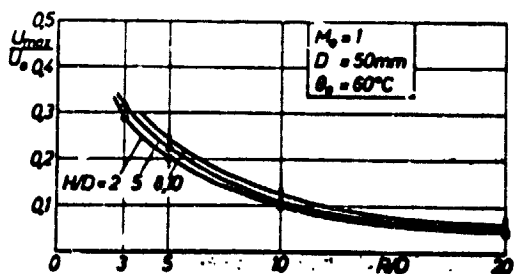


Figure 97. Distribution of the maximum velocities, H/D effect, $\theta_0 = 60^\circ \text{C}$.

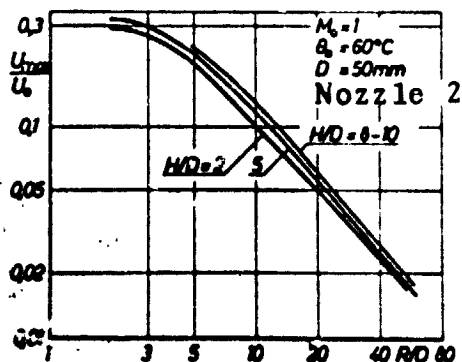


Figure 98. Distribution of the maximum velocities, H/D effect, $\theta_0 = 60^\circ \text{C}$.

Figure 99. Distribution of the maximum velocities, H/D effect, $\theta_0 = 500^\circ\text{C}$.

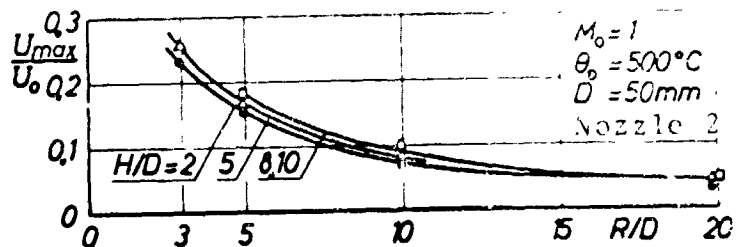


Figure 100. Distribution of the maximum velocities, H/D effect, $\theta_0 = 1,000^\circ\text{C}$.

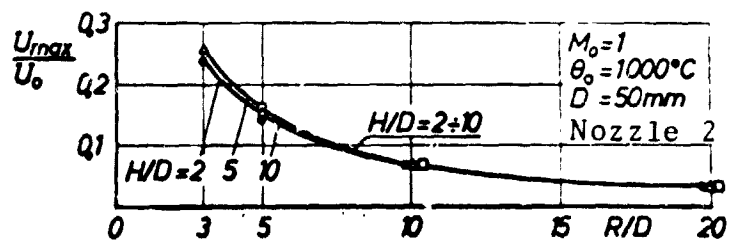


Figure 101. Distribution of the maximum velocities, temperature effect.

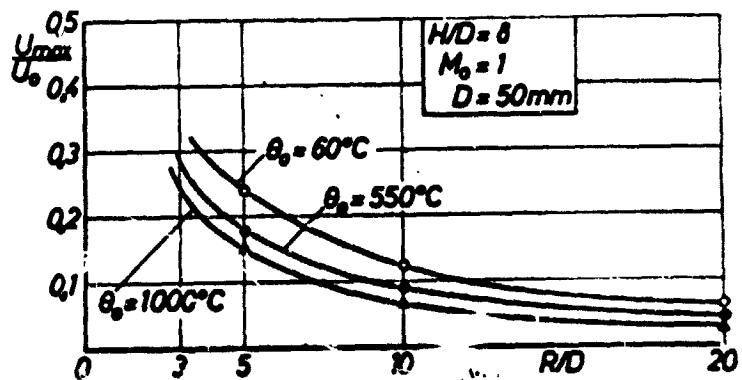


Figure 102. Half-value height of the dynamic pressure.

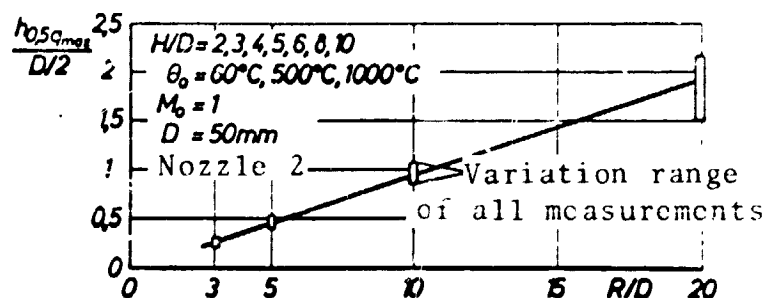
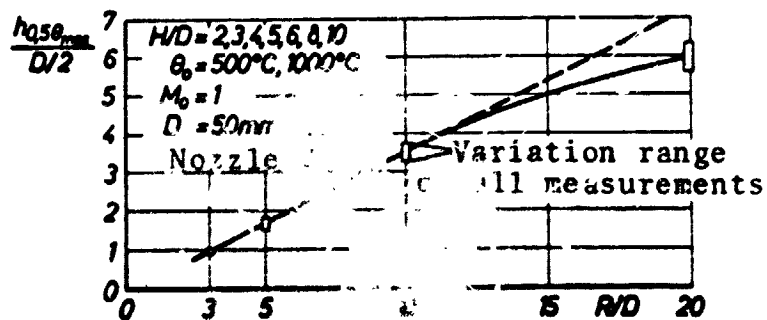


Figure 103. Half-value height of the total temperature.



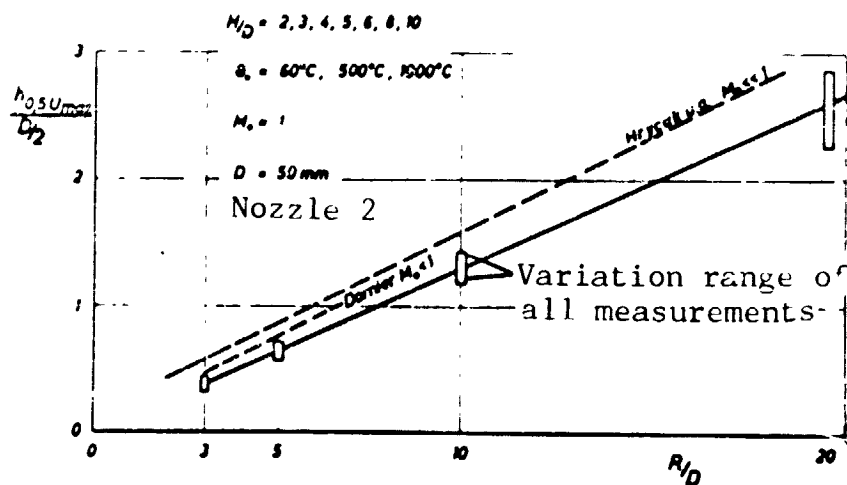


Figure 107. Half-value height for the velocity. Effect of the nozzle Mach number.

/ 161

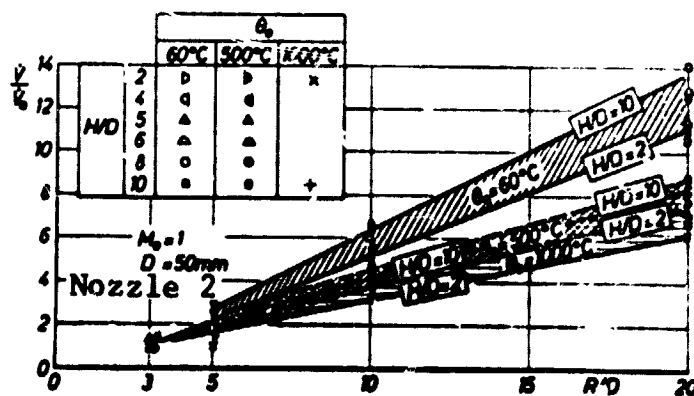


Figure 105. Increase in volume flow. Effect of temperature and H/D .

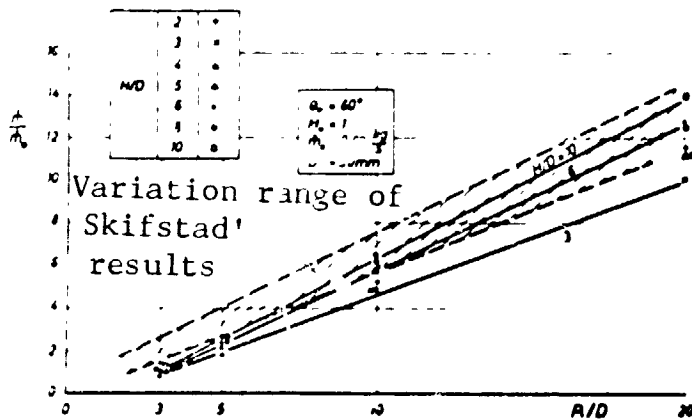


Figure 106. Increase in mass flow, H/D effect.

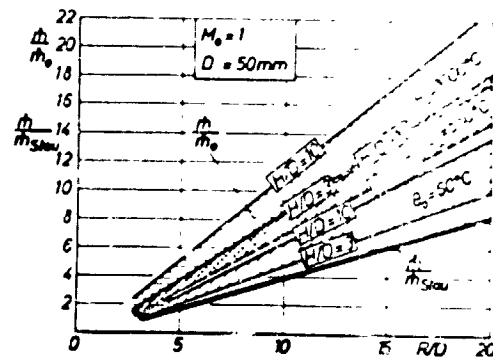


Figure 107. Increase in mass flow, temperature and H/D effect.

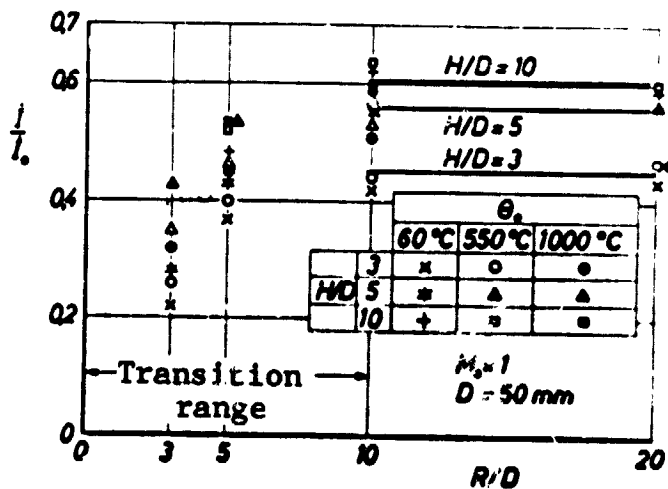


Figure 108. Total momentum flow, effect of temperature and H/D .

Figure 109. Experimental arrangement and measuring points for wind measurement.

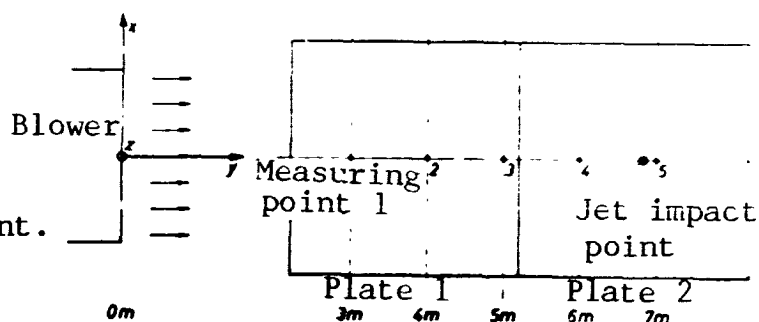
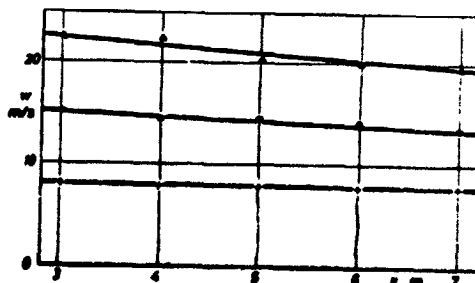


Figure 110. Course of the wind velocity along the Y axis 250 mm above the plate surface.



- Δ No throttle ring in the intake cross section
- o One throttle ring in the intake cross section
- + Two throttle rings in the intake cross section

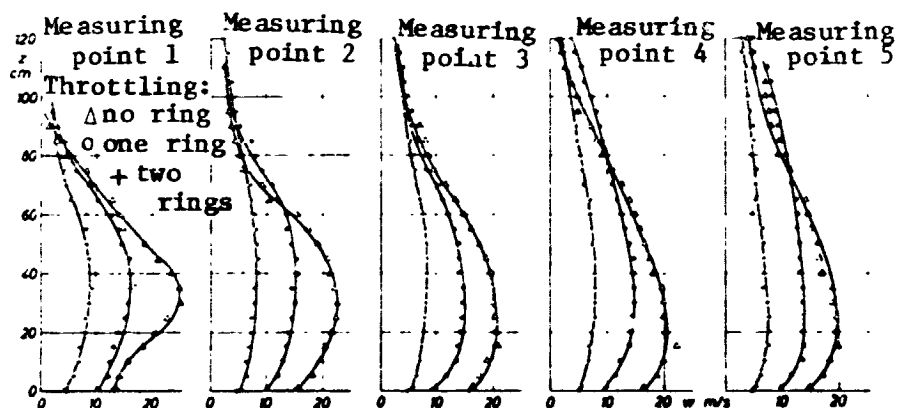


Figure 111. Measured vertical wind profile for different throttle settings.

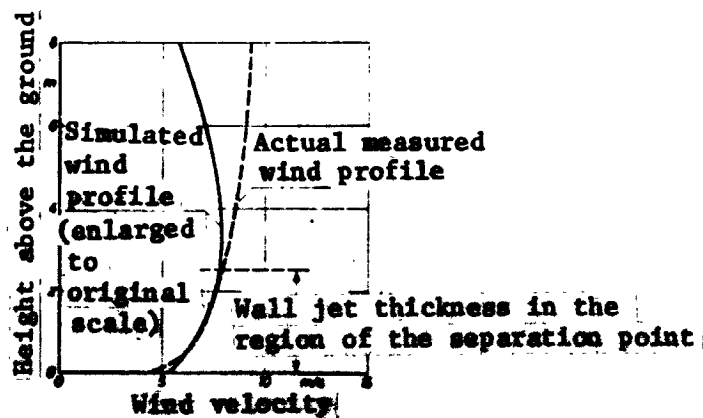


Figure 112. Comparison of a natural wind profile with the simulated one.



Figure 113. Light section photograph of a wall jet separation due to wind effect.
 $M_o = 1$, $\theta_o = 1,000^\circ\text{C}$,
 $W_o = 22 \text{ m/s}$, $H/D = 8$.



Figure 114. Light section photograph of a wall jet separation due to wind effect.
 $M_o = 1$, $\theta_o = 400^\circ\text{C}$,
 $W_o = 22 \text{ m/s}$, $H/D = 3$.

Figure 115. Horizontal light section through the wall jet, 50 mm above the plate surface.
 $M_o = 0.71$, $\theta_o = 60^\circ\text{C}$,
 $W_o = 22 \text{ m/s}$, $H/D = 3$.

Figure 116. Horizontal light section through the wall jet, 50 mm above the plate surface.
 $M_o = 0.78$, $\theta_o = 60^\circ\text{C}$,
 $W_o = 22 \text{ m/s}$, $H/D = 3$.

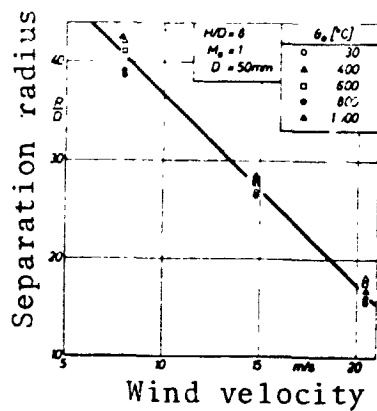


Figure 117. Separation radius of the wall jet. Temperature effect.

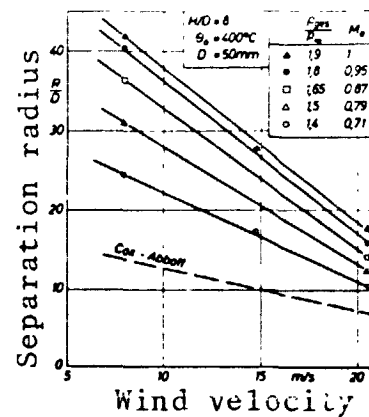


Figure 118. Separation radius of the wall jet. Mach number effect.

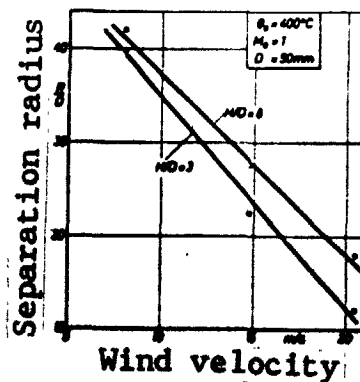


Figure 119. Separation radius of the wall jet, H/D effect.

9.6 Measuring accuracy and error estimation

/ 164

Systematic and random observational errors occur in measurements. While systematic errors can largely be calculated and eliminated, random errors cannot be prevented. They must be considered in the average of the experimental results.

Systematic errors

		Calculation in section
1. Effect of turbulence on the dynamic pressure measurement	0 to over 10%	9.44
2. Effect of radiation and recovery factor on the temperature measurement	0 to -2% (average: -1%)	9.45
3. Solar radiation onto the thermocouples		
4. Atmospheric wind movements		

The dynamic pressure error due to turbulence is considered throughout the evaluation of the results. The temperature measurements were not corrected, however, so that on the average they may be considered to be 1% too low. Error sources 3 and 4 can be eliminated by the fact that the experiments took place only on days on which direct solar radiation or wind movements did not occur.

Random errors

Digital voltmeter	± 0.2 to 0.5% or ± 1 digit
DMS pressure transducer	$\pm 1\%$
Calibration of the DMS pressure transducer	$\pm 0.5\%$
Hot film transducer	$\pm 1\%$

Jacketed thermocouple	up to 300°C: $\pm 2.2^\circ\text{C}$ above 300°C: $\pm 0.8\%$
Reference point temperature	$\pm 0.2\% \triangleq 0.1^\circ\text{C}$
Nozzle diameter tolerance	50 mm ± 0.05 mm
Position of the probe rake	± 2 mm
Individual measuring points of the probe rake	± 0.5 mm
Accuracy of quantities held constant during the time of the experiment:	
Nozzle prechamber pressure	$\pm 3\%$
Nozzle prechamber temperature	$\pm 5\%$

Accuracy of the impact pressure measurement:

/ 165

Turbulence causes a systematic error in measurement of the impact pressure. For the hot gas jet, it can amount to more than 10% of the measured value. This pitot probe error must always be considered for impact pressure measurements in turbulent flow. It is

$$\Delta q = \frac{P_{St}}{2 \cdot R \cdot T_{St}} (\bar{u}^2 + \bar{v}^2 + \bar{w}^2) \quad (9.103)$$

The local turbulent fluctuation velocities are not known for the Mach 1 jet, so that they must be estimated in this work. If we assign these estimates an accuracy of $\pm 20\%$ and allow an error of $\pm 2.3^\circ\text{C}$ in the temperature, then from the Gaussian law of error propagation, we obtain the average error of Δq .

$$S_{(\Delta q)} = \sqrt{\left(\frac{\partial \Delta q}{\partial \bar{u}}\right)^2 \cdot S_{(\bar{u})}^2 + \left(\frac{\partial \Delta q}{\partial \bar{v}}\right)^2 \cdot S_{(\bar{v})}^2 + \left(\frac{\partial \Delta q}{\partial \bar{w}}\right)^2 \cdot S_{(\bar{w})}^2 + \left(\frac{\partial \Delta q}{\partial T}\right)^2 \cdot S_{(T)}^2} \quad (9.149)$$

The relative error of the correction, Δq for the impact pressure is $\pm 25\%$. This is an error of about 3%, referred to the local

dynamic pressure. The measured dynamic pressure also has a random error of $\pm 1\%$ due to inaccuracies of the DMS pressure transducer and of $\pm 0.5\%$ from the calibration process, so that the measured dynamic pressure, corrected by the turbulence error, on which the evaluation is based, can be incorrect by $\pm 4.5\%$.

Accuracy of the calculated velocity

The velocity is calculated as:

$$u = \sqrt{\frac{2 \cdot c_p \cdot R \cdot T_H \cdot q}{(q \cdot R \cdot r^*) + (p_{3r} \cdot \epsilon \cdot c_p)}} \quad (9.95)$$

The dynamic pressure measurement has an inaccuracy of $\pm 4.5\%$, the temperature measurement has an error of $\pm 2\%$, and the recovery factor has an error of $\pm 2\%$. The Gaussian error propagation law is:

$$S_{(u)} = \sqrt{\left(\frac{\partial u}{\partial T_H}\right)^2 \cdot S_{(T_H)}^2 + \left(\frac{\partial u}{\partial q}\right)^2 \cdot S_{(q)}^2 + \left(\frac{\partial u}{\partial r^*}\right)^2 \cdot S_{(r^*)}^2} \quad (9.150)$$

The mean relative error of the velocity, calculated from the measurements with their errors, amounts to $\pm 3.3\%$.

Translated for National Aeronautics and Space Administration under contract No. NASw 2483, by Scitran, P. O. 5456, Santa Barbara, California, 93108.

1. Report No. NASA TT F-14,912	2. Government Accession No.	3. Recipient's Catalog No.
4. Title and Subtitle THE RECIRCULATION FLOW PATTERN OF A VTOL LIFT ENGINE. Ph.D. Thesis Brunswick U.	5. Report Date June 1973	6. Performing Organization Code
7. Author(s) E. Schwantes	8. Performing Organization Report No.	10. Work Unit No.
9. Performing Organization Name and Address SCITRAN Bcx 5456 Santa Barbara, CA 93108	11. Contract or Grant No. NASw-2483	13. Type of Report and Period Covered Translation
12. Sponsoring Agency Name and Address National Aeronautics and Space Administration Washington, D.C. 20546	14. Sponsoring Agency Code	
15. Supplementary Notes Translation of: Das Rezirkulationsströmungsfeld eines VTOL-Hubtriebwerks Source: Deutsche Forschungs- und Versuchsanstalt für Luft- und Raumfahrt, DLR-FB 72-50, pp. 1 - 165.		
16. Abstract A method was developed to predict theoretically the increase in temperature due to wind recirculation in the inlet of a VTOL lift engine exhaust discharging downward toward the ground. Calculation of the velocities in the recirculation flow and determination of the temperatures using the laws of spread of buoyant plumes, are presented with regard to potential theory. Model investigations were carried out to check the results. The three regions of a VTOL propulsion jet (the free jet, the wall jet, and the zone of separation of the wall jet from the ground due to wind effects and buoyancy forces) were investigated using model jets with critical nozzle pressure ratio and temperatures up to 1000 C.		
17. Key Words (Selected by Author(s))	18. Distribution Statement Unclassified - Unlimited	
19. Security Classif. (of this report) Unclassified	20. Security Classif. (of this page) Unclassified	21. No. of Pages 193
		22. Price